Permittivity

Full-waveform inversion of crosshole GPR data for hydrogeological applications

Anja Klotzsche

JÜLICH
FORSCHUNGSZENTRUM

Full-waveform inversion of crosshole GPR data for hydrogeological applications

Anja Klotzsche

Abstract

High resolution and precise characterization of aquifers is needed to improve the understanding of flow and solute transport processes. Decimeter-scale and high contrast structures caused by changes in the porosity or clay content can have a dominant effect on hydraulic processes within an aquifer. Such heterogeneities or layering in aquifers can be related to preferential flow paths or impermeable clay lenses and can act as electromagnetic low-velocity waveguides. Crosshole ground penetrating radar is able to provide shallow subsurface electrical properties, viz. dielectric permittivity and electrical conductivity, and has proven a powerful tool to map and characterize aquifers due to the method's high resolution and sensitivity to porosity and soil water content. Ray-based methods, which incorporate only a small part of the measured signal in the inversion, such as first-arrival travel times and first-cycle amplitudes, are not able to detect such layers. In contrast, the crosshole GPR full-waveform inversion, which considers the entire waveform or significant parts thereof, is able to resolve sub-wavelength high resolution images and can detect high contrast layers. Recently, a novel 2D time-domain vectorial full-waveform crosshole radar inversion was introduced that significantly improves the model resolution compared to standard ray-based techniques.

This GPR full-waveform inversion is modified by allowing an optimized acquisition setup that significantly reduces the acquisition time and computational costs. The improved algorithm is employed to invert crosshole GPR data acquired within a gravel aquifer in the Thur valley, Switzerland, using the ray-based results as starting models. Compared to the ray-based inversion, the results from the full-waveform inversion show images with significantly higher resolution. The simulated traces of the final model, obtained by the full-waveform inversion, fit the observed traces very well in the lower part of the section and reasonably well in the upper part of the section. By incorporating the vadose zone and the water table in the starting models and inversion domain, we are able to improve the initial results and resolve unprecedented sub-wavelength high resolution images for permittivity and conductivity in the entire inversion domain including a high permittivity layer between 5 m - 6 m depth. This high permittivity layer acts as an electromagnetic low-velocity waveguide and is caused by an increased porosity indicating a

I

possible zone of preferential flow. The waveguide trapping causes anomalously high amplitudes and elongated wave trains to be observed for transmitters within the waveguide and receivers straddling the waveguide depth range. The excellent fit of amplitudes and phase between the measured and modeled data confirms its presence.

The same saturated gravel aquifer is analyzed in 3D by inverting six crosshole GPR planes with the 2D full-waveform inversion. The 2D results are stitched together and visualized as 3D models. The full-waveform inversion results show decimeter-scale high resolution images and for the permittivity mainly similar structures at the borehole locations and at the intersection of the diagonal planes. The high permittivity layer which acts as low-velocity waveguide between 5 m - 6 m depth is revealed in all six planes. For transmitters located within the waveguides, a trace energy of at least one order of magnitude higher and late arrival elongated wave trains are observed for receiver positions straddling along this zone. In contrast, for the same receiver a distinct minimum in the trace energy is visible when the transmitter is located outside the waveguide. A novel amplitude analysis is developed that explores these maxima and minima positions of the trace energy spectra and is able to identify low-velocity waveguides and their boundaries from measured data only. The full-waveform inversion results are evaluated with logging data, whereby, hydraulic permeability estimates confirm the presence of a preferential flow path between 5 m - 6 m depth.

The newly introduced amplitude analysis is extended to characterize discontinuous waveguides, and to explore the potential and limitations of the method in more detail by performing different synthetic studies. Within this study, we found that the method is able to detect waveguides and their boundaries for different thickness, dip, extent, and model parameters of the waveguide layer. However, for waveguides thicknesses smaller than the spatial transmitter-receiver sampling, the boundaries could not be precisely resolved. In the presence of elongated wave trains with late arrival high amplitudes, the waveguide is caused by a change in the porosity (high permittivity) rather than a change in clay content (high conductivity), where no elongated wave trains are detected. For waveguides with a limited lateral extent characteristic wave propagation is observed forming high amplitudes and late arrival spreading in the data. Similar events are also observed in an experimental crosshole GPR dataset from the Boise Hydrogeophysical Research Site, where we identified two discontinuous waveguides in the data. The position and extent of the waveguides are confirmed by applying the full-waveform inversion.

The 2D GPR full-waveform inversion and novel amplitude analysis enables a detailed hydrogeological aquifer characterization, and can be applied to a wide range of geological, hydrological, glacial, and periglacial studies, thus improving our ability to detect and visualize important small-scale structures.

Zusammenfassung

Eine hoch aufgelöste und präzise Charakterisierung von Grundwasserleitern ist notwendig, um das Verständnis von Strömungs- und Stofftransportprozessen zu verbessern. Kleinskalige Strukturen im Boden, gekennzeichnet durch einen hohen Kontrast, entstehen häufig durch Veränderungen in der Porosität oder des Tongehaltes und können einen deutlichen Einfluss auf hydraulische Prozesse haben. Solche Heterogenitäten in Grundwasserleitern können mit präferentiellen Strömungswegen oder undurchlässigen Tonlinsen in Verbindung gebracht werden und als Wellenleiter niedriger Geschwindigkeit fungieren. "Crosshole"-Bodenradar, bei dem die Sender- und Empfängerantennen in zwei verschiedenen Bohrlöchern platziert sind, ist in der Lage, elektrische Eigenschaften des Untergrundes wie die dielektrische Permittivität (absolute Elektrizitätskonstante) und die elektrische Leitfähigkeit zu bestimmen. Aufgrund einer hohen Auflösung und Sensitivität gegenüber Porosität des Bodens konnte sich Crosshole-GPR in den letzten Jahren als leistungsfähiges Werkzeug zur Charakterisierung von Grundwasserleitern etablieren. Strahlenbasierte Verfahren, die nur einen kleinen Teil des gemessenen Signals bei der Inversion betrachten, sind häufig nicht in der Lage, kleinskalige Strukturänderungen zu detektieren. Im Gegensatz dazu können diese Schichten mit der Crosshole-GPR-Vollewellenforminversion, die das gesamte Signal betrachtet, mit hoher Auflösung und hohem Kontrast abgebildet werden.

Vor kurzem wurde eine neue, auf vektoriellem Ansatz basierende 2D-Vollewellenforminversion (VWI) im Zeitbereich für Crosshole-GPR entwickelt, welche die Modellauflösung im Vergleich zu Standard strahlenbasierten Techniken deutlich verbessert. Diese GPR-VWI wurde bezüglich einer optimierten Meßanordnung modifiziert, welche die Messzeit und den Rechenaufwand deutlich minimiert. Der verbesserte Algorithmus wurde eingesetzt, um Crosshole-GPR-Daten eines Kiesgrundwasserleiters des Flusses Thur (Schweiz) zu invertieren. Im Vergleich zur strahlenbasierten Inversion zeigen die Ergebnisse der VWI eine deutlich höhere Auflösung. Durch die Einbindung der ungesättigten Zone und des Grundwasserspiegels in die Startmodelle sind wir in der Lage, für den gesamten Bereich eine Auflösung kleiner der Wellenlänge für die Permittivitäts- und Leitfähigkeitstomogramme zu erhalten, einschließlich einer Schicht hoher Permittivität zwischen 5 m - 6 m Tiefe. Diese Schicht mit hoher Permittivität wirkt als elektromagnetischer Wellenleiter, verur-

sacht durch eine Erhöhung der Porosität des Mediums, und könnte auf einen präferentiellen Fließweg hindeuten. Für Sender, die innerhalb eines Wellenleiters positioniert sind, kann man aufgrund der multiplen internen Reflektionen extrem hohe Amplituden und längliche Wellenzüge für die Empfängerpositionen in selbiger Schicht in den Daten beobachten.

Eine 3D Darstellung des gleichen Kiesgrundwasserleiters konnte durch das Invertieren und Zusammenfügen von sechs Crosshole-GPR-Ebenen mittels der 2D-VWI ermöglicht werden. Die Ergebnisse der VWI zeigen hochauflösende Bilder innerhalb der Dezimeter-Skala und fr die Permittivität ähnlichen Strukturen in direkter Nähe der Bohrlöcher und am Schnittpunkt der diagonalen Ebenen. Die durch eine hohe Permittivität gekennzeichnete Schicht, die als Wellenleiter zwischen 5 m - 6 m Tiefe agiert, konnte in allen sechs Ebenen nachgewiesen werden. Für Senderpositionen innerhalb des Wellenleiters konnten wesentlich höher Energiespektren und längliche Wellenzüge für Empfängerpositionen entlang dieser Zone beobachtet werden, wohingegen für die gleichen Empfänger ein ausgeprägtes Minimum im Energiespektrum sichtbar war, wenn der Sender außerhalb des Wellenleiter positioniert wurde. Eine neuartige Amplitudenanalyse wurde entwickelt, die diese Position der Maxima und Minima im Energiespektrum der gemessenen Daten zur Identifizierung von Wellenleitern und deren Grenzen benutzt. Die Ergebnisse der VWI wurden mit Hilfe von Bohrlochlogs ausgewertet, wobei die hydraulische Permeabilität das Vorhandensein eines präferentiellen Fließweges in einer Tiefe zwischen 5 m - 6 m bestätigt.

Das Potential und mögliche Einschränkungen des neuartigen Ansatzes der Amplitudenanalyse wurden mittels verschiedener synthetischer Studien untersucht. In diesen Studien zeigte sich, dass das angewendete Verfahren in der Lage ist, Wellenleiter und ihre Schichtgrenzen für unterschiedliche deren laterale und vertikale Ausdehnung sowie verschiedene Modellparameter der Wellenleiterschicht nachzuweisen. Längliche Wellenzüge mit hohen Amplituden ließen auf einen Wellenleiter schließen, der durch eine Veränderung in der Porosität (hohe Permittivität) verursacht wird. Hingegen wurden bei Veränderungen im Tongehalt (hohe Leitfähigkeit) keine länglichen Wellenzüge beobachtet. Für Wellenleiter mit einer begrenzten horizontalen Ausdehnung konnte eine charakteristische Wellenausdehnung mit einhergehenden hohen Amplituden und verzögerter Ausbreitung der Welle im Medium beobachtet werden. Ähnliche Ergebnisse wurden auch in einem experimentellen Datensatz für den Grundwasserleiters des Flusses Boise (USA) gefunden. Hier konnten zwei Wellenleiter mit begrenzter horizontaler Ausdehnung in den Daten identifiziert werden, welche durch die VWI bestätigt wurden.

Die 2D-GPR-VWI und die neue Amplitudenanalyse ermöglichen eine detaillierte hydrogeologische Charakterisierung von Grundwasserleitern. Insbesondere durch die verbesserte Lokalisierung vor allem kleinskaliger Strukturen eignen sich die Methoden für eine breite Palette geologischer, hydrologischer, glazialer und peri-glazialer Studien.

List of Publications

At the time of writing this dissertation, parts of the doctoral thesis have been published, submitted, or are in preparation for publication by scientific journals and contributed to scientific meetings as specified below. Chapters 1 - 5 are based on papers numbered 1 - 4, Appendices A - C are based on publications numbered 5 - 7, respectively.

1. **Klotzsche, A.**, J. van der Kruk, A. G. Meles, J. Doetsch, H. Maurer, and N. Linde, 2010. Full-waveform inversion of crosshole ground penetrating radar data to characterize a gravel aquifer close to the river Thur, Switzerland. Near Surface Geophysics 8, 631-646, 2010, doi: 10.3997/1873-0604.2010054.

2. **Klotzsche, A.**, J. van der Kruk, A. G. Meles, and H. Vereecken, 2012. Characterizing a low-velocity waveguide using crosshole GPR full-waveform inversion. Geophysics 77, H57-H62, 2012, doi: 10.1190/geo2011-0458.1.

3. **Klotzsche, A.**, J. van der Kruk, N. Linde, J. Doetsch, and H. Vereecken, 2013. 3-D characterization of high-permeability zones in a gravel aquifer using 2-D crosshole GPR full-waveform inversion and waveguide detection. Geophysical Journal International, doi: 10.1093/gji/ggt275.

4. **Klotzsche, A.**, J. Bradford, H. Vereecken and J. van der Kruk, Detection and identification of waveguides with limited lateral extension: synthetic and experimental data. Journal of Hydrology, submitted.

5. Oberöhrmann, M., **A. Klotzsche**, H. Vereecken, and J. van der Kruk, 2013. Optimization of acquisition setup for cross-hole GPR full-waveform inversion using checkerboard analysis. Near Surface Geophysics 11, doi: 10.3997/1873-0604.2012045.

6. **Klotzsche, A.**, J. van der Kruk, H. Vereecken, G. A. Meles, J. Doetsch, H. Maurer, S. A. Greenhalgh, A. G. Green, and N. Linde, 2011. High resolution imaging of the unsaturated and saturated zones of a gravel aquifer using Full-waveform inversion. 6th International workshop on advanced ground penetrating radar, 20-24.

7. Yang, X., **A. Klotzsche**, J. van der Kruk, H. Vereecken, G. A. Meles, and H. Maurer, Full-waveform inversion of cross-hole GPR data measured at the Boise gravel aquifer. 6th International workshop on advanced ground penetrating radar, 304-307.

Contents

X

Chapter 1

Introduction

Over recent decades, aquifers have been characterized to predict flow and transport through complex media at various scales. Knowledge about the flow in a complex multi-phase systems such as the vadose zone is necessary to evaluate risk, storage and clean-up potentials of aquifers (Hubbard *et al.*, 2001; Binley *et al.*, 2002a,b; Kemna *et al.*, 2002). The delineation of decimeter-scale aquifer heterogeneities is desirable in environmental monitoring and remediation because they impact solute transport (Scheibe & Yabusaki, 1998; Zheng & Gorelick, 2003). Such heterogeneities may be layers that contrast with surrounding sediments in lithology, porosity and the degree of water saturation, and so may indicate preferential flow paths or impervious clay zones. Therefore, the precise knowledge of the localization (depth) and extensions of such heterogeneous layers is important. Traditional methods that are applied to characterize aquifers and derive hydrogeological properties of an aquifer have either a small spatial sampling volume and a high resolution, such as slug tests, logging tools or core samples analyses, or capture an average response over a large volume, such as pumping or tracer tests. Hydrological measurements, including hydraulic tomography, characterize aquifers at a fairly large-scale but with limited spatial resolution (Brauchler *et al.*, 2011), whereas lab analysis and well logging have small support volumes away from the sample location or boreholes.

Geophysical methods like ground penetrating radar (GPR), electrical resistivity tomography (ERT) and seismics are able to close the gap between these small-scale investigations and large-scale methods (Rubin *et al.*, 1992; Hubbard & Rubin, 2000; Binley *et al.*, 2001; Garambois *et al.*, 2002; Linde *et al.*, 2008; Doetsch *et al.*, 2010a; Slater *et al.*, 2010). Moreover, they are able to improve the subsurface resolution and resolve heterogeneities over appreciable volumes of the aquifer. Thereby, site specific empirical relationships are often necessary to transform these geophysical parameters into hydraulic properties (Clement & Barrash, 2006; Linde *et al.*, 2006). Several research groups have made

detailed geophysical investigations of specific aquifers to improve the understanding of how different geophysical methods can be used to gain hydrological insights of aquifer behavior, for example, the Boise Hydrogeophysical Research Site (BHRS) in the USA (Bradford *et al.*, 2009; Dafflon *et al.*, 2011a), the Widen test site in Switzerland (e.g. Diem *et al.* (2010); Doetsch *et al.* (2010a); Coscia *et al.* (2012)) and the MAcro Dispersion Experiment (MADE) site in the USA (Dogan *et al.*, 2011; Zheng *et al.*, 2011). These results show that GPR, ERT and seismics are all able to provide porosity estimates for aquifers, but that porosity estimates based on seismic velocity are not as well constrained as those from radar wave speed. Each of the three methods has different benefits, but also suffers from certain limitations. For borehole deployments the resolution of inferred seismic and radar parameters are depending on the ray-coverage of the measurements, which is typically high in between the boreholes and low at the top and bottom of the acquisition domain, whereas ERT parameters are better constrained close to the electrodes and less constrained in between the boreholes (Day-Lewis *et al.*, 2005). GPR is able to return the highest resolution images compared to ERT and seismics for aquifers (Doetsch *et al.*, 2010a), and several non-invasive surface and minimally-invasive crosshole GPR measurements have shown the high potential to characterize the saturated aquifer and the vadose zone (Hubbard *et al.*, 1997; Tronicke *et al.*, 1999; Binley *et al.*, 2001; Hubbard *et al.*, 2001; Tronicke *et al.*, 2002; Winship *et al.*, 2006; Looms *et al.*, 2008).

Another major advantage of GPR is that by employing one method, it is possible to obtain two parameters; the dielectric permittivity ε (related to velocity v) and electrical conductivity σ (related to attenuation α) in connection with assorted geological, hydrological and engineering investigations. For convenience, we use the relative permittivity $\varepsilon_r = \varepsilon/\varepsilon_0$ (or dielectric constant) in this thesis. Table 1.1 shows relative permittivity, conductivity, velocity and attenuation values for selected materials. The geophysical responses caused by changes in ε_r or σ can be linked to hydrogeologically relevant variables such as porosity, water content, water salinity, permeability, fluid content, and pore structure, clay content and lithological variations (Archie, 1942; Topp *et al.*, 1980; al Hagrey & Müller, 2000; Garambois *et al.*, 2002; Barrash & Clemo, 2002; Turesson, 2006; Linde *et al.*, 2006; Kettridge *et al.*, 2008). The electromagnetic (EM) wave velocity mainly depends on the relative dielectric permittivity and due to the high variety of permittivity from air ($\varepsilon_r = 1$) to pure water ($\varepsilon_r = 80$ at 20°C), this parameter can be used to determine the water content or porosity (in the case of a saturated medium) in an aquifer and in the vadose zone. For example, wet sand has a permittivity range of 20 - 30, whereas completely dry sand has a permittivity range of 3 - 5 (see Table 1.1 and Davis & Annan (1989)). In contrast, the attenuation of the EM wave depends strongly on the electrical conductivity σ of the medium, which can give indications about clay content or pore water

Table 1.1: Permittivity ε_r, conductivity σ, velocity v and attenuation α for selected materials for a frequency of 100 MHz (Blindow, 1997).

	$\varepsilon_r[-]$	$\sigma[mS/m]$	$v[m/ns]$	$\alpha[dB/m]$
air	1	0	2.998	0
fresh water	80	0.5	0.033	0.1
salt water	80	30 000	0.01	1000
dry sand	3 - 5	0.01	0.15	0.01
saturated sand	20 - 30	0.1 - 1	0.06	0.03 - 0.3
silt	5 - 30	1 - 100	0.07	1 - 100
clay	5 - 40	2 - 100	0.06	1 - 300
limestone	4 - 8	0.5 - 2	0.12	0.4 - 1
granite	6	0.01 - 1	0.12	0.01 - 1
dry salt	6	0.001 - 0.1	0.125	0.01 - 1
ice	3.18	0.01	0.168	0.02

salinity (Davis & Annan, 1989; Tronicke *et al.*, 2004). Therefore, high frequency bistatic crosshole GPR is well suited to monitor infiltrations and recharge processes of aquifer systems due to its minimal invasive investigation and sensitivity to soil water content (Clement & Barrash, 2006; Binley *et al.*, 2001; Hubbard *et al.*, 1997; Winship *et al.*, 2006; Tronicke *et al.*, 2002). Crosshole radar surveying entails the generation of high-frequency electromagnetic pulses from a dipole-type antenna, which is sequentially positioned at a number of locations along a borehole. The resulting transmitted and scattered waves are detected and subsequently recorded by means of a dipole antenna, which is progressively moved to a number of discrete locations in a second borehole. The center frequency of most GPR borehole antennas lies in the range 20 MHz - 250 MHz with a corresponding dominant wavelengths of 5 m - 0.4 m for common geological materials.

For measuring crosshole GPR, several methods can be applied. Zero-offset profiling (ZOP) obtains a one-dimensional profile of averaged travel time by systematically lowering or rising of the transmitter and receiver antennas at equal depths at the same time located in two different boreholes, whereas it is assumed that waves traveling horizontally directly from transmitter to receiver are measured. In a heterogeneous medium not only a direct wave occurs, but also scattered waves caused by reflections and refractions (see Fig. 1.1), therefore, an improved method is the multi-offset gather, which is the basis of the tomographic inversion. The receiver is moved to different locations by constant spacing in one borehole, while the transmitter remains fixed in a second borehole. This is repeated for

several positions of the transmitter and guarantees that the medium between the boreholes is sampled by a large number of rays with a larger number of angles. To improve the resolution, reciprocal measurements can be collected. The highest resolution is obtained in the central part of the tomogram due to the denser ray-coverage. In comparison, the resolution is lower close to the transmitter and receiver positions.
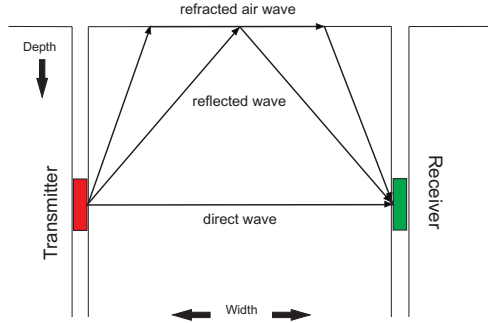
Figure 1.1: Ray-paths of direct, refracted and reflected waves that can be measured during a GPR crosshole measurement. Transmitter and receiver antenna are shown in the left and right borehole, respectively, based on Annan (2005).

To derive the distribution of physical parameters in the subsurface from geophysical data, inversion algorithms are generally needed. Commonly applied inversion algorithms for seismics and GPR are based on ray-based methods like first-arrival time and first-cycle amplitude inversion (Musil *et al.*, 2006), or Fresnel volume radar-propagation velocity tomography (Buursink *et al.*, 2008). A number of studies have estimated hydrogeological parameters by inverting crosshole ground penetrating radar data using ray-based inversion schemes, similar to that described by Holliger *et al.* (2001). For example, Tronicke *et al.* (2002) examined the integration of surface GPR and crosshole radar tomography on braided stream deposits, while Binley *et al.* (2002a,b) and Winship *et al.* (2006) used crosshole GPR to monitor moisture content changes arising from tracer experiments. Linde *et al.* (2006) were able to improve hydrogeological characterization by using a joint inversion of crosshole electrical resistance and GPR travel time data. Looms *et al.* (2008) monitored unsaturated flow and transport by using cross-borehole GPR and ERT.

Conventional GPR tomographic inversions of crosshole GPR data use inversions of picked travel times and maximum first-cycle amplitudes (see Fig. 1.2) of the transmitted radar pulses based on ray theory to visualize the interwell medium. These inversion techniques provide velocity and attenuation images of the subsurface that can be transformed into dielectric permittivity and electrical conductivity. Radar tomography based on ray

theory provides a rather limited resolution because such a inversion uses high-frequency approximations and only accounts for a small fraction of the information contained in the data indicated by red and green in Figure 1.2, such that small targets (smaller than the dominant wavelength) cannot be satisfactorily detected and imaged. Moreover, these techniques typically use regularization in the form of damping or smoothing constraints, to make the inversion algorithm robust and assure convergence. The reconstructed images have a spatial resolution that scales with the diameter of the first Fresnel-zone $\sqrt{\lambda L}$ (Williamson, 1991), where λ is the dominant wavelength and L the wave propagation path length. For a borehole separations of 5 m - 10 m commonly used radar systems operate at pulse bandwidths centered at 100 MHz - 250 MHz, with effective wavelengths of about 1 m. These scaling parameters indicate that decimeter-scale inhomogeneities cannot be accurately mapped using ray-based inversion techniques.
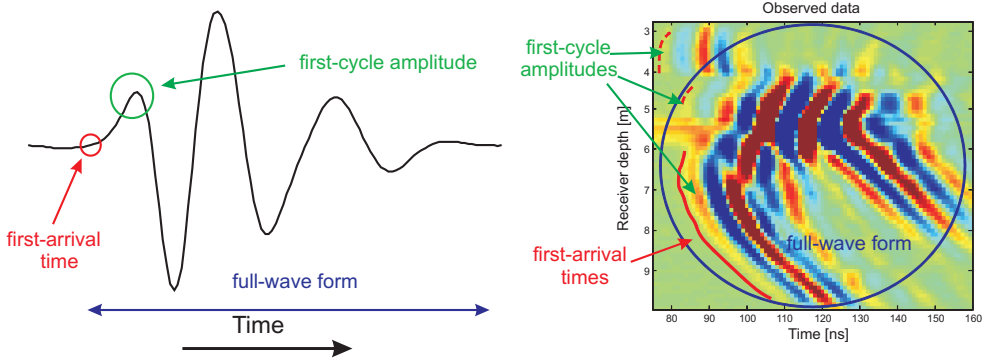
Figure 1.2: Difference between the travel time, first-cycle amplitude and the full-waveform inversion in red, green and blue, respectively. a) Trace of one receiver and b) image plot for all receiver traces for one transmitter position over time. For the travel time and amplitude inversion only the first-arrival and the first-cycle amplitude are considered, while for the full-waveform inversion the entire information of the trace is used.

In the presence of high contrast layers caused by changes in the water content (higher permittivity) or clay content (high electrical conductivity) the electromagnetic waves are affected due to their reduced velocity. When the electrical thickness of a high electrical contrast layer compares with or is smaller than the in situ wavelength of the incident electromagnetic (EM) wave, the layer can act as a waveguide (Arcone *et al.*, 2003; van der Kruk *et al.*, 2009a,b). As the electromagnetic wave speed is reduced in these layers due to an increase in dielectric permittivity, total reflection occurs at the layer boundaries beyond the critical angle and the guided electromagnetic waves are multiple reflected and form late arrival elongated and dispersed wave trains with high amplitudes

that are captured in the measured signal. Due to the trapped electromagnetic energy, the wave can propagate in these low-velocity waveguides over large distances. Such late arrival events, caused by a waveguide are ignored by ray-based methods and therefore, the low-velocity waveguides cannot be resolved by these techniques.

Following classic treatments for seismic waveguides (Ewing & Press, 1957), GPR waveguides, particularly along the surface, have been studied since the last decades (Collin, 1991). A promising tool to estimate the permittivity and the thickness of shallow surface waveguide layers is dispersion analysis, which is based on the fundamental equations of modal theory (van der Kruk *et al.*, 2009b). This method is able to investigate low-velocity, low velocity layer embedded between higher velocity layers, and leaky, low velocity layer embedded between a higher and a lower velocity or larger conductivity layer waveguides. However, borehole measurements are needed to investigate deeper waveguides that cannot be detected by surface measurements. Due to the different acquisition setup, the dispersion analysis cannot be applied. Such deeper waveguides between boreholes have been investigated for seismic data (Lines *et al.*, 1992; Greenhalgh *et al.*, 2007) and for cross-well radar data (Ellefsen, 1999), but have not been reliably inverted due to the late time arrivals and resolution limitations of conventional ray-based techniques.

Thin high contrast layers which are caused by porosity increase or clay lenses play an important role for hydrological processes in aquifers (al Hagrey & Michaelson, 1999; Day-Lewis *et al.*, 2003; Ronayne & Gorelick, 2006; Bianchi *et al.*, 2011), but their restricted thickness often prevents standard methods from detecting the exact position and dimensions of such high contrast layers. To reliably image deeper waveguides, a new high resolution technique is necessary that is able to include complicated wave field modeling in the inversion. The full-waveform inversion of high-frequency GPR-type pulses is able to resolve high resolution images of half the in-situ wavelength (Wu & Toksoz, 1987; Pratt & Shipp, 1999) and can therefore, be used to resolve small-scale structures in layered media with a large number of unknown thicknesses and electrical parameters. In contrast to the ray-based methods, full-waveform inversion not only takes into account the arrival times and first-cycle amplitudes but exploits the full information content of the data (or significant parts of the wave field) including secondary events like forward scattered and refracted waves as illustrated in Figure 1.2. The full-waveform inversion for GPR data uses an accurate forward model based on Maxwell's Equations. Therefore, full-waveform inversions is able to resolve higher resolution images and can thus yield more detailed information for a wide range of applications including sub-wavelength thickness high contrast layers.

Waveform-based inversion schemes were first developed in seismic exploration subject to the acoustic (P-wave only) approximation (Tarantola, 1984a,b, 1986) and were later

modified for elastic (P- and S-) wave propagation (Mora, 1987). Since the pioneering work of Tarantola (1984a), several research groups further developed the full-waveform inversion approach and applied it to seismic data for surface and/or borehole measurements (Tarantola, 2005; Virieux & Operto, 2009). The methods have been adapted to the acoustic-, elastic-, viscoelastic- and anisotropic-wave equations in both time and frequency domain. For that, finite-difference and finite-element approaches are used to solve the forward problem (Zhou & Greenhalgh, 1998b,a, 2003; Pratt, 1999; Pratt & Shipp, 1999; Bohlen, 2002; Watanabe et al., 2004; Fichtner & Trampert, 2011). Full-waveform seismic inversion is extensively discussed in the November 2008 special issue of the Journal Geophysical Prospecting and contains numerous additional other references. Nevertheless, applications to marine seismic data are challenging, mainly due to the absence of low-frequencies components and the highly non-linear objective function (Wang & Rao, 2006; Shin & Cha, 2008). In comparison to surface measurements, crosshole setups are better constrained due to the direct wave traveling between the boreholes, the known borehole separation and a good coupling of the transmitters and receivers. Thereby, the full-waveform inversion of seismic crosshole data is more robust and can successfully be inverted (Belina et al., 2009; Zhang, 2012).

The potential of this method for crosshole GPR was recently demonstrated for synthetic data (Ernst et al., 2007a; Kuroda et al., 2007) and for experimental data (Ernst et al., 2007b; Belina et al., 2012). Ernst et al. (2007a) developed a full-waveform scalar inversion scheme for electromagnetic waves for crosshole GPR data based on the 2D finite difference time-domain (FDTD) solution of Maxwell's Equations using generalized perfectly matched layers to reduce artefacts from reflections at the boundaries and edges of the model space. This scheme was tested on synthetic and observed crosshole data (Ernst et al., 2007b). The obtained results showed that this algorithm provides higher resolution permittivity and conductivity images of the subsurface than conventional ray-based techniques. Similar to Ernst et al. (2007a), Kuroda et al. (2007) applied a full-waveform inversion algorithm to synthetic crosshole radar data. Further theoretical developments by Meles et al. (2010) improved the method of Ernst et al. (2007a) by including the vector properties of the electric field, which enabled an extension of the algorithm to incorporate surface-to-borehole measurements in addition to crosshole measurements. Furthermore, the permittivity and conductivity parameters were simultaneously updated, which proved to be superior to the sequential (cascaded) update approach of Ernst et al. (2007a). Only smoothing of the gradients is applied and no damping parameters are necessary.

Thesis objectives and outline

The primary objectives of this thesis are to improve, explore, and apply the crosshole GPR full-waveform inversion to experimental data sets to achieve an enhanced understanding of the decimeter-scale processes within aquifers. Therefore, we use for all applications the recently proposed and improved full-waveform inversion algorithm of Meles *et al.* (2010, 2011, 2012), which was only tested for synthetic data until recently.

After this introductory Chapter, the second Chapter of this thesis describes the fundamentals of the electromagnetic wave propagation, the ray-based and the full-waveform inversion for crosshole GPR. Thereby, all processing steps for the application of the full-waveform inversion to experimental data are discussed in detail including the 3D to 2D transformation of the measured data, the estimation of the starting model and the procedure to obtain the effective source wavelet.

In Chapter 3, we extend the crosshole GPR full-waveform inversion and apply it to the saturated zone of a gravel aquifer in Switzerland to achieve high resolution images of the aquifer. Thereby, all the necessary steps are described that are important to perform the full-waveform inversion to experimental data, such as the determination of the starting model and the estimation of the unknown effective source wavelet. To improve the acquisition time and the computation cost, we apply an optimized semi-reciprocal measurement setup, and adapt the processing steps and the full-waveform inversion algorithm to use this setup. In the first part of Chapter 3, the starting models for the full-waveform inversion are obtained by the ray-based inversion. The final full-waveform inversion results show significantly higher resolution images between 6 m - 10 m depth compared to the ray-based inversion results. The underlying lacustrine clay sediments are clearly observed in conductivity images below 10 m depth. Due to the presence of the water table, which forms a high medium contrast, and associated refracted/reflected waves, the upper traces are not well fitted and the upper 2 m in the permittivity and conductivity tomograms (4 m - 6 m depth) are not reliably reconstructed. Therefore, an improved starting model is applied in the second part of Chapter 3, which enables us to reliably image the entire inversion domain by incorporating the unsaturated zone above the ground water table and by defining a homogeneous layer below the water table that represents better the measured data. Using this starting model the full-waveform inversion resuls provid reliable inversion results for the entire saturated aquifer and reveal a high contrast layer between 5 m - 6 m depth. The high contrast layer is identified as a sub-wavelength thickness low-velocity EM waveguide caused by a high porosity and indicates a possible zone of preferential flow. The waveguide trapping causes anomalously high amplitudes and elongated wave trains to be observed for a transmitter within the

waveguide and receivers straddling the waveguide depth range.

In Chapter 4, the same aquifer is analyzed in 3D by inverting six crosshole GPR planes by applying the 2D full-waveform inversion. The aim is to determine the aquifer geometry and the lateral extent of the high permittivity zone, which was observed in Chapter 3, that acts as a waveguide between 5 m - 6 m depth. Therefore, we separately invert six GPR planes and visualize the results in 3D. The full-waveform inversion results of the saturated part of the gravel aquifer show unprecedented decimeter-scale resolution images having mainly similar structures at the borehole locations and at the intersection of the diagonal planes. Moreover, in all the six planes the high dielectric permittivity layer is revealed between 5 m - 6 m depth. This layer can be related to an increase of the porosity and indicates a zone of preferential flow. The measured data are analyzed in detail for their amplitude and energy behavior to highlight the existence of wave-guiding structures. Furthermore, we develop a novel amplitude analysis that explores the maxima and minima position of the trace energy spectra of the measured data and is able to identify waveguides and their boundaries without applying any inversion. Finally, the full-waveform inversion results are compared to logging data acquired in the same boreholes.

In Chapter 5, we analyze the potential and limitation of the novel amplitude analysis approach and the full-waveform to detect low-velocity waveguides with a limited lateral extend. Therefore, we perform different synthetic studies using the amplitude analysis, where we vary the thickness, the extension, the orientation, and the model parameters (permittivity and conductivity) of defined low-velocity waveguides. For waveguides with a limited lateral extension (discontinues) we observe characteristic wave propagation forming late arrival spreading of high amplitudes in the data. Furthermore, the amplitude analysis is able to characterize waveguides with different thicknesses, dipping, and extensions, but is restricted to the transmitter-receiver sampling and boundaries for waveguides with a thickness smaller than the spatial sampling are not accurately resolved. In the presence of elongated wave train, the waveguide is caused by a change in the porosity, whereas when no elongate wave train is present but distinct minima positions can be observed, the waveguide is caused by a change in clay content. The new observed wave characteristics for discontinues waveguides are also observed in an experimental crosshole GPR dataset from the BHRS, where we able to identify two wave-guiding structures in the measured data using the amplitude analysis. Full-waveform inversion results and Neutron logging data confirmed these wave-guiding structures and indicated that these layers were caused by the change of the gravel to sand units.

Final conclusions and an outlook for further work are given in Chapter 6. The outlook presents topics for future research such as the extension of the 2D code to 3D and the combined inversion of saturated, unsaturated and surface data using the full-waveform

inversion.

Appendices A - C include additional studies that I was involved in my Ph.D.:

A) The paper Oberröhrmann *et al.* (2013), co-authored by me, involved the optimization of acquisition setup for crosshole GPR full-waveform inversion using checkerboard analysis. My main contribution was to supervise the application the full-waveform inversion for experimental and synthetic data, and helped to interpret the obtained results.

B) The combined inversion of the saturated and unsaturated zone of an aquifer and their first application including the adaption of the full-waveform inversion code for the use of more than one source wavelet;

C) The full-waveform inversion of crosshole GPR data measured at the Boise gravel aquifer using different developing steps of the full-waveform inversion to demonstrate the improvements from the first developments of Ernst *et al.* (2007a) until the final version of the algorithm Meles *et al.* (2010). My main contribution was to support the estimation of the source wavelet and the application of the different full-waveform inversion codes.

Chapter 2

Theory

In this Chapter, first the fundamentals of the electromagnetic wave propagation are introduced. After describing the basics of the ray-based inversion schemes, the different processing steps for the application of the full-waveform inversion for experimental cross-hole GPR data are explained; including the 3D to 2D conversion of the measured data, the forward model, the estimation of the effective source wavelet, and the inversion algorithms.

2.1 Fundamentals of electromagnetic wave propagation

The Maxwell Equations describe the propagation of the electric and magnetic fields in terms of their sources and can be used to interpret GPR traces to achieve information of the medium through which the GPR waves have traveled. Following Meles *et al.* (2010), the Maxwell Equations in combination with the electromagnetic constitutive parameters locally defined at any point of time t and space $\mathbf{x}$ are given in the differential form by:

$$\begin{bmatrix} -\varepsilon(\mathbf{x})\partial_t - \sigma(\mathbf{x}) & \nabla\times \\ \nabla\times & \mu(\mathbf{x})\partial_t \end{bmatrix} \begin{bmatrix} \mathbf{E}^s(\mathbf{x},t) \\ \mathbf{H}^s(\mathbf{x},t) \end{bmatrix} = \begin{bmatrix} \mathbf{J}^s(\mathbf{x},t) \\ \mathbf{0} \end{bmatrix}, \tag{2.1}$$

where
$\mathbf{E}^s$ - electrical field generated by $\mathbf{J}^s$,
$\mathbf{H}^s$ - magnetic field generated by $\mathbf{J}^s$,
$\mathbf{J}^s$ - current density source vector,
$\varepsilon(\mathbf{x})$ - dielectrical permittivity,
$\sigma(\mathbf{x})$ - electrical conductivity,
$\mu(\mathbf{x})$ - magnetic permeability.

The field quantities are vectorial functions (bold letters) of space and time, while the constitutive medium parameters are scalar functions of position and it is assumed that the medium is linear and non-dispersive. The superscript S is used for the particular source. The vectorial quantities $\mathbf{E}^s$, $\mathbf{H}^s$ and $\mathbf{J}^s$ contain the entire space-time domain such as $\mathbf{E}^s = \{\mathbf{E}^s(\mathbf{x}, t), \forall t \in T, \forall \mathbf{x} \in V\}$, where V represents the model space. The permeability is assumed to be constant throughout this thesis. See Meles *et al.* (2010) for a detailed discussion of this vector formalism.

In the following, only the electrical field $\mathbf{E}^s$ is investigated and thus the magnetic field $\mathbf{H}^s$ can be eliminated from Equation (2.1). The electrical field $\mathbf{E}^s$ can be expressed in a simple formulation by $\mathbf{E}^s = \mathbf{G}\mathbf{J}^s$, where $\mathbf{G}$ represents the Greens operator and describes the propagation of the electrical field through the medium. The explicit formulation of this Equations for a specific time and space point $(\mathbf{x}, t)$ is given by

$$\mathbf{E}^s(\mathbf{x}, t) = \int_V dV(\mathbf{x}') \int_0^{T_{max}} dt' \mathbf{G}(\mathbf{x}, t, \mathbf{x}', t') \mathbf{J}^s(\mathbf{x}', t'), \tag{2.2}$$

where $\mathbf{E}^s(\mathbf{x}, t)$ is the electrical field at point $(\mathbf{x}, t)$ generated by $\mathbf{J}^s(\mathbf{x}', t')$, and T_{max} is the maximum observation time. Here, the Greens tensor $\mathbf{G}(\mathbf{x}, t, \mathbf{x}', t')$ acts on the source term $\mathbf{J}^s(\mathbf{x}', t')$, which is defined as $\mathbf{J}^s = \delta(\mathbf{x} - \mathbf{x}_s) \cdot b \cdot \mathbf{S}(\omega)$, where $\mathbf{S}$ is the source wavelet, b identifies the antenna orientation and the delta function describes the position.

The general form of the electrical field in the frequency domain is given by

$$\hat{\mathbf{E}}^s = \hat{\mathbf{G}}\hat{\mathbf{J}}^s, \tag{2.3}$$

where $\hat{}$ indicates the frequency domain. For far-field and high frequency approximation $\hat{\mathbf{G}}$ can be described by

$$\hat{\mathbf{G}}(\mathbf{x}, \omega) = \frac{j\omega}{|\mathbf{x}|} \mathbf{A} e^{-\alpha|\mathbf{x}|} e^{-j\frac{\omega}{v}|\mathbf{x}|}, \tag{2.4}$$

where $\mathbf{A}$ is the amplitude, α the attenuation, $|\mathbf{x}|$ the travel distance and v the velocity of the medium (van der Kruk *et al.*, 2003). The term $j\omega$ is applied due to the solution in homogeneous 3D medium or to a halfspace (van der Kruk, 2001).

The real part of the bulk dielectric permittivity ε in natural medium can be derived with c as the radar wave velocity in air (< 0.3 m/ns) and for high frequencies, low loss and non-magnetic materials ($\mu \approx 1$ with $\mu = \mu_0 \cdot \mu_r$ with $\mu_0 = 4 \cdot \pi \cdot 10^{-7}$)

$$v = \frac{c}{\sqrt{\varepsilon}} \tag{2.5}$$

whereas ε is described by the relative to their values in vakuum $\varepsilon = \varepsilon_0 \cdot \varepsilon_r$ with $\varepsilon_0 = 8.8542 \cdot 10^{-12}$. Typically in ground penetrating radar, the relation

$$\alpha = \frac{\sigma}{2} \sqrt{\frac{\mu}{\varepsilon}} \tag{2.6}$$

is used for high frequency low loss attenuation and electrical properties, with σ as conductivity in mS/m.

2.2 Ray-based methods

Standard tomographic inversion of crosshole ground penetrating radar uses the first-arrival travel times and the first-cycle amplitudes of a measured trace and provides information about the electromagnetic velocity and attenuation structure of the subsurface. Two kinds of ray-based theory are possible; the straight ray approach, which is linear between transmitter and receiver, and the curved ray method, which is nonlinear along the path and the velocity can change between a transmitter and a receiver related to Snell's law.

For solving the forward problem, two types of algorithms can be applied. The first method is ray-tracing (Cerveny, 2001; Zelt & Ellis, 1988) and the second is a finite-difference implementation of the Eikonal Equation (Vidale, 1990), for which travel times are needed for all transmitter-receiver combinations. Due to computing times and memory requirements, the ray-tracing is more efficient than finite-difference Eikonal algorithms. However, the ray-tracing can only be applied to smoothly heterogeneous mediums, which can be parameterized effectively with piecewise analytical functions. In comparison the finite-difference Eikonal solver uses a regular grid of points at which the velocities are defined. The grid spacing (horizontal and vertical) must be less than the receiver spacing to avoid discretization errors (Rabbel, 1996). We applied the Eikonal solver for the ray-based inversion. In the following, the theory of the travel time and first-cycle amplitude inversion are explained in more detail.

First-arrival travel time inversion

The first-arrival travel time inversion uses the first-arrival travel times in the data to derive a velocity model for the subsurface. For this process it is necessary to simulate the ray-paths from the transmitters to the receivers. By varying parameters and forward modeling, a velocity distribution can be obtained. In the following an overview is given for the travel time inversion according to Lanz *et al.* (1998) and Rabbel (1996). The inversion can be divided into the following steps:

1. Defining the initial subsurface model;

2. Forward modeling to simulate the travel times for the current model;

3. Estimating the difference between the calculated and observed travel times;

4. Using a computing scheme to convert the estimated differences into an improved model;

5. Updating the model.

Steps 2 - 5 are repeated until the error between the measurement and the calculated data is small enough and a good model is obtained (Rabbel, 1996). The travel time misfit C_{TT} can be described by a squared root function of the difference between the observed and simulated travel times:

$$C_{TT} = \sum_s \sum_r \frac{(t_{sr}^{obs} - t_{sr}^{syn})^2}{n},$$ (2.7)

where t^{obs} and t^{syn} are the observed and synthetic travel times at transmitter and receiver positions x_s and x_r. The number of data points is given by n, where s and r are the source and receiver numbers, respectively.

The forward model calculates the travel times of a transmitter - receiver combination by using the model parameters. The time t that the wave needs to propagate along a ray-path S through a 2D isotropic medium can be described as

$$t = \int_S u(r(x,z))dr,$$ (2.8)

where $u(r)$ represents the slowness field ($u = \frac{1}{v}$) and $r(x,z)$ indicates the position vector. The slowness field can be described by equidimensional cells m in which the slowness u_k (k=1...m) is constant. Thus the i-th travel time of n observations can be expressed by the linear relationship

$$t_i = \sum_{k=1}^m l_{ik} u_k = \mathbf{L}_i \mathbf{u},$$ (2.9)

where l_{ik} stands for the i-th portion of the ray path in the k-th cell of the model space.

To solve the forward problem that calculates $\mathbf{L}$, a fast finite difference Eikonal solver approach is applied, that simulates the propagation of wavefronts through heterogeneous media and subsequently reconstruct the ray paths. Lanz *et al.* (1998) used a modified approach of a brute-force mapping scheme of Schneider *et al.* (1992), where the subsurface is subdivided into a two-dimensional rectangular grid. For each cell the length of the ray-paths can be determined with respect to the slowness field, that are needed to derive the first break picks of the travel times. The lengths of each ray passing a cell are entries of the Jacobian matrix, describing the sensitivities.

In most cases for heterogeneous medium, it is not possible to derive the modeled slowness field $\mathbf{u}$ without additional regularization constrains in form of smoothing and

damping, thus Equation (2.9) can according to (Musil *et al.*, 2003) written as

$$
\begin{bmatrix} \mathbf{t} \\ 0 \\ \mathbf{u}_0 \end{bmatrix} = \begin{bmatrix} \mathbf{L} \\ \mathbf{A} \\ \mathbf{I} \end{bmatrix} \mathbf{u},
\tag{2.10}
$$

where $\mathbf{A}$ is a smoothing matrix, $\mathbf{I}$ corresponds to the identity matrix and $\mathbf{u}_0$ is a vector of damping contains. The matrix on the right side is a sparse matrix. The damping represents a weighting factor, which determines the relative weight of the model regularization with respect to the data and is applied to minimize the amount of deviations from the input model $\mathbf{u}_0$. In contrast, smoothing requests that the difference of adjacent model parameters are small and ensures that distinctive features are only resolved if they really presents the data. The Equation 2.10 can be written in a more compact form as

$$
\mathbf{d} = \mathbf{D}\mathbf{u}
\tag{2.11}
$$

Due to that the $\mathbf{L}$ depends on unknown slowness field $\mathbf{u}$, the inversion problem that intents to minimize the objective function C_{TT} is non-linear and need to be solved iteratively. Hence $\mathbf{D}$ is a sparse matrix, many sparse matrix solvers can be applied. Lanz *et al.* (1998) proposed a least squares (LSQR) approach of Paige & Saunders (1982) based on a conjugate-gradient type method for solving sparse linear Equations and sparse least-squares problems.

A good coverage of the medium with ray-paths is necessary to achieve relevant information about the subsurface. The amount of rays becomes less with increasing depth for surface measurements. For borehole measurements the coverage is lower for the highest and the lowest measurements points. To obtain a suitable start model, it can be required to run several different iterations with different start models to determine the best solution, and a priori information are additionally useful.

First-cycle amplitude inversion

First-cycle amplitude inversion provides information about the subsurface and estimates the electrical conductivity distribution of the medium by obtaining the attenuation structures. The following Equations and assumptions are based on Holliger *et al.* (2001) and Maurer & Musil (2004). For the inversion scheme of the amplitude inversion, additional priori assumptions are necessary such as radiation patterns of the borehole antennas. Assuming that the antennas can be described by infinitesimal dipoles, we can describe the amplitude of the electrical field $\mathbf{E}$ by

$$
\mathbf{E}_{ij} = \frac{A_0 \Theta_{t_i} \Theta_{r_j} e^{-\sum_{k=1}^{m} \alpha_k \mathbf{L}_{ijk}}}{\sum_k \mathbf{L}_{ijk}},
\tag{2.12}
$$

where A_0 symbolizes the source strength, Θ_t and Θ_r are the radiation patterns of the transmitting and receiver antennas, respectively. Here, $\mathbf{L}_{ijk}$ represents the distance over which a certain ray travels through a grid of k cells from source i to receiver j, where α is the constant attenuation of this grid. Equation (2.12) is only valid for a homogeneous medium and the ray paths obtained from the first-arrival travel time inversion are needed.

To achieve a linear form of Equation (2.12) the following substitution is applied, where $\tilde{\boldsymbol{E}}_{ij} = -ln\frac{\mathbf{E}_{ij}\sum\mathbf{L}_{ijk}}{\Theta_{t_i}\Theta_{r_j}}$ and $\tilde{\boldsymbol{A}}_0 = -ln(A_0)$ are used to solve for the attenuation values. Equation (2.12) can now be rewritten as

$$\tilde{\boldsymbol{E}}_{ij} = \sum \alpha_k \mathbf{L}_{ijk} + \tilde{\boldsymbol{A}}_0, \tag{2.13}$$

and takes the same form as the travel time inversion in Equation (2.9), where instead of the slowness the attenuation is used. Similar numerical approaches can be used to solve this Equation as already described for the travel time inversion. In addition, systematic errors, for example antenna-borehole coupling or other systematic effects along the borehole, can be accounted for by extending the first-cycle amplitude inversion (Eq. 2.13) with the introduction of correction factors:

$$\tilde{\boldsymbol{E}}_{ij} = \sum \alpha_k \mathbf{L}_{ijk} + acf_i^t + acf_j^r \tag{2.14}$$

where acf_i^t and acf_i^r are the amplitude correction factors for the i-th transmitter and the j-th receiver, respectively.

2.3 Full-waveform inversion methodology

The workflow of the full-waveform inversion scheme that uses a simultaneous update of the permittivity and conductivity model is shown in Figure 2.1. First, we describe the pre-processing followed by the source wavelet estimation. Then, we discuss the inversion algorithm and implementation details. In 2D the system of Equations 2.1 determines the propagation of the waves in the x-z plane. For most crosshole cases the vertical component of the electrical field is obtained by the standard vertical antenna orientations. Therefore, in the following mainly the TE mode or the transverse electrical mode of the Maxwell Equations is used.

Part I — Pre-processing

- A - Filter out noise
- B - Ray-based inversion and define start model for FWI
- C - 3D to 2D conversion

Part II — Source wavelet estimation

- D - Estimate source wavelet with horizontal rays (more details in Part A Fig. 2.2)
- E - Determine effective source wavlet (more details in Part B, Fig. 2.2)

Part III — Full-waveform inversion

- F - Compute synthetic wavefield
- G - Estimate residual wavefield and calculate cost function
- H - Estimate back-propagated residual wavefield
- I - Cross-correlation of synthetic & backpropagated residual wavefield
- J - Calculate update directions for inversion
- K - Estimate step-lengths
- L - Update ε and σ with gradient and step-length
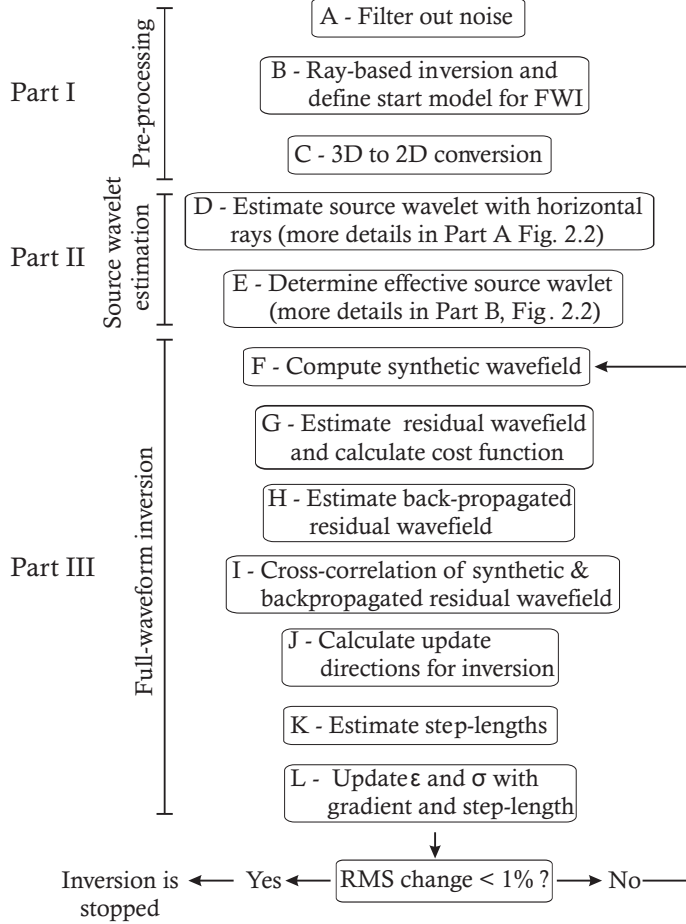
RMS change < 1% ? — Yes → Inversion is stopped / No

Figure 2.1: Full-waveform inversion workflow showing the three main parts: pre-processing, source wavelet estimation and full-waveform inversion. The arrow indicates that these steps should be repeated until the misfit between the observed and synthetic data between sequenced iterative steps is below 1%.

17

2.3.1 Pre-processing

Initially, the data are band-pass filtered to remove noise outside the source spectrum (Fig. 2.1, step A). The starting model is typically obtained by standard ray-based inversion techniques. First-arrival travel times and first-cycle amplitude are used for the ray-based inversion to obtain velocity and attenuation tomograms of the subsurface, which can be transformed into permittivity and conductivity distributions (Fig. 2.1, step B) using Equations 2.5 and 2.6 as

$$\varepsilon = \left(\frac{c}{v}\right)^2 \tag{2.15}$$

$$\sigma = 2 \cdot \alpha \sqrt{\frac{\varepsilon}{\mu}}. \tag{2.16}$$

3D to 2D Conversion

To apply the 2D full-waveform inversion algorithm to experimental data it is necessary to account for the 3D radiation characteristics of electromagnetic wave propagation (see Eq. 2.4). The geometrical spreading describes the decrease of the energy density along a propagating wave front. The wave front area is widening with increasing travel distance. Consequently, the geometrical spreading is different in 2D and 3D cases, as for the 3D case the wave front propagates spherical and the amplitude decay is proportional to the traveled distance, while the wave radius depends on the velocity and time, where $r = vt$ and $A \approx \frac{1}{t}$. In 2D, the energy is spread over the perimeter of the circle, which leads to the geometrical amplitude decay of $A \approx \frac{1}{\sqrt{r}} \approx \frac{1}{\sqrt{t}}$ (Liner, 2004). Therefore, it is necessary to multiply the 3D data with $\sqrt{t}$ when using a 2D code. Furthermore, in 2D the sources are implicitly considered as infinitive long extended lines of point dipole in the perpendicular direction of the 2D plane. This is not true in reality, thus a phase shift must be introduced.

Similar to Ernst *et al.* (2007b), we apply a 3D to 2D transformation technique developed by Bleistein (1986) to compensate for differences in geometrical spreading and pulse shape (frequency scaling and phase shifting; Fig. 2.1, step C). The transformation uses a phase shift of $\pi/4$ and a scaling factor of $1/\sqrt{\omega}$ in the frequency domain. This is expressed by

$$\hat{\mathbf{E}}^{2D}(\mathbf{x}_{trn}, \mathbf{x}_{rec}, \omega) = \hat{\mathbf{E}}^{obs}(\mathbf{x}_{trn}, \mathbf{x}_{rec}, \omega) \sqrt{\frac{2\pi t(\mathbf{x}_{trn}, \mathbf{x}_{rec})}{-j\omega \varepsilon^{mean}\mu}}. \tag{2.17}$$

The left side of the Equation shows the corrected data $\hat{\mathbf{E}}^{2D}$ for the transmitter at location x_{trn} and receiver x_{rec}. On the right side $\hat{\mathbf{E}}^{obs}$ denote the original measured data and $t(x_{trn}, x_{rec})$ are the travel times (account for 3D to 2D geometrical spreading); ε^{mean} is the

mean dielectric permittivity of the media; ˆ indicates the frequency domain. Ernst *et al.* (2007b) denoted, by testing this approach, that a good agreement can be achieved between 3D and corresponding pure 2D data in the far-field.

Due to the measurement behavior of the antennas for crosshole equipment (single-component antennas), it is not really possible to distinguish between out-of-plane and in-plane events. However, we assume, that most of the energy comes from in-plan events linked to the media in the first few cycles of the traces. To minimize the problem with out-off plane effects, only the first few cycles of the measured traces FDTD can be used for the inversion by reducing the time window (Ernst *et al.*, 2007b).

2.3.2   Forward Problem

For the source wavelet estimation and the full-waveform inversion, a forward modeling tool is necessary, that simulates the entire EM field based on the Maxwell Equations for given model parameters. In contrast, for the ray-based inversion only the ray-paths of the wave through the model are simulated. To solve the forward problem for the full-waveform inversion, a 2-D finite-difference time-domain (FDTD) solution of the Maxwell Equations in Cartesian coordinates is applied (Meles *et al.*, 2010). Finite-difference is a grid-based differential time domain numerical modeling method to find a numerical solution of time-dependent differential Equations such as Equation (2.1). The main idea is the approximation of partial derivatives by finite differences. The system of Equations of (2.1) is solved by using an FDTD technique based on staggered-grid finite-differences operators, which are second order operators in space and time. To reduce artefacts from reflections at the boundaries and edges of the model space generalized perfect matched layers (GPML) are implemented. These layers absorb waves at the model boundary to avoid back-reflection of waves into the medium (Ernst *et al.*, 2006; Berenger, 1994). In the following steps, the forward modeling is necessary for the correction of the effective source wavelet and during the full-waveform inversion four times for each transmitter position. Consequently, a large amount of computing resources is necessary for the inversion.

2.3.3   Source wavelet estimation

Next, the unknown effective source wavelet is estimated. The source wavelet estimation (Fig. 2.1, steps D and E) is a critical step for the inversion. Only through obtaining an effective source wavelet, it is possible to match the measured waveforms, including any small nuances that may be present. This wavelet not only reflects the current density pattern of the finite length GPR antenna, but also the influence of water- or gas-filled

boreholes. The steps in the source wavelet estimation are illustrated in detail in Figure 2.2 extended from Ernst *et al.* (2007b).

First, an initial source wavelet is estimated (Fig. 2.2, Part A), where only the shape of the wavelet is determined without considering any amplitude information. All traces from a vertical zero-offset profile, containing only horizontally traveling waves, are normalized and aligned to estimate an average pulse (Fig. 2.2, step 1). By cross-correlating the zero-offset profile traces, data containing erroneous wave shapes due to for example interfering reflections are identified and excluded. To reduce the noise of the measured data the upper and lower neighbors of the receivers are also taken and a mean trace is calculated. We know from Maxwell Equations that the electric field is proportional to the time derivative (multiplication with $j\omega$ in the frequency domain, see Eq. 2.4) of the current density source wavelet. To obtain the shape of the initial source wavelet we divide the average Fourier transformed selected electric field pulse by $j\omega$ in the frequency domain (Fig. 2.2, step 2).

In Part B (Fig. 2.2), we calculate a corrected wavelet with detailed amplitude and phase characteristics. The forward modeling is performed using the 2D FDTD code of Ernst (2007). The synthetic radargrams $\mathbf{E}^{syn}$, for each transmitter-receiver position are calculated using the model of permittivities and conductivities obtained from the ray-based inversion (indicated by ε_{ray} and σ_{ray}) and the initial source wavelet (Fig. 2.2, step 3 and 4). The radar data can be mathematically seen as the convolution of the source wavelet with the impulse response of the earth (Green's function) in the time-domain, or, as the multiplication of the source spectrum with the Fourier-transformed Green's function (Eqs 2.2 and 2.3). Therefore, an effective source wavelet can be obtained by deconvolving the radar data $\hat{\mathbf{E}}^{obs}$ with an appropriate Green's function $\hat{\mathbf{G}}$ calculated using the travel time inversion results as input. This is best done using a least-squares approach in the frequency domain (Ernst *et al.*, 2007b; Streich, 2007b). The transfer function $\hat{\mathbf{G}}$ is calculated by spectral division of $\hat{\mathbf{E}}^{syn}$ in the frequency domain with the initial wavelet spectrum $\hat{\mathbf{S}}_{k=0}$ for each separate trace (Fig. 2.2, step 5). Next, we estimate $\hat{\mathbf{S}}_{k=1}$ by dividing the actual observed data $\hat{\mathbf{E}}^{obs}$ with the transfer function $\hat{\mathbf{G}}$, using all traces in a least-squares sense (Fig. 2.2, step 6). Quantities η_D and η_I are prewhitening factors that are applied to stabilize the solution and avoid a division by zero when notches are present in the spectrum of $\mathbf{G}$. The time-domain source wavelet $\mathbf{S}_{k+1}(t)$ is obtained by an inverse Fourier transformation (Fig. 2.2, step 7). Steps 3 - 7 can be repeated until the source wavelet has converged (loop 1), where k indicates the iteration number. In Part C (Fig. 2.2) a source wavelet refinement can be applied during the full-waveform inversion after several iterations to improve the wavelet when necessary (loop 2).

Part A
Initial Source
wavelet estimation

step 1 — Determine average pulse by using mainly horizontal rays

step 2 — divide by $j\omega$

$\mathbf{S}_{ini}(t)$

$\mathbf{S}_{k=0}(t) = \mathbf{S}_{ini}(t); \varepsilon_{k=0} = \varepsilon_{ray}; \sigma_{k=0} = \sigma_{ray}$

Part B
Source wavelet
correction

step 3 — Initial forward modeling

step 4 — $\mathbf{E}^{syn}(\varepsilon_k, \sigma_k, \mathbf{S}_k(t), t)$

FFT$\{\mathbf{S}_k(t)\}$, FFT$\{\mathbf{E}^{syn}(t)\}$

step 5 — $\hat{\mathbf{G}}(f) = \hat{\mathbf{E}}^{syn}(f)\left[\hat{\mathbf{S}}_k(f) + \eta_D\right]^{-1}$

FFT$\{\mathbf{E}^{obs}(t)\}$

step 6 — $\hat{\mathbf{S}}_{k+1}(f) = \left[\hat{\mathbf{G}}(f) + \eta_I\right]^{-1}\hat{\mathbf{E}}^{obs}(f)$

IFFT$\{\hat{\mathbf{S}}_{k+1}(f)\}$

step 7 — $\mathbf{S}_{k+1}(t)$

Source wavelet refinement required? — Yes

$k=k+1$ Loop 1 — $k=k+1$ Loop 2

Part C
Full-waveform
inversion
(more details in Part III Fig. 2.1)

$\varepsilon_{k=0} = \varepsilon_{ray}$
$\sigma_{k=0} = \sigma_{ray}$

No

Waveform Inversion — No — Source wavelet refinement required? — Yes

$k=k+1$

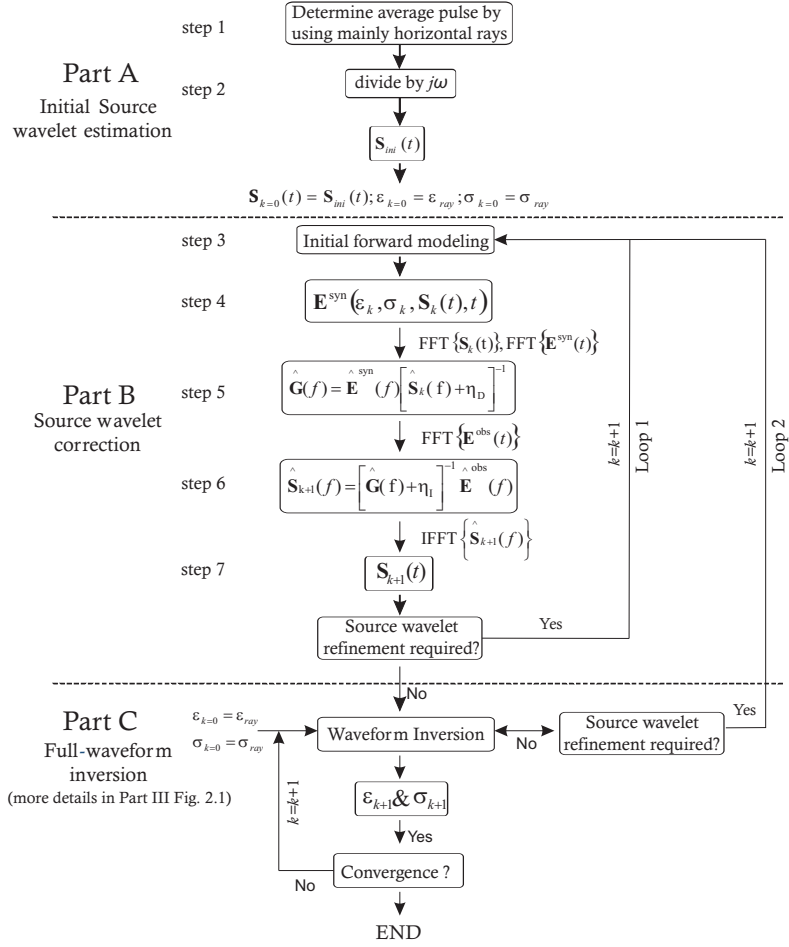ε_{k+1} & σ_{k+1} — Yes

Convergence ? — No

END

Figure 2.2: Source wavelet estimation flow consisting of three parts: Part A: initial source wavelet estimation using averaged horizontal rays (steps 1 - 2), Part B: the source wavelet correction (steps 3 - 7) with the deconvolution method using all available data (extended from Ernst *et al.* (2007b)) and Part C: source wavelet refinement during the full-waveform inversion. The source wavelet estimation is always carried out before starting the full-waveform inversion (loop 1) and can also be performed after several iterations of the full-waveform inversion (loop 2).

2.3.4   Inversion algorithm

Using the estimated starting model and effective source wavelet we compute the initial full-waveform model synthetic radar waveforms that should match the observation within half the dominant pulse period, otherwise the inversion will proceed to update in the wrong direction and result in a phenomenon called local minimum trapping (Meles *et al.*, 2011).

Inverse Problem

The full-waveform inversion is based on Tarantola's approach (1984a,b, 1986) that uses a conjugate gradient method. This approach involves finding the spatial distribution of the permittivity and conductivity that minimize the cost (misfit) function C_{FW} in an iterative approach between the modeled $\mathbf{E}^s$ and measured $\mathbf{E}^s_{obs}$ traces for all transmitter-receiver combinations within a defined time window (Fig. 2.1, Part III). This is achieved by computing the gradient of $\mathbf{C}_{FW}$, which indicates the update direction of the permittivity and conductivity models. Furthermore, individual step-lengths need to be determined that indicate the magnitude of the model updates. Using the vector formalism introduced by Meles *et al.* (2010) and Equations 2.2 the misfit function can be written as

$$C_{FW}(\varepsilon, \sigma) = \frac{1}{2} \sum_s \sum_r \sum_\tau [\mathbf{E}^s(\varepsilon, \sigma) - \mathbf{E}^s_{obs}]^T_{r,\tau} \, \delta(\mathbf{x} - \mathbf{x}_r, t - \tau) \, [\mathbf{E}^s(\varepsilon, \sigma) - \mathbf{E}^s_{obs}]_{r,\tau} \, , \quad (2.18)$$

where $\mathbf{E}^s$ stands for the electric field of a particular source and contains the entire space-time domain, superscript T indicates the transposed operator, and s, r, and τ indicate sums over sources, receivers, and observation times. The difference between the cost functions C_{TT} (Eq. 2.7) and C_{FW} (Eq. 2.18) is that in the full-waveform inversion the complete traces of the electrical field $\mathbf{E}^s$ are taken into account, whereas for the travel time inversion only the first-arrivals t are used.

To calculate the gradient ∇C, the forward propagated wave field $\mathbf{E}^{syn}$ is computed using the estimated source wavelet and the model from the previous inversion iteration (or the ray-based inversion model for the first iteration). The wave fields are stored in memory for each transmitter and each time step (Fig. 2.1, step F). The gradient ∇C can be estimated as described by Meles *et al.* (2010). The Maxwell Equations are rewritten for a perturbed system, which describes the changes in the measured wave field due to permittivity and conductivity changes as follows:

$$\mathbf{E}^s(\varepsilon + \delta\varepsilon, \sigma + \delta\sigma) - \mathbf{E}^s(\varepsilon, \sigma) = \hat{\mathbf{G}}(\partial_t \mathbf{E}^s \delta\varepsilon + \mathbf{E}^s \delta\sigma) = \begin{bmatrix} \mathbf{L}^s_\varepsilon & \mathbf{L}^s_\sigma \end{bmatrix} \begin{bmatrix} \delta\varepsilon \\ \delta\sigma \end{bmatrix}. \quad (2.19)$$

Here, the sensitivity operator $\mathbf{L}^s$ is defined for the individual contributions of permittivity and conductivity perturbations with

$$\mathbf{L}^s_\varepsilon(\mathbf{x}') = \hat{\mathbf{G}}\delta(\mathbf{x} - \mathbf{x}')\partial_t \mathbf{E}^s, \qquad (2.20)$$

$$\mathbf{L}^s_\sigma(\mathbf{x}') = \hat{\mathbf{G}}\delta(\mathbf{x} - \mathbf{x}')\mathbf{E}^s. \qquad (2.21)$$

Gradients of the misfit function

The gradient of the cost function can be estimated by taking the first order approximation of the cost function in Equation 2.18:

$$C_{FW}(\varepsilon + d\varepsilon, \sigma + d\sigma) = C_{FW}(\varepsilon, \sigma) + \nabla C_{FW}^T \begin{bmatrix} \delta\varepsilon \\ \delta\sigma \end{bmatrix} + O(\delta\varepsilon^2, \delta\sigma^2). \qquad (2.22)$$

The total gradient ∇C_{FW} is estimated by first calculating all separate contributions for each source, receiver and observation time combination terms of Equation (2.18) and in the second step by adding all these gradient terms. By introducing the residual wave field, which is calculated by subtracting the synthetic wave field from the observed wave field (Fig. 2.1, step G) for each transmitter

$$[\Delta\mathbf{E}^s]_{r,\tau} = \delta(\mathbf{x} - \mathbf{x}_r, t - \tau)\left[\mathbf{E}^s(\varepsilon, \sigma) - \mathbf{E}^s_{obs}\right]_{r,\tau}, \qquad (2.23)$$

and applying $\mathbf{L}_s$ to this residual, the gradient of the misfit function as summation over all sources s can be written as

$$\begin{bmatrix} \nabla C_\varepsilon(\mathbf{x}') \\ \nabla C_\sigma(\mathbf{x}') \end{bmatrix} = \sum_s \begin{matrix} (\delta(\mathbf{x} - \mathbf{x}')\partial_t\mathbf{E}^s)^T\hat{\mathbf{G}}^T\mathbf{R}^s \\ (\delta(\mathbf{x} - \mathbf{x}')\mathbf{E}^s)^T\hat{\mathbf{G}}^T\mathbf{R}^s \end{matrix}, \qquad (2.24)$$

with $\mathbf{R}^s$, which is a summation over all receiver and observation times, as the generalized residual wave field

$$\mathbf{R}^s = \sum_r \sum_\tau [\Delta\mathbf{E}^s]_{r,\tau}. \qquad (2.25)$$

where $\hat{\mathbf{G}}^T\mathbf{R}^s$ can be interpreted as the back-propagated residual wave field in the same medium as $\mathbf{E}^s$. The spatial delta function $\delta(\mathbf{x} - \mathbf{x}')$ corresponds to the spatial components of the gradients and reduces the inner product to a zero-lag cross-correlation in time.

This Equation is the core of the full-waveform inversion and is illustrated in Figure 2.3. $\mathbf{E}^s$ is the electrical field in the current model for a source at x^s and is stored in memory for each source and each time step (Figs 2.1, step F and 2.3a). In the second step, the residual wave field $\hat{\mathbf{G}}^T\mathbf{R}^s$ is back-propagated from all receivers to the corresponding

a)   b)   c)

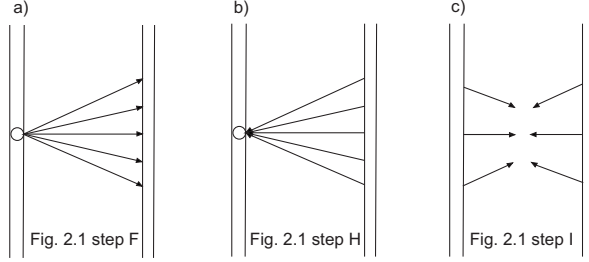Fig. 2.1 step F   Fig. 2.1 step H   Fig. 2.1 step I

Figure 2.3: Illustration of the a) forward propagation of the electrical field due to a source at position x^s; b) backward propagation of the residual wave field calculated at the receiver position; c) zero-lag cross-correlation of both wave fields and summing over all times and sources.

transmitters through the model at the same time (Fig. 2.1, step H). Finally, the gradient at each point x is obtained by a zero-lag cross-correlation of the stored values of $\mathbf{E}^s$ with the back-propagated residual wave field and by summing over all transmitters and times (Fig. 2.1 step I and J, and see Fig. 2.3c).

Equations (2.24) and (2.25) describe, that if at a certain location in space the medium properties deviate from the current model medium parameters, a residual wave field will be present (Eq. 2.23 and Fig. 2.3a). When this residual wave field is back-propagated and cross-correlated with the already calculated electrical field (Eqs 2.24 and 2.25) constructive interferences will occur at exactly at that position in space where the medium properties deviated. The gradient calculated with Equation (2.24) indicates how to change these medium properties to reduce the misfit function.

Step-lengths

After estimating the permittivity and conductivity gradients (Fig. 2.1, step J), the step-lengths are calculated (Fig. 2.1, step K). These step-lengths are necessary to update the permittivity and conductivity model in each iteration. In general, permittivity and conductivity can be updated by :

$$\left[\ \varepsilon_{upd}\ \right] = \left[\ \varepsilon\ \right] - \zeta \cdot \left[\ \nabla C_\varepsilon\ \right], \tag{2.26}$$

$$\left[\ \sigma_{upd}\ \right] = \left[\ \sigma\ \right] - \zeta \cdot \left[\ \nabla C_\sigma\ \right]. \tag{2.27}$$

By searching for the minimum of the object function C along the gradient, the step-length ζ can be obtained by setting the first derivative to zero.

For large differences between the permittivity and conductivity sensitivities the simultaneous inversion, which uses the same step-length for both parameters, could fail for complex models. Therefore, Ernst *et al.* (2007a) applied a stepped (cascaded) inversion, where first the permittivity is inverted, while leaving the conductivity constant for several iterations. Then the conductivity is inverted, while the permittivity is fixed for several iterations. In contrast, Meles *et al.* (2010) introduced individual step-lengths that allows a simultaneously update of the permittivity and conductivity models in each iteration. By using the ∇C_ε and ∇C_σ two step-lengths in a quasi-simultaneous approach can be derived by

$$\left[\begin{array}{c} \varepsilon_{upd} \end{array} \right] = \left[\begin{array}{c} \varepsilon \end{array} \right] - \zeta_\varepsilon \cdot \left[\begin{array}{c} \nabla C_\varepsilon \end{array} \right], \tag{2.28}$$

$$\left[\begin{array}{c} \sigma_{upd} \end{array} \right] = \left[\begin{array}{c} \sigma \end{array} \right] - \zeta_\sigma \cdot \left[\begin{array}{c} \nabla C_\sigma \end{array} \right]. \tag{2.29}$$

From Equation (2.24) it can be seen that the permittivity gradient can be obtained from the conductivity gradient using:

$$\nabla C_\varepsilon = \partial_t \nabla C_\sigma. \tag{2.30}$$

Next, the step-length ζ_ε and ζ_σ are calculated which follow the gradient to minimize the cost function. For this purpose the appropriate perturbation factors κ_ε and κ_σ are introduced and the step-lengths are obtained as:

$$\zeta_\varepsilon = \kappa_\varepsilon \frac{\sum_s \sum_r \sum_\tau \left[\mathbf{E}(\varepsilon + \kappa_\varepsilon \nabla S_\varepsilon, \sigma) - \mathbf{E}^s(\varepsilon, \sigma) \right]_{r,\tau}^T \delta(\mathbf{x} - \mathbf{x}_r, t - \tau) \left[\mathbf{E}^s(\varepsilon, \sigma) - \mathbf{E}^s_{obs} \right]_{r,\tau}}{\sum_s \sum_r \sum_\tau \left[\mathbf{E}^s((\varepsilon + \kappa_\varepsilon \nabla S_\varepsilon, \sigma) - \mathbf{E}^s(\varepsilon, \sigma) \right]_{r,\tau}^T \delta(\mathbf{x} - \mathbf{x}_r, t - \tau) \left[\mathbf{E}^s((\varepsilon + \kappa_\varepsilon \nabla S_\varepsilon, \sigma) - \mathbf{E}^s(\varepsilon, \sigma) \right]_{r,\tau}}, \tag{2.31}$$

and

$$\zeta_\sigma = \kappa_\sigma \frac{\sum_s \sum_r \sum_\tau \left[\mathbf{E}^s(\varepsilon, \sigma + \kappa_\sigma \nabla S_\sigma) - \mathbf{E}^s(\varepsilon, \sigma) \right]_{r,\tau}^T \delta(\mathbf{x} - \mathbf{x}_r, t - \tau) \left[\mathbf{E}^s(\varepsilon, \sigma) - \mathbf{E}^s_{obs} \right]_{r,\tau}}{\sum_s \sum_r \sum_\tau \left[\mathbf{E}^s((\varepsilon, \sigma + \kappa_\sigma \nabla S_\sigma) - \mathbf{E}^s(\varepsilon, \sigma) \right]_{r,\tau}^T \delta(\mathbf{x} - \mathbf{x}_r, t - \tau) \left[\mathbf{E}^s(\varepsilon, \sigma + \kappa_\sigma \nabla S_\sigma) - \mathbf{E}^s(\varepsilon, \sigma) \right]_{r,\tau}}. \tag{2.32}$$

Note that, the perturbation factors need to be carefully chosen, such that they are small enough to guaranty that the perturbed model still lies in the linearity range to avoid overshooting of the inversion, and large enough, to avoid round-off errors of the computer system while dealing with small numbers (Meles *et al.*, 2010).

Finally, the permittivity and conductivity at the current iteration are updated with the obtained gradient directions and step-lengths (Fig 2.1, step L) using Equation 2.28 and 2.29. In the first iteration of the full-waveform inversion, we use the obtained permittivity and conductivity models of the ray-based inversions to calculate the modeled data. In subsequent iterations, steps F - L are repeated using the updated model until the change in the misfit function C_{FW} between two subsequent iterations is approximately less than 1% and no significant gradient is present (Ernst *et al.*, 2007b).

Parametrization of the physical System

Ernst *et al.* (2007a) and Meles *et al.* (2010) applied a logarithmic scaled version for the unknown parameters by following Tarantola's approach

$$\tilde{\varepsilon} = log\frac{\varepsilon}{\varepsilon_0} = log(\varepsilon_r), \tag{2.33}$$

$$\tilde{\sigma} = log\frac{\sigma}{\sigma_0} = log(\sigma). \tag{2.34}$$

where σ_0 is 1 S/m. Such a logarithmic scaling is necessary, because it gives the models space a linear structure and ensures further positive values for the permittivity and conductivity within a wider range of the values. $\tilde{\varepsilon}$ and $\tilde{\sigma}$ are the modified parameters and by using Equations (2.33) and (2.34) the gradient function is changed and can be rewritten by using

$$C(\varepsilon(\tilde{\varepsilon}), \sigma(\tilde{\sigma})) = C'(\tilde{\varepsilon}, \tilde{\sigma}) \tag{2.35}$$

2.3.5   Implementation details

The computational costs of the full-waveform inversion are determined mainly by the FDTD calculations. The full-waveform algorithm requires the solution of the forward problem four times during each iteration. With the first solution the residual wave field is calculated, the second solution is required to compute the model update directions (gradients) and two FDTD calculations are needed for determining the step-lengths. The calculations for each transmitter position are independent from each other. Therefore, the algorithm can be easily parallelized. For each transmitter one slave CPU is required and one master CPU coordinates the communication and computation of the gradients and model updates. The overhead for the distribution of the computations is about 10 % using the MPI system (Ernst *et al.*, 2007a). During the calculation of the gradient, the forward modeled field $\mathbf{E}^s$ remains in the computer memory. The required memory $\mathbf{M}$ is estimated by

$$M = \frac{nx_f \cdot nz_f \cdot timesteps \cdot 2 \cdot 8}{inv/fwd \cdot inv/fwd} \cdot N_{TRN}, \tag{2.36}$$

where nx_f and nz_f are the numbers of the horizontal and vertical forward modeling cells, the value 2 indicates the two components ($\mathbf{E}_x$ and $\mathbf{E}_z$) of the electric field, the 8 stands for double-precision number representation in bytes of the electric field values and $\mathbf{N}_{TRN}$ is the number of transmitters. Due to memory constraints, each inversion cell consists of $inv/fwd = 3$ forward modeling cells in the x and z directions, which is stated by the square of the factor inv/fwd. The computation time can be calculated using

$$T_{comp} = 4 \cdot 1.1 \cdot T_{forward} \cdot N_{iter}, \tag{2.37}$$

where $T_{forward}$ is the time for a single FDTD calculation and N_{iter} is the number of iterations (Meles *et al.*, 2010). Most of the full-waveform calculations are conducted on the JUROPA cluster (Research Center Jülich), shown in Figure 2.4.

Figure 2.4: Image of the high performance JUROPA Cluster located in the JSC Forschungszentrum Jülich
(www.fz-juelich.de/ias/jsc/EN/Expertise/Supercomputers/JUROPA/).

Chapter 3

Applications of the full-waveform inversion to experimental data: case study of the Thur River hydrogeophysical test site [1] [2]

In this chapter, we explore the potential and limitation of the ray-based and the full-waveform inversion using an experimental data set. First, we describe the field site and the survey geometry. Then, we show the ray-based inversion results, present the procedure to estimate the effective source wavelet and describe the influence of the starting model on the full-waveform inversion results by applying two different starting models. The first starting model is based on the ray-based inversion results, whereas the second starting model is improved to guaranty reliable inversion results for the entire saturated domain by incorporating on overlying unsaturated domain.

---

[1]adapted from Klotzsche, A., van der Kruk, J., Meles, G. A., Doetsch, J., Maurer, H. and Linde, N., 2010, Near Surface Geophysics, 8, 635-649, doi:10.3997/1873-0604.2010054

[2]adapted from Klotzsche, A., van der Kruk, J., Meles, G. A. and Vereecken, H., 2012, Geophysics, 77, H57-H62, doi:10.1190/geo2011-0458.1

3.1 Thur River hydrogeophysical test site and field experiment

The crosshole GPR data set was acquired in the Thur valley close to Frauenfeld, Switzerland. The Thur valley was initially formed by glaciers during the Pleistocene, which cut into the older underlying Tertiary bedrock. Today, the valley is filled with lacustrine sediments and the central part of the Thur River is 40 m - 45 m wide. On the south side of the Thur River, an overbank was formed with an approximate width of 130 m. The aquifer comprises a 7 m thick glaciofluvial gravel deposit (Fig. 3.1), which is embedded between a 3 m thick alluvial loam (silty sands) at the top and low permeability clay aquitard (lacustrine sediments) below 10 m depth (Cirpka *et al.*, 2007). Within the framework of the RECORD project (www.cces.ethz.ch/projects/nature/Record), four 11.4 cm diameter monitoring wells were installed in 2007 close to the Thur River shown in Figure 3.2, where measurements of crosshole GPR, ERT and seismic data have been performed (Doetsch *et al.*, 2010a,b). We consider in this chapter only the crosshole GPR data of the saturated aquifer acquired along the south-west plane of the six planes interpreted by Doetsch *et al.* (2010a,b).
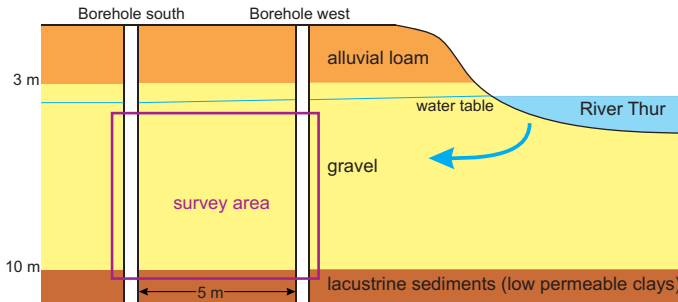

Figure 3.1: Simplified geological representation of the experimental area, showing a three-layer structure: alluvial loam, gravel, lacustrine (clay) sediments (from top to bottom); with boreholes close to the Thur River. The water table is approximately at 4.2 m depth. The purple box indicated the area of interest for the inversions.

A limited number of transmitter positions were used during the data acquisition to minimize acquisition time. To ensure that enough information is captured to reliably invert the data, a much larger number of receiver positions were occupied. The disadvantage of this approach is that ray coverage close to the transmitter borehole is relatively low (see Fig. 3.3a). This is overcome by using a semi-reciprocal transmitter-receiver setup shown in Figure 3.3b, in which transmitter and receiver boreholes are interchanged. The combina-
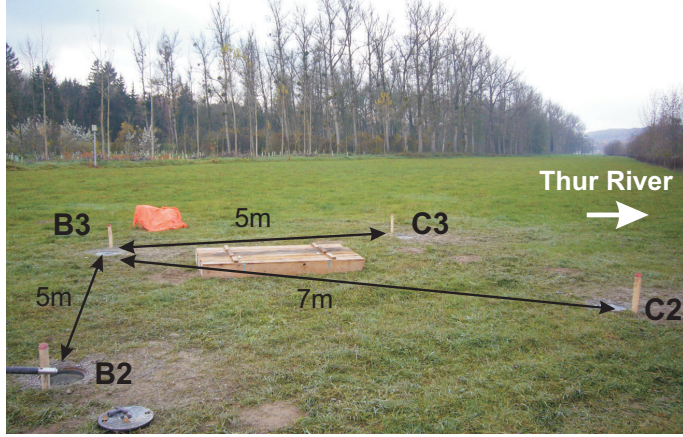
Figure 3.2: Picture of the setup of the four installed 11.4 cm boreholes during the drilling process (Picture provided by Joseph Doetsch). The white arrow indicated the direction of the Thur River.

tion of both data sets results in adequate ray-coverage over the entire domain (Fig. 3.3c). In addition, this setup also reduces next to the acquisition time the computational costs, due to the parallelized full-waveform inversion code, where for each transmitter position one CPU is necessary (see Eq. 2.24). Appendix A (Oberröhrmann *et al.*, 2013) demonstrated that our employed semi-reciprocal setup gives the best compromise between resolution and computational cost out of a few tested configurations. Thereby, a resolution analysis was applied to the full-waveform inversion results for different transmitter-receiver configurations for experimental data. Next to our employed setup, two one-sided setups were tested with a sampling of 0.1 m for the receivers and a sampling for the transmitters of either 0.1 m or 0.5 m.

For the GPR measurements, a RAMAC Ground Vision system of MalåGeoscience with 250 MHz antennas was employed. For the purpose of characterizing the aquifer between 4 m - 10 m depth, we used 12 transmitter positions at a vertical sample interval of 0.5 m in the south borehole and 59 receiver positions at 0.1 m spacing in the west borehole (SW setup). We then exchanged the receiver and transmitter borehole and repeated the acquisition with 12 transmitter and 57 receiver positions in the west and south borehole, respectively (WS-setup, see also Fig. 3.3). Figure 3.4a the recording configuration in which the blue crosses represent transmitter positions and the white circles receiver positions. Consequently, we obtained dense ray coverage between the 5 m separated boreholes over the depth range 4.2 m - 10 m below the water table (at approximately 4.2 m depth) and at the same time optimize the acquisition time and
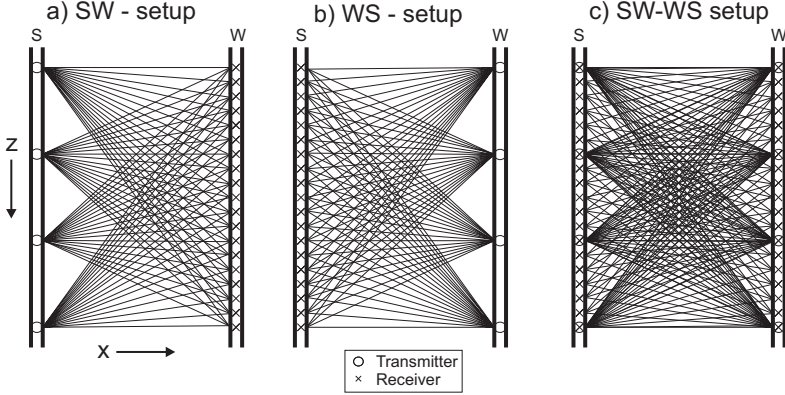
Figure 3.3: Schematic of the measurement setup employed that requires significantly less transmitter than receiver position, but has low ray-coverage in the transmitter borehole. Semi-reciprocal measurements, in which transmitter and receiver boreholes are interchanged, are indicated in a) and b). The combination of these measurements, shown in c), improves the ray-coverage compared to the individual setups.

computer resources needed for the inversion. Due to the measurement setup, the receiver records rays up to an angle of approximately 50°. The zone above the water table is neither included in the measurements nor in the inversion volume, so any recorded signals that have refracted/reflected from this horizon are not accommodated in the forward modeling and inversion.

3.2 Initial model estimation using the ray-based inversion scheme

The first step in the processing sequence consists of picking the first-arrival travel times and the first-cycle amplitudes of the measured data. The ray-based inversion is performed by minimizing the misfit between the picked travel times and the first-cycle amplitudes of the measured and calculated data for a given fixed model regularization that includes both damping and smoothness constraints (Holliger *et al.*, 2001; Maurer & Musil, 2004). The obtained velocity and attenuation tomograms are transformed into permittivity and conductivity images (Figs 3.4a and b). Both permittivity and conductivity images reveal roughly three zones. A zone of higher permittivity and higher electrical conductivity is obtained in the top 4 m - 5.5 m, followed by lower permittivity and lower conductivity values between 5.5 m - 8 m. The bottom part exhibits intermediate values for both parameters.

Neglecting the critically refracted waves results in a low ray density in the uppermost part of the tomographic plane. In addition, the high permittivities (low velocities) cause most of the rays to avoid the upper part (Fig. 3.4c). Therefore, small-scale features found within this zone should be viewed with caution and not be over-interpreted. Other geophysical studies confirmed 3 layers in the saturated aquifer system (Doetsch *et al.*, 2010a,b; Diem *et al.*, 2010; Coscia *et al.*, 2011). A first layer between 4 m - 6 m depth indicated low velocities and resistivities, a second layer between 6 m - 8 m showed high velocities and high resistivities, and a third layer below 8 m showed intermediate values for both parameters (Doetsch *et al.*, 2010b; Coscia *et al.*, 2011).
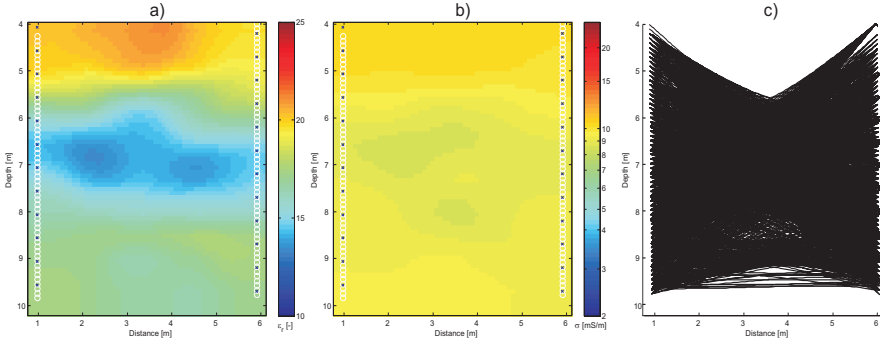

Figure 3.4: Ray-based inversion results that are used as the initial model for the full-waveform inversion. a) The distribution of permittivity and b) conductivity; transmitter and receiver positions are indicated with crosses and circles, respectively. c) The ray-coverage based on the travel time inversion.

3.3   Source wavelet estimation

Before the source wavelet estimation can be performed, it is necessary to apply a 3D to 2D conversion to transform the 3D field data to make them comparable with the 2D modeling data, i.e., synthetic traces (Ernst *et al.*, 2007b) using Equation (2.17). These transformed data are then used in all the following processing steps, as well as in the full-waveform inversion.

3.3.1   Initial source wavelet estimation

Following the scheme outlined in Figure 2.2 Part A, the traces of one upper and one lower neighboring receivers of the zero-offset profile data are averaged to reduce the noise.

Then the similarity of these waveforms obtained for each transmitter is investigated using a cross-correlation procedure for the obtained waves. Waveforms having relative cross-correlation values below 0.8, which indicate significant differences, are discarded. Waveforms of SW-transmitters 1, 2 and 12 and WS-transmitters 13, 14, 23 and 24 are excluded.

In the next step, all traces are aligned to the largest pulse minimum, which results in a better alignment than using the largest maximum of the pulses as used by Ernst *et al.* (2007b) and integrated (see also Fig. 2.2). A band-pass filter is applied in the frequency domain to remove frequencies below 40 MHz and above 150 MHz. The tapered and normalized initial wavelet is plotted in blue in Figure 3.5. Note, that only the shape is estimated and the amplitude scale is not considered.
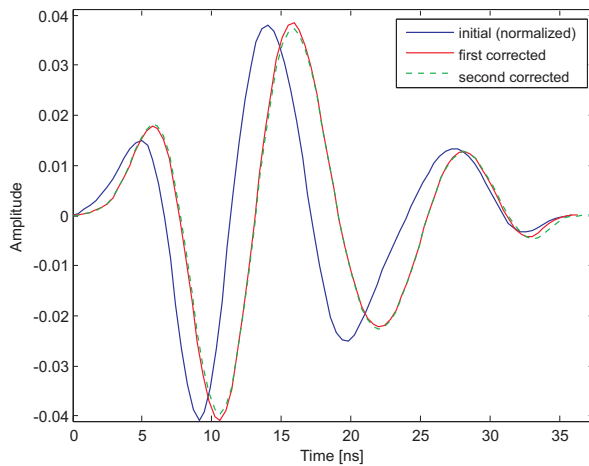

Figure 3.5: Wavelets for different processing steps: the initial wavelet that is normalized to the maximum amplitude of the first corrected wavelet (blue), first corrected wavelet (red) and the second corrected wavelet (green).

The initial source wavelet is employed for modeling the radargrams using the ε_r and σ distributions obtained from the ray-based inversion. In Figure 3.6, the experimental data for the SW-setup are compared with the modeled data. The amplitudes for each trace are normalized to the maximum to enable a better comparison of the shape of the data. Negative and positive amplitudes are indicated by the blue and red color in the image, respectively. The images show a similar trend for both data sets. However, a time shift of about 3 ns is apparent, especially in Figures 3.7a - c, where the observed and modeled data are compared in more detail. Normalized wiggle plots are shown for the selected transmitter positions 2, 7 and 11, respectively, of the SW-setup with their respective receivers. The red and blue traces show the observed and modeled traces, respectively.

Only traces containing waves that mainly traveled horizontal paths show a good fit with the modeled data (green ellipses). High-angle data contain significant time shifts and transmitters close to the water table have a significant misfit, which is probably due to reflections being present in the top 20 traces from transmitters 2 and 7. Similar results are obtained for the WS-setup.
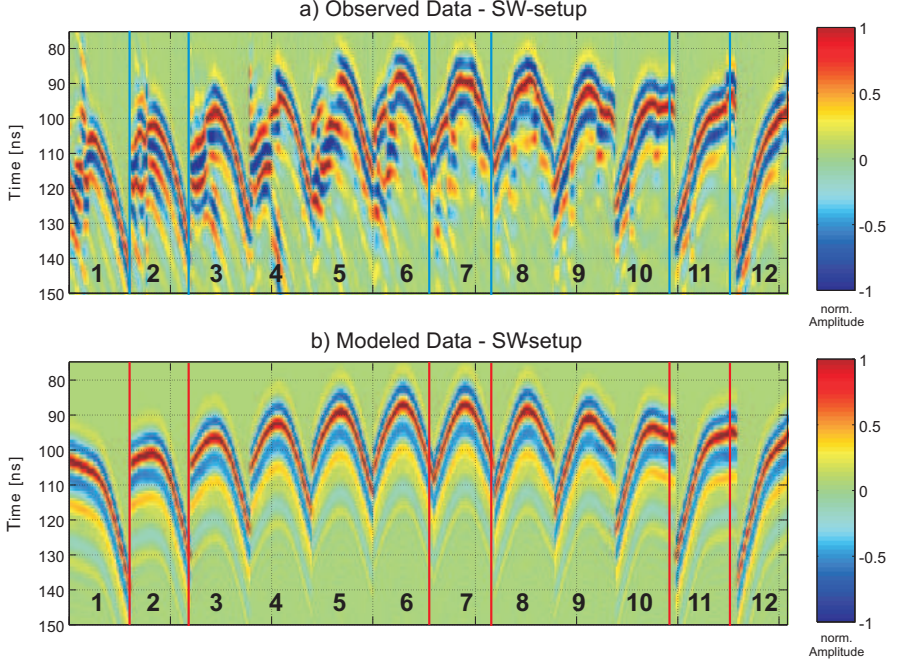

Figure 3.6: Comparison after one forward modeling run of the observed a) and modeled b) data for the SW-setup (amplitudes normalized to their maximum). The numbers indicate the transmitter positions. Wiggle trace plots for observed and modeled data for transmitters 2, 7 and 11 are shown in Figures 3.7a - c, respectively.

3.3.2 Source wavelet correction and refinement

In the next step, the source wavelet is corrected according to Figure 2.2, Part B. In contrast to the initial source wavelet estimation, where only horizontal rays were considered, we now use all traces to estimate the corrected wavelet. The amplitude and phase spectra of the wavelets are shown in Figures 3.8a and b, respectively. The blue, red and dashed black lines show the initial wavelet, the wavelet after the deconvolution and the final corrected wavelet, respectively. The corner frequencies of the band-pass filter applied
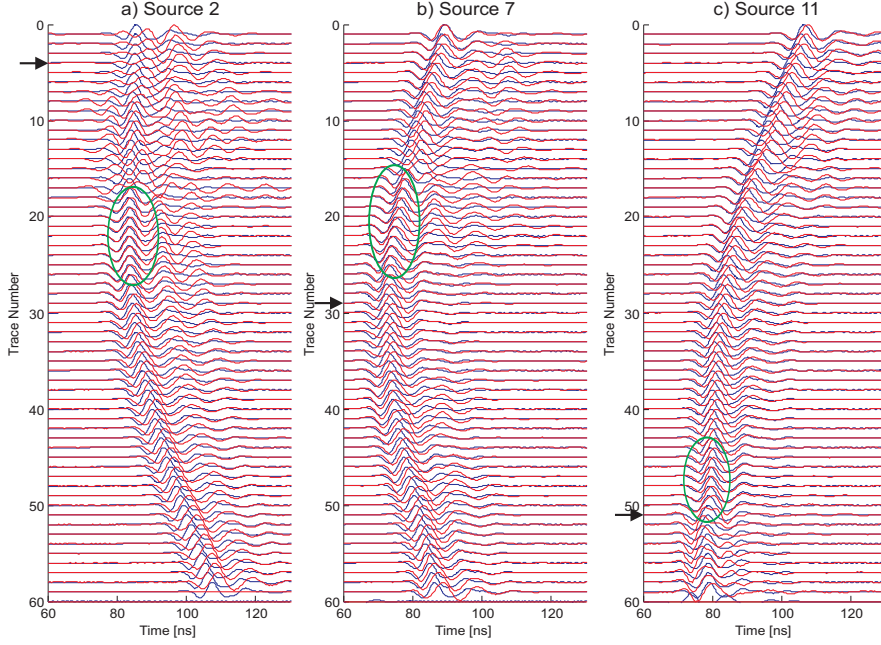
Figure 3.7: Comparison of normalized observed (red) and modeled (blue) traces after the first forward modeling run using the ray-based inversions results for transmitter gathers a) 2, b) 7 and c) 11. The green ellipses indicate the areas of best fit between the traces. The arrows at trace number a) 4, b) 29 and c) 51 indicate transmitters 2, 7 and 11, respectively.

during preprocessing are shown by vertical dotted green lines. Within the band-pass there is a good match of the amplitude spectrum (Fig. 3.8a), whereas the phase spectrum still shows a significant shift. The resulting wavelet, marked as the red graph in Figure 3.5, shows a compensation of the earlier observed time shift between the observed and modeled data in Figures 3.6 and 3.7. This shift probably arises because the first estimation of the wavelet is based on a limited number of averaged direct waves over the entire depth scale and only the general form is obtained. Note, that the amplitude of the corrected wavelet is now also determined, whereas the initial wavelet (blue line in Fig. 3.5) is normalized to the maximum of the first corrected wavelet to allow a comparison of the shape with the corrected wavelet (corrected wavelet amplitude is about 1/25 of the initial wavelet amplitude).

To investigate and refine the phase shift and amplitude, one more correction of the source wavelet is applied using the same steps and parameters (green wavelet in Fig. 3.5).
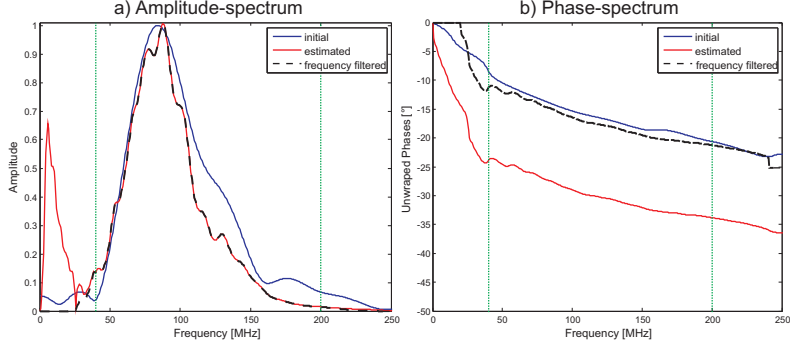
Figure 3.8: a) Amplitude and b) phase spectra of the initial source wavelet (blue), the estimated wavelet (red) and the frequency filtered wavelet (dashed black). A band-pass frequency filter is applied, having corner frequencies indicated by the green dotted lines.

The wavelet did not change much and is found to be stable, suggesting that the shape and the amplitude are properly obtained. Figure 3.9 shows a comparison of the observed and modeled data for the same transmitter positions as in Figure 3.7. Note, that non normalization is applied and the true amplitudes are shown. It is obvious that the data fit improves and that both data sets are more comparable. The observed and modeled traces now have the same first-arrival times and the amplitudes for the traces correspond better when the transmitter and receiver positions are aligned sub-horizontally (see green ellipses). The time shift of 3 ns that was observed after the first forward modeling is absent. However, with increasing angle from the transmitter, the fit to the observed amplitudes becomes progressively worse. Note, that during the source wavelet estimation procedure it is checked that the modeled data based on the starting models, matches the observed data within half the dominate pulse otherwise the inversion will proceed to update in the wrong direction.

3.4   Full-waveform inversion

3.4.1   Permittivity and conductivity results

The full-waveform inversion (Fig. 2.1 Part III) starts by computing a modeled wave field using the ray-based results, shown for the permittivity in Figure 3.10a (iteration 0) using the travel time inversion. Figures 3.10b - d show the permittivity tomograms obtained for iterations 10, 20 and 35, respectively. In the upper two meters the image changes between iteration 0 and 20 and regions with a higher permittivity become visible. Also,
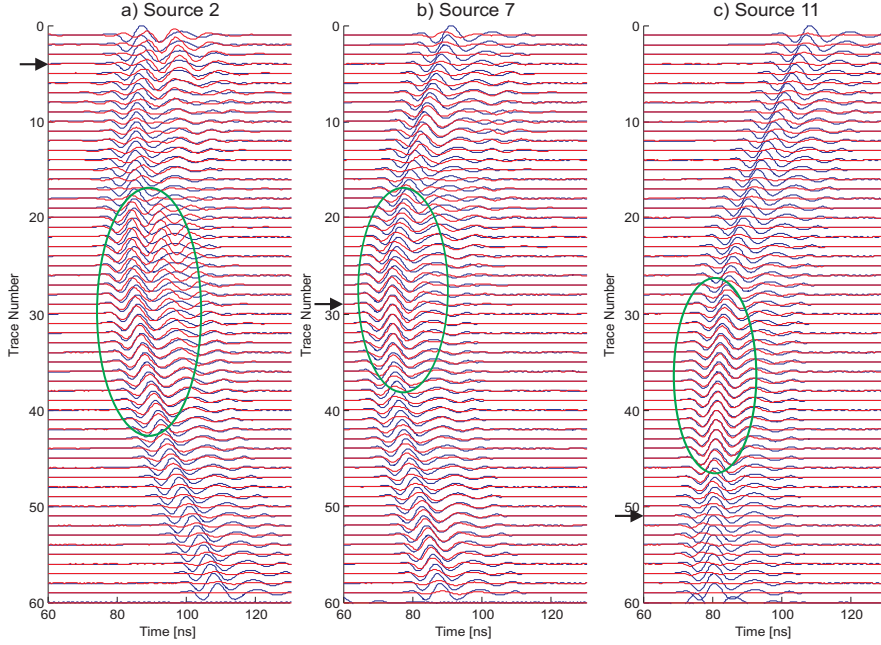
Figure 3.9: Comparison of true amplitude observed (red) and modeled (blue) traces after the second forward modeling run for the measurements of the transmitter positions a) 2, b) 7 and c) 11. The green ellipses indicate where the best fit is between the traces.

over the depth range 5.5 m - 10 m more structures and layering become evident. After iteration 20, the tomograms remain relatively constant until the final solution (iteration 35) in Figure 3.10d. The final permittivity image shows much more details than the travel time inversion result. The aquifer area between depths of 4 m - 5.5 m contains thin layers having very high contrasts. Instead of the more or less homogeneous middle layer obtained from the travel time inversion, the area between 6 m - 7.5 m depth contains two areas of relatively low permittivity. Below this area four intermediate and two lower permittivity zones are resolved.

Figure 3.11a shows the initial conductivity model (logarithmic scale) obtained from the ray-based inversion (iteration 0) using the first-cycle amplitudes. The conductivity tomograms after iterations 10, 20 and 35 of the full-waveform inversion are shown in Figures 3.11b - d, respectively. In contrast to the permittivity tomograms, where small-scale features become visible in the earlier iterations, the conductivity tomograms remain relatively smooth during the first 20 iterations, whereas finer details only occur for the later iterations. The reason is that the permittivity inversion model must first converge to

ensure matching the phases between the modeled and real data. Otherwise, the waveforms are not time-aligned and the amplitudes cannot be effectively optimized. A kinematic shift of more than one quarter of a pulse period precludes a satisfactory dynamic inversion. The final conductivity tomogram shows much more detail than the ray-based model (iteration 0). A very pronounced higher conductivity zone is imaged at a depth below 9.5 m (black dashed line in Fig. 3.11d), indicating the boundary of the underlying lacustrine sediments. In contrast, the ray-based methods were not able to detect this lower boundary (Fig. 3.11a).

Generally, the permittivity and conductivity images of the gravel aquifer show a much higher resolution compared to the ray-based inversion between 5.5 m - 10 depth. Thin horizontal layers are imaged for the upper part between 4 m - 5.5 m depth of the aquifer having strongly alternating permittivities and conductivities which need to be further investigated. Therefore, Figure 3.12 shows the smoothed gradient $\nabla \mathbf{C}_\varepsilon$ and $\nabla \mathbf{C}_\sigma$ (Eq. 2.24) for the final permittivity and conductivity results after 35 iterations, respectively. Between 5 m - 6 m depth in both cases a remaining gradient can be observed, which is a indicator that not all the data are perfectly fitted.
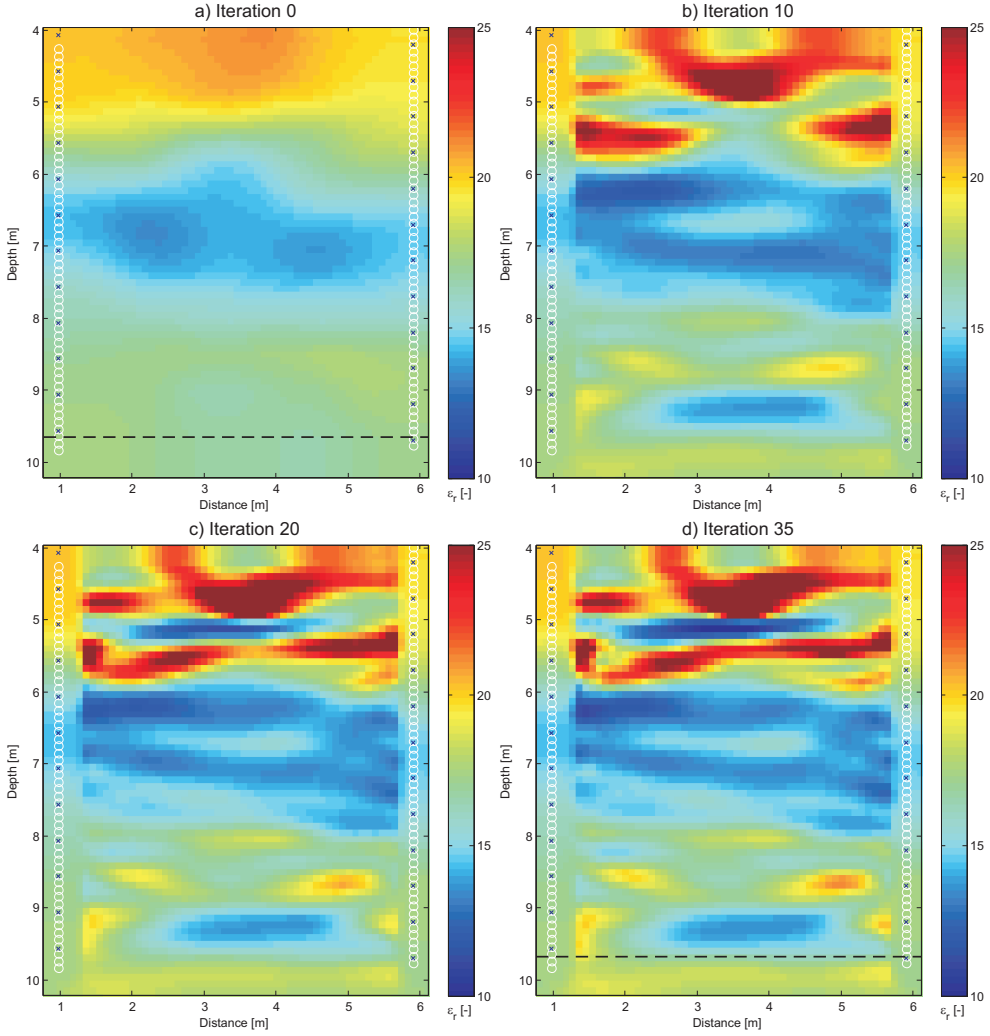
Permittivity Tomograms

Figure 3.10: Relative permittivity tomograms for different iteration steps from a) initial model of the full-waveform inversion obtained from the ray-based inversion, b), c) and d) show the models obtained at iterations 10, 20 and 35, respectively.
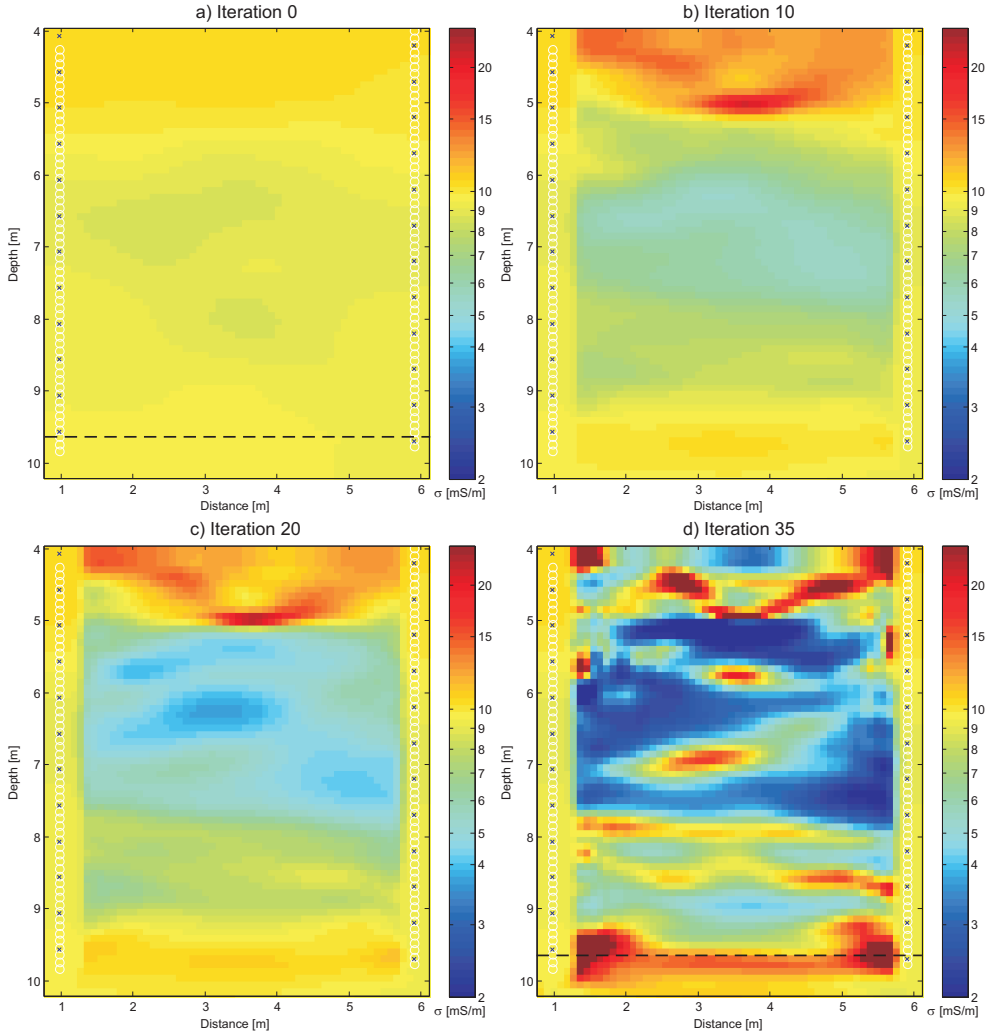
Conductivity Tomograms

Figure 3.11: Conductivity tomograms for different iteration steps from a) initial model of the full-waveform inversion obtained from the ray-based inversion, b), c) and d) show the models obtained at iterations 10, 20 and 35, respectively. Note the logarithmic scale for the conductivity image.
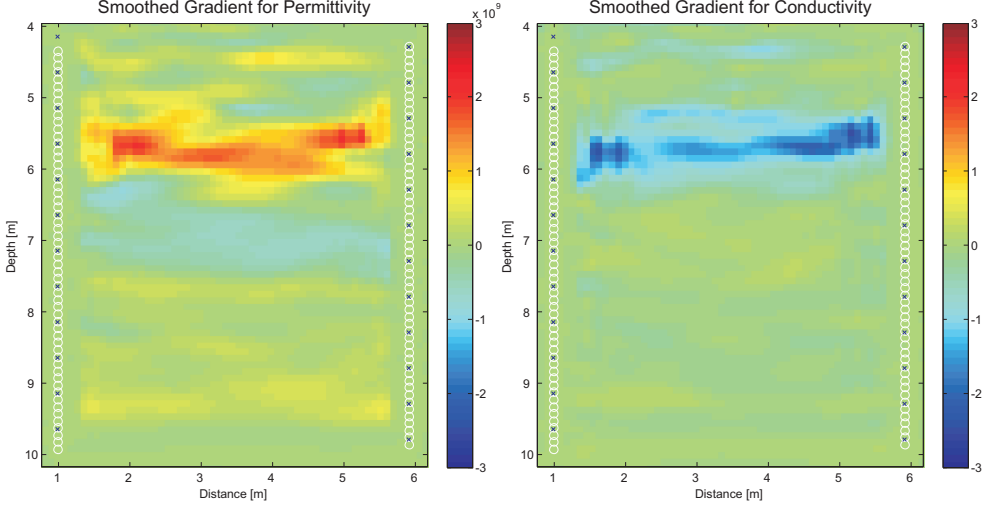
Figure 3.12: Smoothed gradient for a) permittivity and b) conductivity after 35 iterations.

The RMS misfit between observed and predicted traces for all iterations is shown in Figure 3.13. The vertical axis is normalized such that the RMS of the initial model (obtained with the ray-based inversion) is equal to 1.0. The convergence criterion of less than 1% change in the misfit between iterations is achieved after 35 iterations.

3.4.2 Comparison between observed and modeled traces

Figure 3.14 compares the observed traces (red) for transmitter positions 2, 7 and 11 at iteration 35 with the modeled traces (blue) with the true amplitudes. For transmitters 7 and 11 (Figs 3.14b, c), the simulated amplitudes and phases fit the measured data remarkably well. Therefore, we expect that the tomogram details below 6 m depth represent reality rather well. By comparing Figures 3.7, 3.9 and 3.14 it is obvious that the fit between the observed and modeled data becomes significantly better after wavelet estimation and especially after the full-waveform inversion. The green ellipses indicate the areas with the best fit. All these results indicate that the simultaneous full-waveform inversion of both permittivity and conductivity performs well.

The agreement for transmitter 2 (Fig. 3.14a) is less convincing. Note, that transmitter 2 is located in the upper region close to the water table (see arrow in Fig. 3.14a) and was excluded from the source wavelet estimation. On the basis of the poor match of the observed and predicted traces in the upper part of the aquifer (Fig. 3.14a) and also indicated by a remaining permittivity and conductivity gradient $\nabla \mathbf{C}_\varepsilon$ and $\nabla \mathbf{C}_\sigma$, respec-
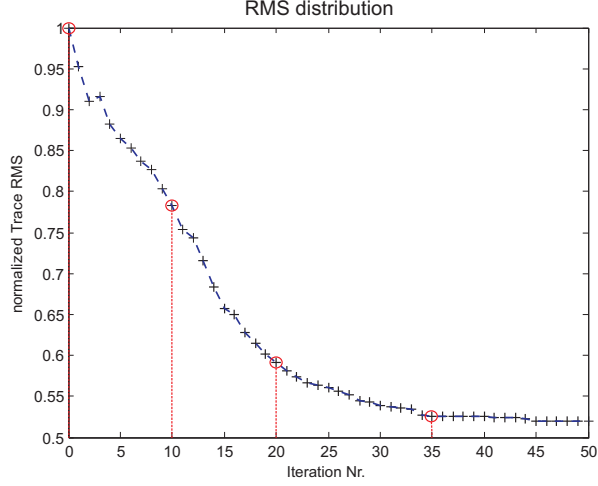
Figure 3.13: RMS values as a function of the iteration number for the ray-based inversion starting model. The RMS is normalized to the ray-based inversion result and after 35 iterations the RMS misfit changes less than 1%. The red circles along the graph indicate the iteration number for which the permittivity and conductivity results are shown in Figures 3.10 and 3.11.

tively (see Fig. 3.12), we expect the full-waveform models to be unreliable between 4 m - 6 m depth. A likely explanation for this is the presence of the groundwater table, which represents a very strong discontinuity in electrical subsurface parameters. The presence of the water table is indicated by the additional prominent refractions and reflections shown in the blue ellipse in Figure 3.14 for transmitter 2 in the upper 5 traces (not present in the modeled data). Instead of discarding the traces containing refracted waves that have traveled through the unsaturated gravel, as is done in the ray-based inversion (see Fig. 3.4c), we included all traces in the full-waveform inversion. The algorithm tried to fit these events without taking into account the presence of the unsaturated zone. This leads to non-linear effects that can cause the inversion to get trapped in local minima. This probably produces anomalous structures (low and high permittivity and conductivity values) in the upper 2 m.
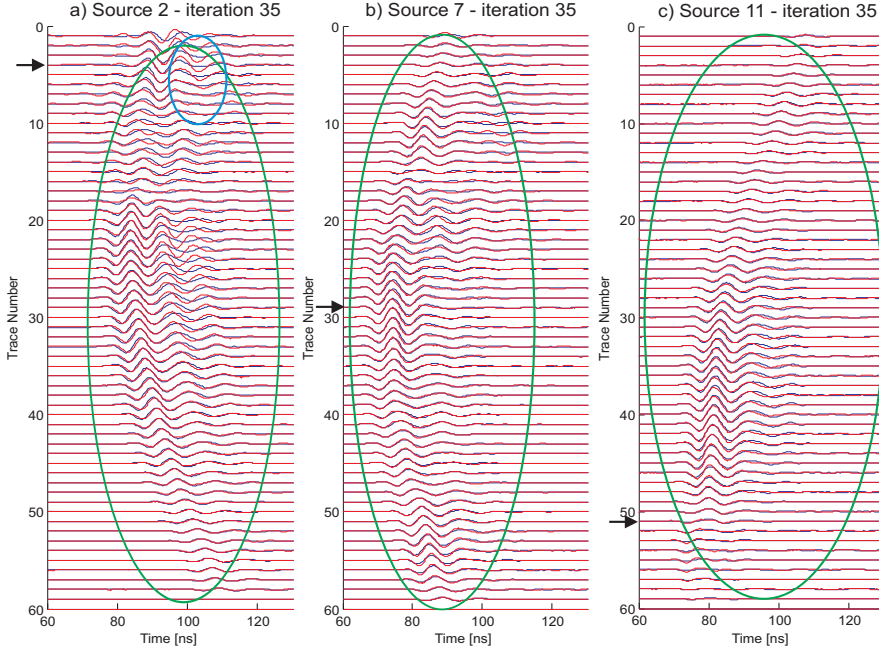
Figure 3.14: Un-normalized true traces after 35 iterations for the measurements of transmitters a) 2, b) 7 and c) 11. A general good agreement of the observed traces (red) and the simulated traces (blue) is visible. The green ellipses indicate where the fit is best between the traces, whereas the blue ellipse shows the reflections from the water table (see text for further discussion).

3.5 Full-waveform inversion using an improved starting model

To solve the issue of the insufficient results between 4 m - 6 m depth, in the second part of this Chapter the starting model will be improved by incorporating as a priori information the unsaturated zone of the aquifer and by updating the starting model close to the water table. Furthermore, data of transmitter and receiver positions close to the water table (partly located in the saturated and in the unsaturated domain) that show significant refractions and reflections will be excluded.

3.5.1 Improved starting model and data update

Until now, we used the ray-based inversion results as a starting model. After we discarded traces containing refracted waves that traveled through the unsaturated gravel (two transmitter and four receiver positions were excluded), we obtained still a low ray-coverage close to the water table. Here, we adapt the ray-based starting model by introducing a homogeneous permittivity layer between 4.2 m - 6 m depth and the water table at 4.2 m in the inversion domain (low permittivity above) shown in Figure 3.15. Forward modeling with a relative permittivity of 17 for this layer show an overlap of the modeled radar waveforms with the observed data to within half the dominant pulse period, which is a necessary condition for convergence (Meles *et al.*, 2011). For conductivity we use a homogeneous starting model of 9.5 mS/m, which represents the mean for the first-cycle amplitude inversion results. The effective source wavelet is again updated using this new starting model and after 5 iterations of the full-waveform inversion. Figure 3.16 shows the comparison with the source wavelet obtained in Chapter 3.3.2. Note the higher amplitude which is caused by the updated conductivity model after 5 iterations of the inversion (conductivity mainly influences the amplitude of the data).
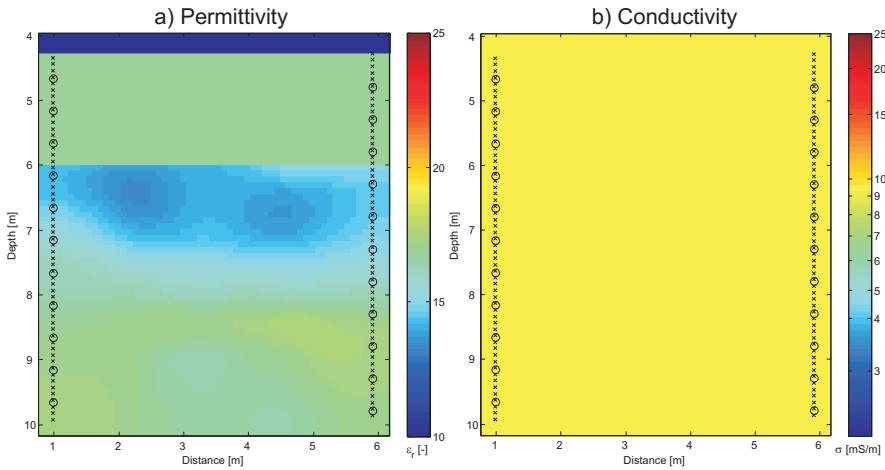

Figure 3.15: Improved starting model for the a) permittivity and b) conductivity. In the permittivity model the vadose zone above 4.2 m depth is included together with a homogeneous layer between 4.2 m - 6 m depth. For the conductivity a homogeneous model is defined with the mean conductivity of the first-cycle amplitude inversion.
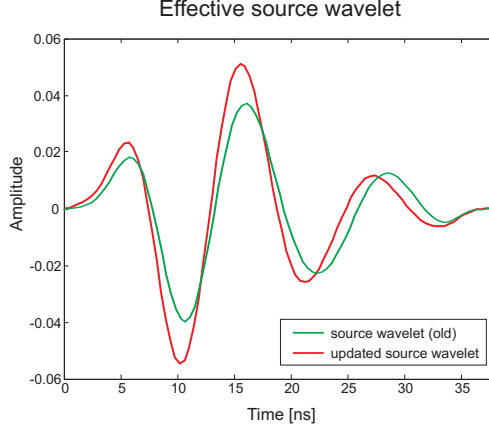
Figure 3.16: Comparison of the effective source wavelet based on the ray-based inversion (green), which is equal to second corrected wavelet in Figure 3.5, and the improved effective source wavelet (red).

3.5.2 Permittivity and conductivity results

Figure 3.17 shows the permittivity and conductivity tomograms after the stopping criterion is reached at 25 iterations. The root-mean square (RMS) error between the observed and modeled data is reduced by 55% to 1.81 from its value for the initial model (ray-based model reduced by 47% to 2.01), thus the inversion converged faster and a further improvement of the RMS is achieved by using the new starting model. Reliable inversion results for the entire inversion domain are indicated by the absence of a remaining gradient for permittivity and conductivity, shown in Figure 3.18. For the area below 5.5 m depth similar results are obtained for the permittivity and conductivity as shown in Figures 3.10d and 3.11d where the ray-based starting models were used. The main difference is the absence of the high permittivity layer above 5 m depth (see Fig. 3.10d). The prominent high permittivity (low-velocity) layer, that is dipping slightly upward from left to right, between the black dashed lines (depth range 5.3 m - 6.1 m), was also indicated in the previous results, but was not considered reliably due to presents of the artefact above and the remaining gradient for this area.

3.5.3 Comparison of the modeled and measured data

In the entire inversion domain a remarkably good fit between the measured and modeled data is obtained. Figure 3.19 compares the measured electric field (radargrams) and the synthetically calculated electric field for the final inversion model, for transmitter T3
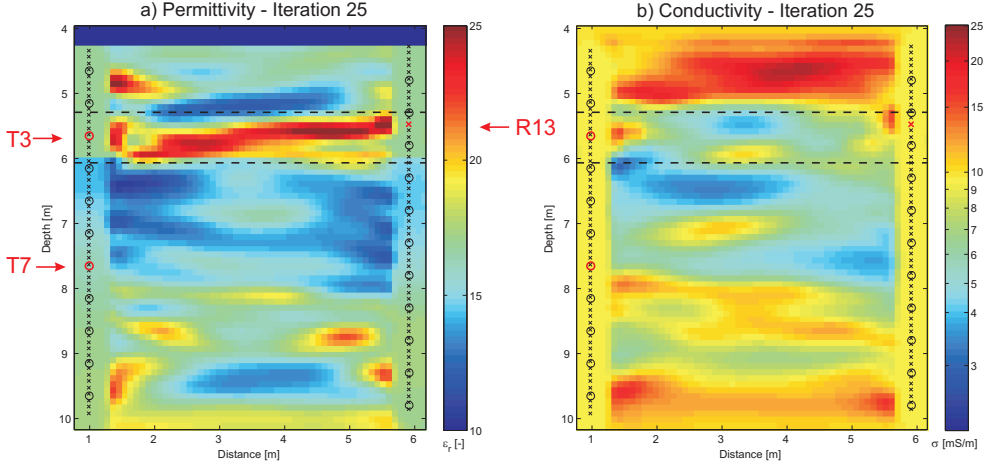
Figure 3.17: a) Permittivity and b) conductivity results of the full-waveform inversion after 25 iterations. Note the logarithmic scale for the conductivity image. Transmitter and receiver positions are indicated by circles and crosses, respectively, along the vertical edges. The black dashed lines indicate the boundaries of the high permittivity/ low-velocity region. Observed and modeled data for the red marked transmitters T3 and T7 are shown in Figure 3.19.

in the high permittivity zone (low velocity), and transmitter T7 below this zone. The circles indicate the position of the transmitters, and the black dashed lines at 5.3 and 6.1 m indicate the upper and lower boundaries of the high permittivity zone (see also Fig. 3.17a). In general, the modeled data are very similar to the measured data in shape and amplitude, which indicates a reliable inversion. The measured and modeled data for transmitter T3 (Figs 3.19a and b) show very similar elongated wave trains and high amplitudes at later arrivals over the depth range of the high permittivity/ low velocity zone. For the transmitter outside the waveguide T7 (see Figs 3.19d and e), the measured and modeled waveforms have similar shape and amplitude at all receiver depths.

Figures 3.19c and f show the trace energy spectra for T3 and T7 (note the logarithmic scale), respectively. In Figure 3.19c the highest amplitudes are observed within the waveguide and shows a maximum at receiver R13, which lies where the waveguide approaches the receiver borehole and the velocity has a minimum (see Fig. 3.17a). In contrast, the receivers located above 5.3 m and below 6.1 m show significantly reduced amplitudes (at least one order of magnitude) and shorter wave trains. The high amplitudes and elongated wave trains are caused by total reflection of the waves emitted by T3 at the upper and lower interfaces of the waveguide. The EM energy is essentially
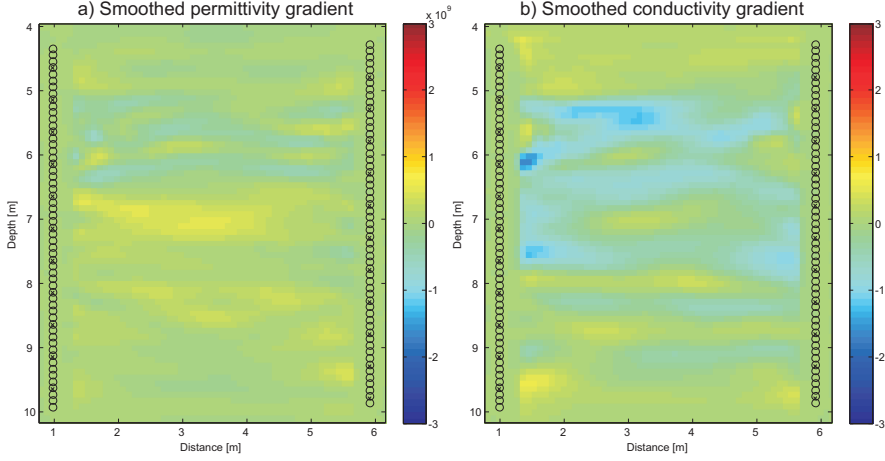
Figure 3.18: Smoothed gradient for a) permittivity and b) conductivity after 25 iterations.

trapped within the waveguide by total internal reflection (beyond the critical angle) at the upper and lower boundaries (van der Kruk *et al.*, 2006). The multiple reflections interfere constructively to produce high amplitude signals with less geometrical spreading than for receivers (and transmitters) outside the waveguide. For the trace energy spectra of transmitter T7 (outside the guide) the energy is equally distributed, except for receiver R13 (inside the guide), where a pronounced reduction in amplitude (Fig. 3.19f), corresponding to the phase change observed in Figures 3.19d and e is visible. The solid, dark green lines in Figures 3.19a and d indicate the picks of the first-arrival times. The light yellow amplitudes to their immediate right indicate the first-cycle amplitudes that were used in the ray-based inversion. These first-cycle amplitudes do not represent the energy content for the entire trace because later parts of the wave train have large amplitudes which are ignored by ray-based methods. In comparison, full-waveform inversion uses all information and resolves the thin waveguide layer that produced the diagnostically large later arrivals.

We also perform forward modeling using the ε_r and σ inversion results of Figure 3.17. Snapshots of the wave field at time t = 64 ns are given in Figures 3.20a and b for transmitters T3 and T7, respectively. Figure 3.20a shows that (1) most of the radiated energy is trapped within the waveguide zone indicated by the black dashed lines; (2) an elongated wave train is present due to multiple internal reflections (see characteristic ray-path in Fig. 3.20a); and (3) only waves with small amplitude can be observed outside the waveguide. Figure 3.20b shows that the wavefronts emanating from transmitter T7 have a more uniform amplitude distribution over almost the entire depth range and the
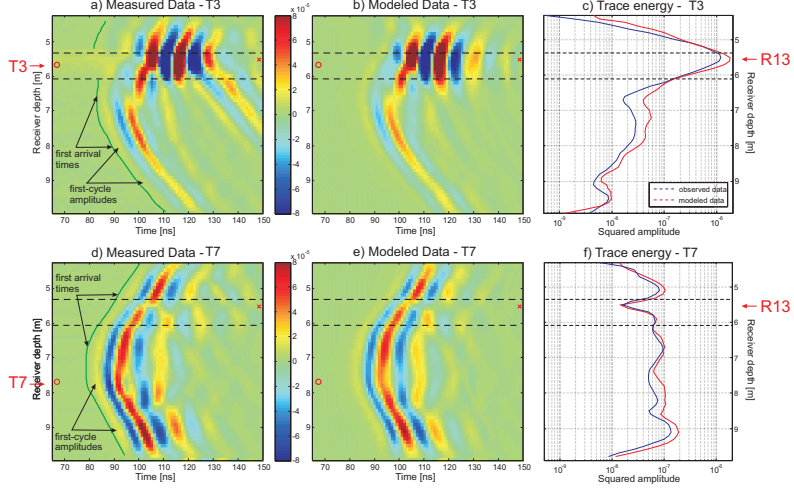
Figure 3.19: a) Measured and b) modeled data of transmitter T3 for all receiver depths and c) corresponding energy plots of the measured and modeled data shown in red and blue, respectively. d) Measured and e) modeled data of transmitter T7, and f) corresponding energy plots. Note, that the same axes are used to enable a quantitative amplitude comparison. The green lines indicate picked travel times for the light yellow, first-arrival amplitudes used in the ray-based inversion.

waveforms is closer to spherical.

Figure 3.20b illustrates that, at a depth of ∼5.5 m (i.e., within the waveguide range), an anomalous decrease in amplitude and a clear change in wave characteristics occurs, which is consistent with the minimum amplitude observed in Figure 3.19f. The waves emitted by transmitter T7 enter the waveguide layer and refract toward the vertical due to the decrease in velocity within the waveguide. Subsequently, they bend away from the vertical when leaving the waveguide at the other side (see characteristic ray-path in Fig. 3.20b). Due to the bending toward the vertical, the waves on opposite sides of the waveguide clearly shift in travel time. Because of interference, a phase change occurs which coincides with the amplitude minimum. This notch, or reduced amplitude, occurs at the depth of receiver R13 (Fig. 3.19f). The modeled data sets show a minimum in receiver amplitude for transmitters close to the waveguide at a depth of approximately 5.8 m, which moves toward 5.3 m for transmitters at greater depths. Consequently, our full-waveform inversion returns sub-wavelength resolution images of aquifer heterogeneities including the low-velocity waveguide. The thin low-velocity layer is caused by high porosity and water rather than high clay content. This layer was confirmed by flow meter and slug tests that detected
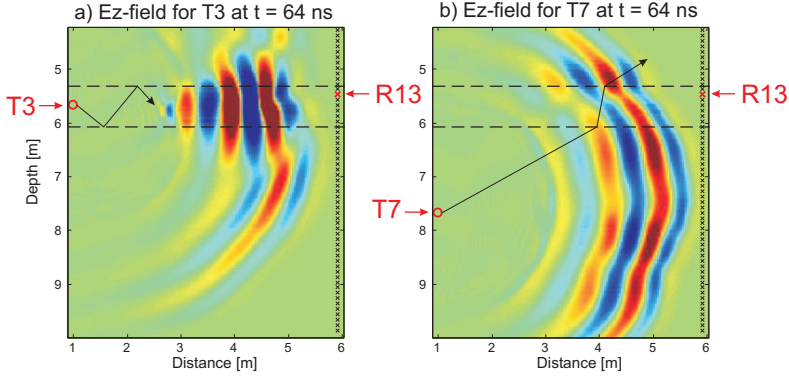
Figure 3.20: Forward modeled snapshots of the electrical field distribution at 64 ns for transmitters a) T3 and b) T7, respectively, using the full-waveform inversion results shown in Figure 3.17. Transmitter positions are indicated by red circles. Inset of a) shows the effective source wavelet determined from the measured data that we used in all the forward modelings.

a high hydraulic conductivity layer between 5.2 and 6.7 m (Diem *et al.* (2010), S. Diem, personal communication, 2011). Moreover, a detailed ERT time lapse study indicated a preferential flow path within the aquifer (Coscia *et al.*, 2012). Although the conductivities within the waveguide layer are low, they cannot be quantitatively interpreted because the 3D to 2D conversion only corrects the amplitude for the first-arrivals and not for the late arrivals, such as the elongated wave trains that indicate the waveguide.

3.6   Conclusions

Full-waveform inversion uses all phase and amplitude information contained in the measured data and is able to image complicated structures within sub-wavelength resolution. Here, the crosshole full-waveform inversion was applied by using an optimized acquisition setup and was able to image high resolution images between two boreholes for the entire saturated domain including the area close to the water table and high contrast layers. Due to the adapted acquisition setup of using less transmitters then receivers, the computational cost of the full-waveform inversion were acceptable and showed still a high resolution. After incorporating the vadose zone in the starting model, the improved inversion results revealed a low-velocity waveguide (high permittivity) between 5 m - 6 m depth. Comparison of measured data with synthetic data modeled using the inversion results as input showed that the shape and amplitude were very similar, including the

elongated wave trains and high amplitudes at late arrivals caused by the waveguide. The good fit and the reduced gradient for the final permittivity and conductivity models indicate reliable inversion results. Low-velocity waveguides may correspond with preferential and more permeable flow paths within an aquifer and we showed that the full-waveform inversion is able to characterize such layers. We observed for transmitter traverses in the waveguide, high-amplitude elongated wave trains would be sensed by receivers straddling the depth range of the waveguide, and have energy one to two orders of magnitude higher than that recorded outside the waveguide. When the transmitter is located above or below the low velocity channel (high permittivity), intermediate amplitudes are measured on most receivers. An additional waveguide indicator is the significantly diminished amplitude detected on receivers located within the waveguide for a transmitter outside. Therefore, high-contrast layers can be observed which cannot be reached by surface GPR measurements. Using lower frequency antennas, these high contrast layers could probably be observed over larger distances. Nevertheless, more research is needed to quantify the uncertainty of the obtained results.

We demonstrated that a good starting model and effective source wavelet are necessary to accurately resolve permittivity and conductivity distributions. Additional constraints on the starting model are usually required for the region close to the water table due to the presence of reflected waves caused by the water table and the high contrast to the overlying unsaturated zone. Our analyses further showed that estimation of the source wavelet is critical and should also be carried out after several iterations of the full-waveform inversion. A possible improvement could be the estimation of an effective source wavelet for different areas, where the medium parameters and the corresponding dielectric coupling are different (Tronicke & Holliger, 2004). To reliably image also data which are highly influenced by the water table and by the high contrast to the unsaturated domain above (in the second part of this Chapter two transmitter positions were excluded), it is necessary to jointly invert the saturated and unsaturated aquifer. Appendix B introduces such a combined full-waveform inversion of the saturated and unsaturated aquifer. Thereby, four effective source wavelets during the full-waveform inversion are necessary. Another factor that might also influence the results in the upper part of the aquifer is the 3D to 2D conversion, which is only valid for far-field conditions. Here, the minimum distance between transmitter and receiver is seven wavelengths and publications (Streich, 2007a) indicate that the far-field assumption may be thus not valid. The use of a 2.5D forward modeling program (e.g., Zhou & Greenhalgh (1998a,b) might solve this problem.

Chapter 4

3-D characterization of high-permeability zones in a gravel aquifer using 2-D crosshole GPR full-waveform inversion and waveguide detection [1]

In this Chapter, we determine the lateral extent of the low-velocity waveguide, which we observed in Chapter 3, using a pseudo-3-D full-waveform inversion of six crosshole GPR cross-sections within a square configuration of four boreholes. For each cross-section, we use a 2-D full-waveform inversion, and the inversion results are visualized in 3-D to characterize the aquifer geometry and the extensions of the low-velocity waveguides. A novel amplitude analysis is introduced to delimit wave-guiding structures by exploring the maxima and minima positions of the trace energy distributions of the measured data, which indicate the existence of wave-guiding structures. Using these positions, we are able to detect fast and efficient continuous waveguides and their boundaries without applying any inversion or detailed processing (necessary for full-waveform inversion). Finally, we compare the full-waveform inversion results with porosities inferred from Neutron-Neutron data and permeability logs based on EM flowmeter data acquired in the same boreholes, and show that the low-velocity waveguides are zones of high porosity and high permeability.

4.1 Thur River test site and 3D acquisition setup

The test site is located in northeastern Switzerland close to the Thur River. Previous studies (Cirpka *et al.*, 2007; Diem *et al.*, 2010; Doetsch *et al.*, 2010a,b; Klotzsche *et al.*, 2010; Coscia *et al.*, 2011, 2012; Klotzsche *et al.*, 2012) indicated an aquifer comprising a 7-m-thick highly permeable glaciofluvial gravel deposit, embedded between overlying alluvial loam, with a thickness of 3 m, and underlying low-permeable lacustrine sediments at a depth 10 m. The test site (Fig. 4.1a) consists of 18 boreholes that were slotted over the thickness of the aquifer. (Coscia *et al.*, 2012) indicated zones of preferential flow in the shallow-to-intermediate zone of the aquifer using ERT time-lapse experiments.
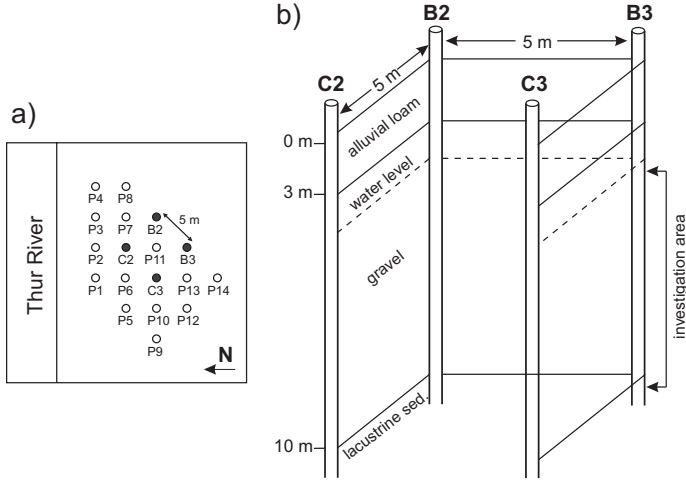

Figure 4.1: a) Overview of the Widen test site with the borehole locations (modified from Coscia *et al.* (2012)). The four black boreholes were used for the full-waveform inversion. (b) Schematic setup of the four boreholes used for the full-waveform inversion within the geological sequence. The aquifer comprised a 7-m-thick gravel layer embedded between alluvial loam in the top 3m and underlying low permeable lacustrine sediments. The groundwater table was at a depth of approximately 4.2 m.

Using four boreholes arranged in a square, (see black circles in Figs 4.1a and b), a zonation based on joint inversion of crosshole GPR, seismics and ERT data was performed revealing that the aquifer can be divided into three main lithological zones, where the middle layer is characterized by a significantly lower porosity Doetsch *et al.* (2010a). In Chapter 3 we studied the acquisition plane between B3 and C3 using GPR full-waveform inversion and imaged a low-velocity waveguide at a depth of 5.3 m - 6.1 m, which was not imaged using other geophysical techniques. Here, we characterized the waveguide zone at

a depth of 5 m - 6 m in 3D, and performed tomographic crosshole experiments using all six possible borehole combinations between the four boreholes followed by a comparison with independent geophysical logging data.

The GPR measurements were acquired using fiber optic cables and RAMAC 250 MHz dipole antennas, except for the cross-section B3 - C2, where 100 MHz antennas were employed due to battery problems. We chose the same depth notation as Doetsch *et al.* (2010a,b), with the zero level being the top of the casing of borehole C2. The same semi-reciprocal setup was applied as in Chapter 3 by using low number of transmitter positions with a spacing of 0.5 m and a dense spatial sampling of the receiver positions with 0.1 m below the groundwater table (approximately at 4.2 m depth). About 9 - 11 transmitters and 55 - 60 receivers were used for both semi-reciprocal measurements in every plane.The specific employed numbers of transmitters (TRN) and receivers (REC) for each plane are shown in Table 4.1.

Table 4.1: Employed number of transmitter and receiver positions for each of the measured GPR planes, whereas the second number indicates the reciprocal measurements.

Borehole plane	B3-C3	C2-C3	B2-C2	B2-B3	B2-C3	B3-C2
Transmitter	11-11	11-11	11-11	11-11	9-10	10-11
Receiver	57-57	56-57	57-58	56-57	54-54	62-53

4.2 Full-waveform inversion results of the Thur River aquifer

Similar to Chapter 3 firstly, the crosshole GPR data were pre-processed by applying a time-zero correction and a band-pass filter to remove the noise outside the source spectrum. Secondly, ray-based inversions using curved rays were applied to obtain starting models. The first-arrival travel-time inversion results based on the data of Doetsch *et al.* (2010a) were used as r starting models, as shown in Figure 4.2. The ray-based tomographic inversion models were a smooth representation of the stratigraphy, and generally three zones were observed with a low r layer embedded between two intermediate ε_r layers. To account for the strong contrast between the unsaturated and saturated zones, which was not resolved by the travel-time inversion, the vadose zone above 4.2 m was attributed a relative permittivity of $\varepsilon_r = 5$, and a homogenous layer was introduced at a depth of 4.2 m - 5.5 m with $\varepsilon_r = 17$. For these values, the first-arrival times of the modeled and

measured data showed an overlap of at least half a wavelength. For σ, we used a homogeneous starting model with 9.5 mS/m, representing the mean of the first-cycle amplitude inversion results.
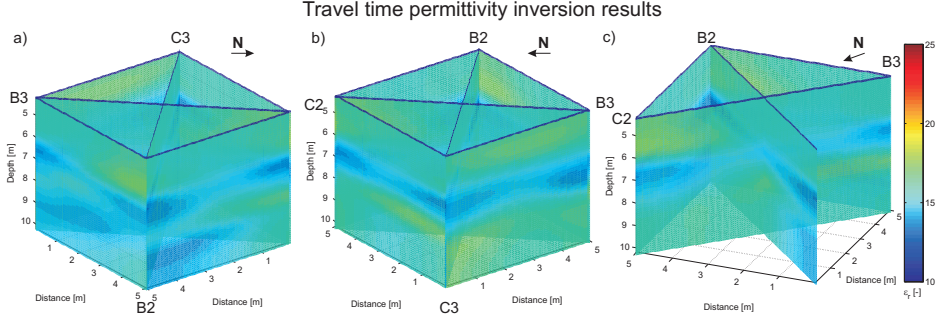

Figure 4.2: Relative permittivity results of the travel time inversion for different viewing angles. See Figure 4.1 for the borehole notation. These results serve as starting models for the full-waveform inversion. The vadose zone is included with a low permittivity $\varepsilon_r = 5$ above 4.2 m depth.

Using the obtained starting models for each of the six cross-sections, an initial source wavelet for each cross-section was estimated by averaging the normalized horizontally traveling pulses from each transmitter. Next, effective wavelets were calculated by applying the deconvolution approach (Figs 4.3a and b). A similar shape and amplitude of the wavelet was observed for all cross-sections where the 250 MHz antennae were used, whereas the diagonal plane C3 - B2 had slightly higher amplitudes. In Figure 4.3c, the normalized amplitude profiles for each of the six cross-sections are plotted. The center frequencies and frequency bandwidth for all cross-sections with the 250 MHz antennas were very similar, as expected from the results presented in Figure 4.3a. Note, that the effective center frequency is significantly lower than the nominal center frequency, due to the fact that the antennas are electrically longer in high-permittivity media and emit lower frequencies than when they are placed in air. Similar wavelets were observed for all angles, which indicates that our numerical approach to model the antennas as infinitesimal dipoles is suitable. In the modeling, the dipole antennas were present at the position of the feed gap of the true antennas. When transmitter-receiver combinations are used with larger angles, differences in the wavelets might occur, and the finite length of the antennas must be included. Antennae with finite length can be implemented in the FDTD code using the approach of (Arcone, 1995), and (Streich & van der Kruk, 2007).

The full-waveform inversion results for ε_r (Fig. 4.4) show higher resolution images than the travel-time inversion results (Fig. 4.2). The high ε_r zone at a depth of 5 m -
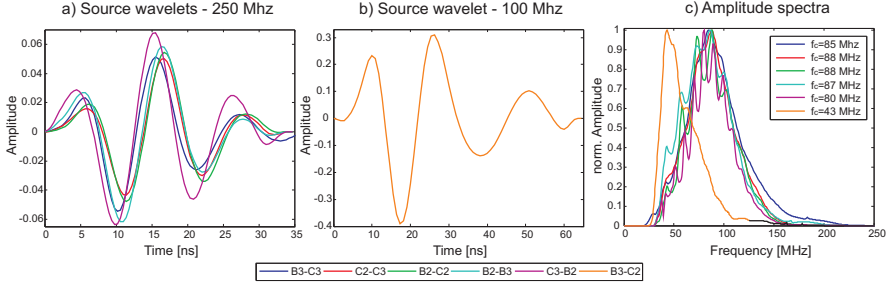
Figure 4.3: a) and b) show the estimated effective source wavelets for the planes where the 250 MHz antenna or the 100 MHz antenna were used, respectively. Each color in this Figure represents a different plane. In c) the corresponding normalized amplitude spectra are shown for the six different source wavelets. Note the similar shape, amplitude and center frequency for the planes measured with the 250 MHz antennas in blue, red, green and cyan.

6 m for plane B3 - C3, which was inferred in Chapter 3, can be identified in all other cross-sections. Another high ε_r layer was observed at a depth of 7.5 m - 9 m, for example, in planes C2 - C3 and C3 - B3. We obtained similar results for all of the 2D tomograms at the borehole locations, and at the intersection of the diagonals. Only the upper parts of the diagonal sections show less similarity at the intersection. The corresponding 3D σ images from the full-waveform inversion show in all tomograms clearly the underlying lacustrine sediments (elevated clay content) indicated by high-conductivity values below a depth of 9.5 m (Fig. 4.5). These inversion results were achieved without a priori information. In contrast, 3D ERT inversion required constraints on the actual boundaries to obtain models in agreement with the geological logs (Coscia *et al.*, 2011). Although late-arrival amplitudes caused by the high r zone are not correctly processed using the 3-D-to-2-D conversion, the intermediate conductivities obtained at a depth of 5 m - 6 m indicate a change in the porosity rather than a change in the clay content as the cause of the increase in ε_r.

For all of the acquisition planes, a good agreement was obtained between the measured and full-waveform modeled data in terms of shape and amplitude of the waveforms, as shown in Figures 4.6a, b and c for plane B3 - C3 (transmitter located in borehole C3). The ray-based modeled data (Fig. 4.6b) show only a good match of the first-arrival times, but the fit for later-arrivals times and amplitudes is less satisfactory. In contrast, the full-waveform inversion data (Fig. 4.6c) show an excellent fit of amplitude and phase, including small nuances in the radargrams, which indicates that the full-waveform inverted model well explains the measured data. Similar to previous experiences with field data
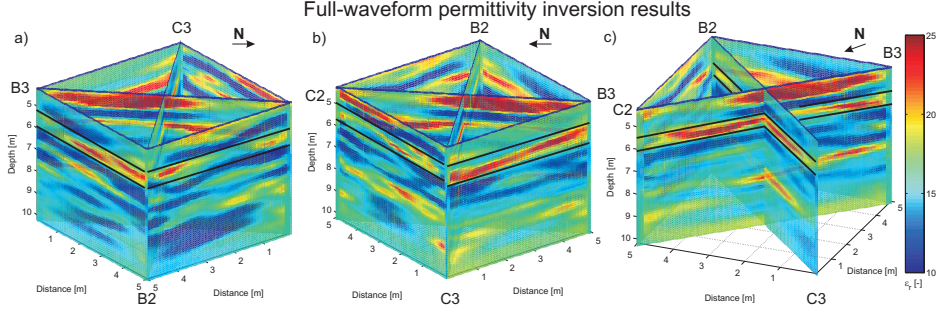
Figure 4.4: Permittivity results of the full-waveform inversion for different viewing angles. See Figure 4.1 for the borehole notation. The vadose zone is included in the inversion above 4.2 m depth. The black lines indicate the high permittivity zone between 5 m - 6 m depth.
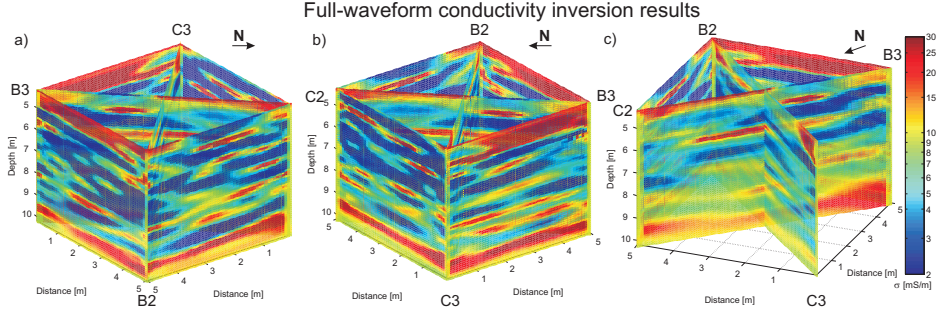

Figure 4.5: Conductivity results of the full-waveform inversion for different viewing angles. See Figure 4.1 for the borehole notation. The vadose zone is included for the inversion above 4.2 m depth.

(Ernst *et al.*, 2007b; Klotzsche *et al.*, 2012; Oberröhrmann *et al.*, 2013), the root-mean-square (RMS) error between the measured and modeled data for each tomogram was reduced by at least 50 % compared to the ray-based inversion starting model.

To test the consistency between inversion results, we calculated correlation coefficients (R) at the intersections of cross-sections at borehole locations and the crossing of the diagonal planes at P11, for permittivity and conductivity (Table 4.2). For the calculation, we used the mean of two inversion cells next to the borehole. A high mean R^2 value of 0.88 was obtained for permittivity, whereas the mean R^2 value for conductivity was lower at 0.25 indicating that the conductivity values are less reliable. To improve the accuracy of conductive values more transmitter and receiver position could be used (Oberröhrmann *et al.*,
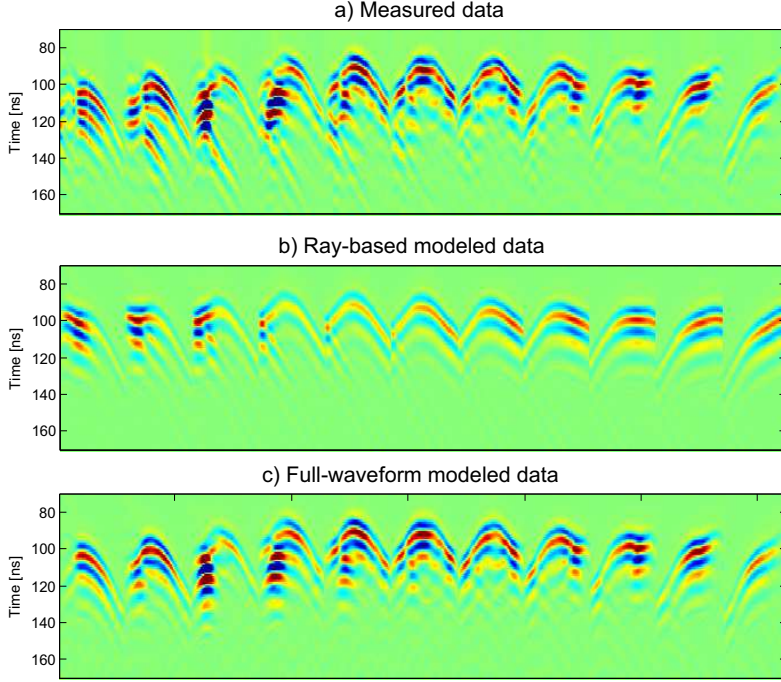
Figure 4.6: a) Measured, b) ray-based modelled and c) full-waveform modelled data for section B3 - C3 (transmitter in C3). The transmitter positions are indicated by T1 until T11, whereas T1 is located close to the water table and T11 at the bottom of the aquifer.

2013) or a combined wavelet and conductivity updating could be implemented (similar to Busch *et al.* (2012)). A total of 23 CPUs (for each transmitter and one master) were needed for the full-waveform inversion and an entire inversion took approximately 30 min using an MPI parallelized code on the JUROPA cluster at Forschungszentrum Jülich. Improved and more consistent conductivity results could possibly be obtained if cross-sections were inverted together, such that the estimated permittivities and conductivities at intersections are enforced as sometimes done in 2D ray-based inversions (Musil *et al.*, 2006; Dafflon *et al.*, 2011b).

4.3   Waveguide detection through amplitude analysis

Similarly to Klotzsche *et al.* (2012) and Strobach *et al.* (2012), we consistently observe for transmitters located within waveguide zones late-arrival and high-amplitude elongated wave trains for receivers straddling the high-contrast layer. An example is transmitter T2

Table 4.2: Correlations coefficient R^2 for the full-waveform inversion permittivity and conductivity results at the boreholes. The mean value of the R^2 for the permittivity and conductivity planes is 0.88 and 0.26, respectively.

Borehole	Planes	$R^2(\varepsilon)$	$R^2(\sigma)$
	B3-C3 B2-C3	0.90	0.17
B3	B3-C3 B3-C2	0.87	0.32
	B2-B3 B3-C2	0.96	0.29
	B3-C3 C3-C2	0.75	0.16
C3	B3-C3 C3-B2	0.87	0.42
	C3-C2 C3-B2	0.85	0.18
	C3-C2 C2-B2	0.81	0.21
C2	C3-C2 B3-C2	0.90	0.19
	C2-B2 B3-C2	0.92	0.53
	C2-B2 B2-B3	0.87	0.29
B2	C2-B2 C3-B2	0.92	0.18
	B2-B3 C3-B2	0.92	0.09
P11	B2-C3 B3-C2	0.84	0.24

of cross-section B3 - C3 (transmitter located in B3), where the wave trains are formed by internal multiple reflections beyond the critical angle, which interfere constructively to produce high-amplitude data and trap the energy within this low-velocity zone (see Fig. 4.7a). The corresponding modeled radargram for T2, as obtained from the final full-waveform inversion models, show a good agreement for the guided wave arrivals (Fig. 4.7a and b). The black lines indicate the position of the waveguide as detected by the full-waveform inversion. Similar high-amplitude elongated wave trains can be observed in the measured and modeled data for transmitter T3 in the cross-section B3 - C3 (not shown).

Elongated wave trains, as observed in measured data of T3 (Fig. 4.7a), show a distinct maximum peak in the trace energy distribution (summation of the squared amplitude) , and the energy for such traces is one to two orders of magnitude higher than the recorded trace outside the waveguide layer, as shown in Figure 4.7c for the trace energy profiles of T2 and T3. For transmitters located outside the waveguide (e.g. Figs 4.7d and e) such as transmitter T7 of cross-section B3 - C3, intermediate amplitudes were observed for most of the receivers. However, receivers positioned within the waveguide showed significantly diminished amplitudes. This behavior is visible in the trace energy profile
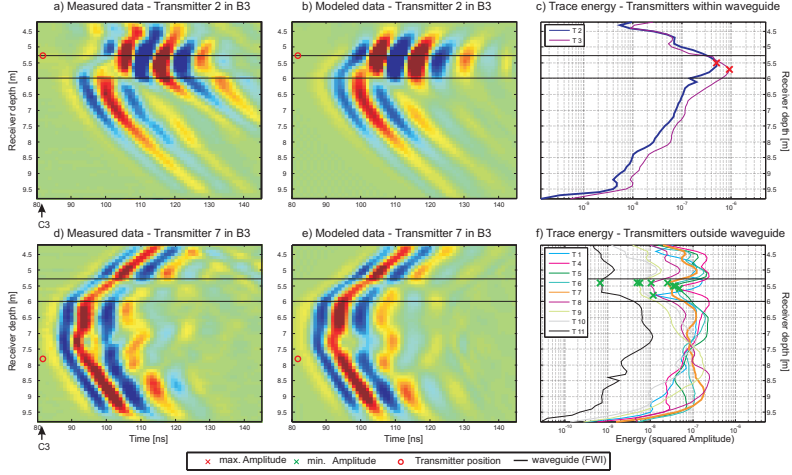
Figure 4.7: a) and b) image plots of the measured and modelled data of transmitter 2 in cross-section B3 - C3, respectively. Transmitter 2 is taken as an example of a transmitter located within the waveguide structure observed in Figure 4.4. The red circle indicates the depth of the transmitter located in B3. c) Corresponding trace energy profiles for all transmitters of the measured data located in the waveguide. The thick blue line indicates the profile corresponding to the image plot in (a). The red crosses indicate the position of the energy maximum. d) and e) image plots of the measured and modelled data of transmitter 7, respectively. Transmitter 7 is taken as an example of a transmitter located outside the waveguide structure. f) Corresponding trace energy profiles for all transmitters of the measured data located outside the waveguide. The thick orange graph indicates the profile corresponding to the image plot in d). The green crosses indicate the position of the energy minimum within the waveguide.

of transmitter T7 (Fig. 4.7f), exhibiting a clear minimum at a depth of 5.4 m around the previously found maxima positions (minima positions should be located close to the maxima positions). Similar behavior was also observed in all other radargrams where transmitters were located outside the low-velocity waveguide (Fig. 4.7f). A possible explanation could be destructive interferences of the electromagnetic head waves from above and below the waveguide, which cause a minimum in the trace energy.

We also located high-amplitude elongated wave trains and diminished amplitudes for the other transmitter-receiver combinations, but concentrated on the dominant features linked to the high-permittivity zone at a depth of 5 m - 6 m, which is present in all planes. Such clear maxima and minima positions of the trace energies as shown in Figure 4.7 were not always observed. For example, for the cross-section C3 - C2 and the transmitters
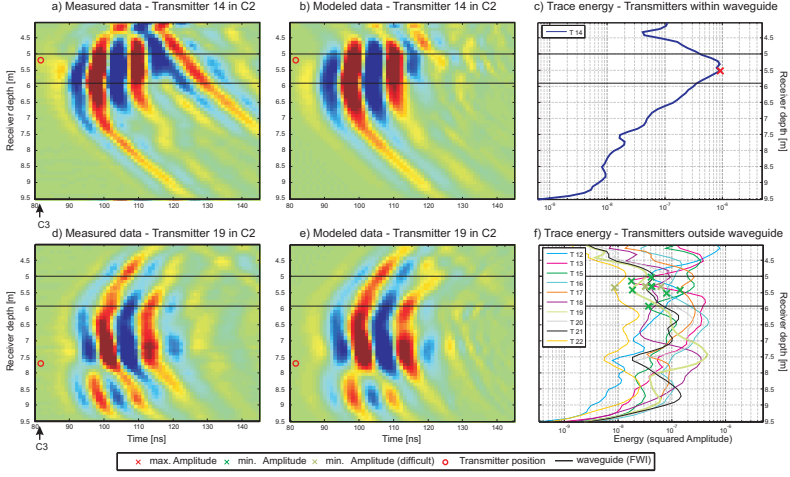
Figure 4.8: a) and b) image plots of the measured and modelled data of transmitter 14 of cross-section C3 - C2, respectively. Transmitter 14 is taken as an example of a transmitter located within the waveguide structure observed in Figure 4.4. The red circle indicates the depth of the transmitter located in C3. c) Corresponding trace energy profiles for all transmitters of the measured data located in the waveguide. The red crosses indicate the position of the energy maximum. d) and e) image plots of the measured and modelled data of transmitter 19, respectively. Transmitter 19 is taken as an example of a transmitter located outside the waveguide structure. f) Corresponding trace energy profiles for all transmitters of the measured data located outside the waveguide. The thick light green line indicates the profile corresponding to the image plot in d). The green crosses indicated the position of the energy minimum within the waveguide.

located in C2, only one transmitter showed late-arrival elongated wave train events and the corresponding distinct maximum in the trace energy (see transmitter T14 in Figs 4.8a - c). Identifying the minima positions for the rest of the transmitters around the maximum position was also more challenging (as shown in Figures 4.8d - f). The less distinct minima positions were probably caused by the lateral heterogeneity within the high-permittivity structure (see also Fig. 4.4b). Further, clear maximum amplitudes were observed for transmitters at a depth between 7 m and 8 m because of the high-permittivity range at these depths (see also Fig. 4.4b).

In the next step, the identified maxima and minima positions of the energy profiles of section B3 - C2 are plotted against receiver depth and compared with the full-waveform inversion results close to borehole C3 (Figs 4.9a and b). It appears that the minima

position for increasing depth converges with the upper waveguide boundary close to the borehole. Due to the restricted distance to the water table for the transmitter positions above the waveguide layer in the saturated aquifer, the minima indicating the lower waveguide boundary were not as definite here. For the second example of cross-section C3 - C2, shown in Figures 4.9c and d, the identification of the boundaries using the measured data was less straightforward, which was probably caused by the heterogeneity of the high-permittivity zone of the plane close to the borehole .
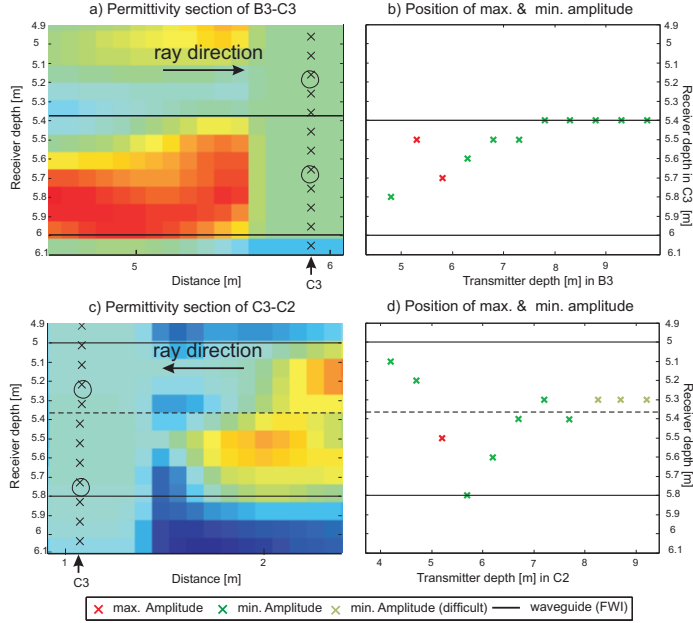

Figure 4.9: a) Permittivity section of the waveguide in cross-section B3 - C3 close to the borehole C3 (see Fig. 4.4). The black lines indicate the waveguide boundaries observed from the full-waveform inversion close to the corresponding borehole. The circles and crosses indicate the transmitter and receiver positions. For comparison, the maximum and minimum positions obtained in Figures 4.7c) and f) are plotted in b) along the receiver depth, where the red and green crosses indicate the chosen maxima and minima position of the trace energy. c) Permittivity section of the waveguide in plane C3 - C2 close to the borehole C3 (see Fig. 4.4). For comparison, the maximum and minimum positions obtained in Figures 4.8c) and f) are plotted in d) along the receiver depth.

For the depth range between 7.5 m and 9 m, additional distinct elongated wave trains (e.g. for plane C3 - C2 in Fig. 4.8d) and corresponding minima positions were found,

pertaining to high-permittivity structures present in the tomograms of C3 - C2, C3 - B2 and B3 - C3 (see Fig. 4.4). Generally, a similar analysis could be carried out; however, choosing maxima and minima positions was more challenging for these zones, and they were not present in all cross-sections. Hence, the accuracy of boundary determination is influenced by the homogeneity of the waveguide.

We applied our approach of detecting maxima and minima positions to the datasets of all six cross-sections for the distinct waveguide at a depth of 5 m - 6 m (Fig. 4.10). In some cases, it was more problematic to define a clear boundary from the minima trace energy picks (indicated with light green crosses). For example, for the transmitter located in C2 (Fig. 4.10b), it appears that two upper boundaries are possible to identify (indicated by dashed lines). The accuracy also decreases for the diagonals (see Figs 4.10e and f, right columns), and picking is more challenging, especially in the case of discontinuous layering of wave-guiding structures. The spatial transmitter position sampling of 0.5 m enabled a detailed detection of the waveguide effects. A sparser spatial sampling of transmitter and receiver would probably have reduced the ability to detect and identify the waveguide structures. The general view that permittivity dominates the travel-time and that conductivity dominates the amplitude of the signal must be revised, because the amplitudes are strongly influenced by the permittivity contrast in the presence of a waveguide.
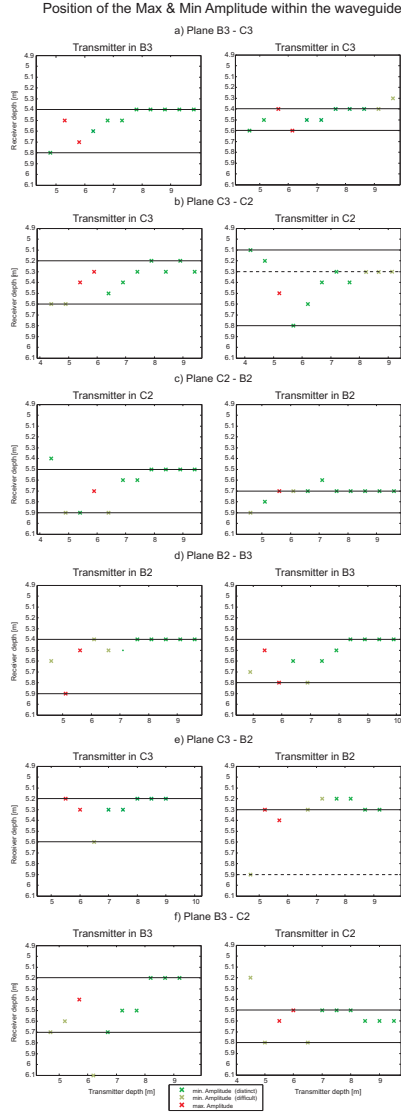
Figure 4.10: Position of the energy distribution maxima and minima for all cross-sections along the receiver depth. The dark green crosses indicate distinct minima position, whereas the light green crosses indicate difficult minima positions. The black lines indicate the estimated upper and lower boundaries of the waveguides obtained by the amplitude analysis using the maxima and minima positions of the trace energy profiles close to the corresponding borehole.

65

4.4 Petrophysical interpretation and comparison with logging data

The permittivity is influenced mainly by the pore structure and the porosity of the gravel, which contains particle sizes between 0.2 mm - 60 mm (Füchtbauer, 1988; Diem *et al.*, 2010) and also a small fraction of fines. Permittivity values for saturated gravel are reported to lie between 20 - 30 (Daniels *et al.*, 2005). The conductivity is determined by porosity and pore structure, salinity and surface conductivity at the grain/solution interface. Moreover, if clay is present in the gravel, conductivities will increase with an increasing amount of clay. Clay particles contribute to the exchange of cations to the electrolyte, which increases the conductivity of the formation (Waxman, 1968; Worthington, 1993).

We transformed the permittivity tomograms of each plane into porosities to characterize the aquifer and evaluate the waveform inversion results. We compared these porosities with Neutron-Neutron porosity and hydraulic permeability logs (Tchang, 2012; Lochbühler *et al.*, 2013). For the transformation of the permittivity, we followed the same approach as (Pride, 1994) and (Doetsch *et al.*, 2010a) using

$$\varepsilon = \frac{1}{F} \cdot [\varepsilon_W + (F - 1) \cdot \varepsilon_S] = \frac{\varepsilon_W}{F} + \varepsilon_S - \frac{\varepsilon_S}{F} \tag{4.1}$$

$$F = \Phi^{-m} \tag{4.2}$$

$$\Phi = \sqrt[m]{\frac{\varepsilon - \varepsilon_S}{\varepsilon_W - \varepsilon_S}} \tag{4.3}$$

where F is the formation factor and Φ the porosity. Here, we used $\varepsilon_W = 84$ as the relative permittivity of water (at 10 °C), $\varepsilon_S = 8$ as the relative permittivity of the solid matrix, and the cementation factor was $m = 1.4$. A positive correlation exists between permittivity and converted porosity (compare Figures 4.4 and 4.11).

All waveguide boundaries identified using the amplitude analysis (see Fig. 4.10 and dark green boxes in Fig. 4.11) were confirmed, and in most cases, the boundaries obtained from the full-waveform inversion agreed well with the boundaries obtained by the energy analysis. The correspondence between the diagonal planes was less clear due to the increased distance and the reduced resolution caused by lower angular coverage and increased data errors. When the waveguide was discontinuously layered, the amplitude analysis approach was less accurate (see Figs 4.9c and d), whereas these heterogeneous structures were also resolved by the full-waveform inversion. In addition to the dominant waveguides between 5 m - 6 m depth (dark green boxes in Fig. 4.11), we also indicate

thinner waveguides present between 7 m - 8 m depth that could be identified using at least one maxima and five minima (light green boxes in Fig. 4.11).

The permeability logs, normalized to the maximum of each log, were obtained using electromagnetic (EM) flowmeter data, in which the difference of the vertical flow in the boreholes was determined by subtracting the ambient flow from a flow measurement during a stable injection (see Tchang (2012)) for details). Within the hydraulic permeability logs, we observed a zone with higher permeability at a depth of 5 m - 6 m, and an intermediate zone at a depth of 7.5 m - 9 m. These zones were also found to have higher values in the porosity images obtained from the waveform inversion. Generally, for all the cross-sections, we obtained a good fit between the permeability logs and the high-porosity zones for the permittivity models of all planes. Furthermore, in the porosity images and in the permeability logs, we observed a decrease in the thickness of the high-porosity zone at 5 m - 6 m towards the Thur River. This change in thickness is indicated by the tomogram C2 - B2 (approximate thickness 0.3 m - 0.4 m), which was located close to the Thur River in comparison to the tomogram B3-C3 (approximate thickness 0.6 m), which was furthest away from the river.

For the diagonal planes, we performed a direct comparison at the intersection of the C3 - B2 and B3 - C2 sections, where Neutron-Neutron porosities and Natural Gamma data were acquired in borehole P11 (see Fig. 4.1 for the location). Neutron-Neutron data indicate water content (and thus porosity), whereas Natural Gamma data indicate the presence of clay. Details of the calculations were given in (Klotzsche *et al.*, 2010). For each depth in the C3 - B2 and B3 - C2 planes, we computed the mean of three cells (each 9 cm) of the porosity models (see legend for corresponding color) and compared these means with the measured porosity logs (black graph) in Fig. 4.11f. Similar the Natural Gamma logs are compared wih the conductivity means in Figure 4.11g. First of all, the porosity results of the full-waveform inversion between depths of 5 m and 10 m were overall very similar, whereas some differences occurred in the upper meter. A comparison of the full-waveform porosities with the Neutron-Neutron porosity logs showed that they agreed well at a depth of 6 m - 9.5 m. For the upper meter, the measured porosity was between the porosities obtained from the two permittivity tomograms. The dashed black line in Figure 4.11g indicates the high conductivity zone of the tomographic planes at the base of the aquifer below 9.6 m depth, which indicates the boundary of the lacustrine sediment. These results fit very well with the Natural Gamma log of P11, which clearly indicate the presence of a high clay content layer below 9.6 m.
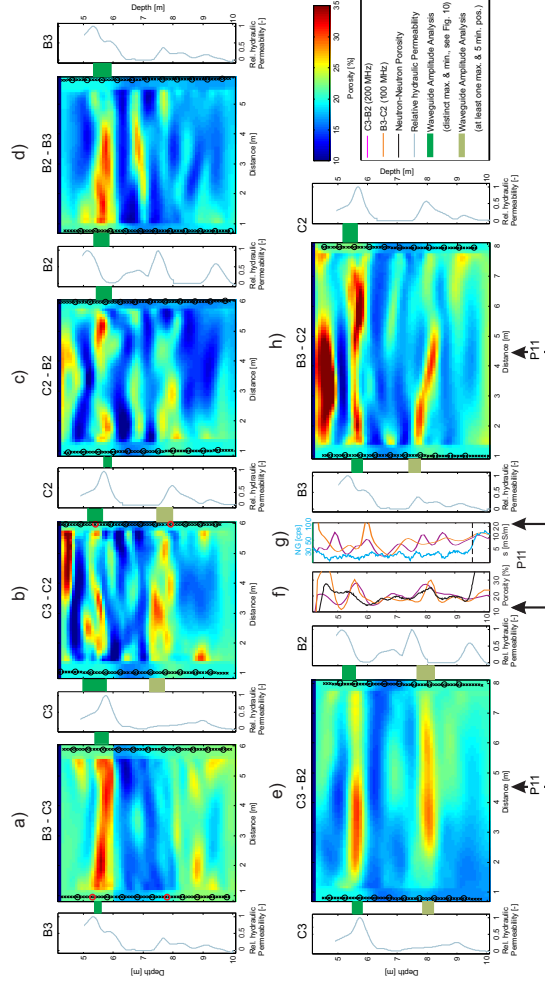
Figure 4.11: Converted porosities from the full-waveform inversion (images) in comparison to relative hydraulic permeabilities measured directly in the boreholes (graphs). Transmitter and receiver positions are indicated by circles and crosses, respectively. The transmitters coloured in red are used in Figures 4.7 and 4.8. f) Neutron-Neutron porosities and g) Natural Gamma log of P11 are plotted with the corresponding response from the full-waveform inversion porosities and conductivity, respectively. The green box between the full-waveform inversion porosities and the permeability log indicate the thicknesses of the wave-guiding structures estimated using the amplitude analysis (see Fig. 4.10).

To evaluate the full-waveform porosities, we calculated the correlation coefficient (R^2), the mean absolute error (MAE), and the root mean square (RMS) error between the Neutron-Neutron porosities of P11 and the porosity graphs of the diagonal porosity planes(Fig. 4.11f) for the depth range of 6 m to 9.5 m. For plane C3 - B2, a higher correlation and smaller misfit with the porosity of P11 was obtained compared to the plane B3 - C2 (Table 4.3). A possible explanation could be the difference in antenna frequency used for the GPR measurements. The lower frequency antenna used for the B3-C3 section results in larger wavelength and lower resolution.

Table 4.3: Correlation coefficients (R^2), mean absolute errors (E), and root mean square (RMS) errors between the porosities obtained from the full-waveform inversion for the diagonal planes and the Neutron-Neutron porosities of P11 at a depth of 6 m - 9.5 m.

	R^2	E [%]	RMS [%]
C3-B2	0.82	1.56	1.87
B3-C2	0.57	1.69	2.15

4.5 Conclusions

We performed a 3D characterization of a gravel aquifer using 2D full-waveform inversion of six cross-sections in a set of four boreholes arranged in a square configuration. The independent decimeter-resolution full-waveform inverted cross-sections revealed good consistency in terms of permittivity at their intersection. In all conductivity images, the underlying lacustrine sediments were clearly observed without relying on any a priori information. Natural Gamma logging data also indicates the presence of this layer boundary at the same depth. However the consistency of the conductivity results is less satisfactory. A good fit was achieved for all tomograms between the measured and full-waveform modeled data in shape and amplitude, including the high-amplitude and late-time arrival events, which indicates reliability of the results. All models showed a high-permittivity layer at a depth of 5 m - 6 m, and a second less extended layer with high-permittivity layer at a depth of 7.5 m - 9 m. These high-permittivity zones acted as low-velocity waveguides for electromagnetic waves.

For transmitters located in the wave-guiding layer, high-amplitude and late-arrival elongated wave trains were present at receivers straddling the waveguide zone. In contrast, for transmitter positions outside the waveguide layer, diminished amplitudes were observed for receivers located within the waveguide. With increasing distance of the

transmitter above and below the waveguide, these minima positions corresponded well with the lower and upper boundary of the full-waveform inverted continuous waveguides, respectively. This novel amplitude analysis was applied to the other measured crosshole data sets, and the obtained waveguide boundaries were confirmed by the full-waveform inversion results. For discontinuous waveguides, the results obtained were less clear. More research with synthetic studies is necessary to explore the potential and limitations of the amplitude analysis in more detail in the case of discontinuous, heterogeneous and dipping waveguides. Nevertheless, this new method is able to provide fast and efficient information about the position and dimension of waveguides without applying any inversion or advanced processing of the data. The full-waveform inversion can provide high resolution images between the boreholes using several processing steps (e.g. starting models, source wavelet estimation) and more computational costs.

The obtained full-waveform inversion results were compared with porosity estimates from Neutron-Neutron and hydraulic permeability logs. While the logging data provide detailed information close to the wells, the full-waveform inversion returns a high-resolution porosity distribution between the boreholes. The peaks of the permeability and porosity logs agreed well with the high-permittivity waveguide layers of the full-waveform inversion at a depth of 5 m - 6 m and 7.5 m - 9 m, and the consistency of the results obtained and the data fit for all the cross-sections showed that full-waveform inversion returns reliable images with the highest resolution currently possible at these scales. The full-waveform inversion and the novel amplitude analysis can be applied as a minimally invasive method to characterize sub-wavelength structures for a wide range of applications, and it can improve our ability to image important small-scale structures in the critical zone.

More research is necessary to quantify the uncertainties of the waveform inversion models using different starting models, and synthetic modeling is required to understand the phenomena that cause the presence of a minimum in the trace energy. Further developments in full-waveform inversion should concentrate on the extension of the forward model to 3D, and a combined 2D inversion of more than one cross-section to get more consistent conductivity models at the borehole locations.

Chapter 5

Detection and identification of waveguides with limited lateral extension: synthetic and experimental data [1]

Since the observed complicated wave phenomena caused by a low-velocuty waveguide as shown in Chapter 4, are not well understood, we perform here a detailed synthetic study to improve our understanding of the observed wave phenomena. The investigation of laterally limited and discontinuous waveguides enabled the extension of the amplitude analysis such that now heterogeneous waveguides with limited lateral extend can also be identified and characterized. By varying the thickness, the extension, the orientation, and the model parameters (ε_r and σ) of defined low-velocity waveguides present between two boreholes, the potential and limitations of the extended amplitude analysis method are investigated. The extended amplitude analysis is applied to an experimental crosshole GPR data acquired at the Boise Hydrogeophysical Research Site (BHRS) that contains two heterogeneous low-velocity waveguides with limited lateral extend. To prove the obtained boundaries of the wave-guiding structures observed in the measured data, we perform full-waveform inversion, which enables us to estimate the structures with decimeter scale resolution. The converted full-waveform porosities are compared with Neutron-Neutron logging data to evaluate the reliability of the amplitude analysis and full-waveform inversion results.

5.1 Synthetic models of continuous and discontinuous low-velocity waveguides with limited lateral extend

For the synthetic study, we use high relative permittivity low-velocity waveguide layers with $\varepsilon_r = 26$ present within a background medium with relative permittivity of $\varepsilon_r = 12$, similar to previously inverted experimental data (see Chapter 3 and 4). The conductivity is assumed to be homogeneous with $\sigma = 8.5$ mS/m in the entire domain. For all the synthetic models we use a reciprocal measurement setup with 21 transmitter and 81 receiver positions with a vertical spacing of 1 m and 0.25 m, respectively. In the following, we choose as notation convention the acquisition plane measured from left to right and from right to left as LR and RL plane, respectively. The transmitters are numbered for the left and the right borehole from top to bottom with L1 - L21 and R1 - R21 starting at 1 m depth until 21 m depth. We calculated for these models, a critical angle θ_c

$$\theta_c = \sin^{-1}\left(\sqrt{\frac{\varepsilon_2}{\varepsilon_1}}\right) \tag{5.1}$$

above which total internal reflection occurs of $\theta_{C1} = 42.8°$. Here ε_1 and ε_2 are the relative permittivities of the waveguide and the surrounding medium, respectively. The synthetic models are calculated using a 2D FDTD algorithm to obtain corresponding synthetic radar data.

First we applied a synthetic model that contains both a continuous and a discontinuous waveguide with limited lateral extent (Fig. 5.1a). For the L10 and R10 transmitters, which are located in the continuous waveguide layer, clearly elongated wave trains and high amplitude late arrivals in the synthetic data are detected over the depth range of the low-velocity waveguide which are causing the peak maxima in the trace energy profiles. The symmetry in the observations indicates a continuous waveguide layer. Also for L9 and R9, indicators for elongated wave trains are visible showing smaller amplitudes than L10 and R10. In contrast, the data for the discontinuous waveguide layer show a clear asymmetry: R12 again indicates elongated wave trains with increased amplitudes for the discontinuous layer, whereas the data for L12 shows a spreading of higher amplitudes at later arrivals. These amplitudes are smaller than for the continuous waveguide.

To investigate the high amplitude spreading over many receivers for the L12 transmitter, we plot snapshots at 64 ns, 102 ns and 127 ns of the vertical electrical wave field (Ez) for transmitter L12 in Figures 5.2a, b and c, respectively. In earlier times (Fig. 5.2a) most of the energy is trapped within the waveguide around 12 m depth forming an elongated wave train caused by internal multiple reflections beyond the critical angle of $\theta_{C1} = 42.8°$.
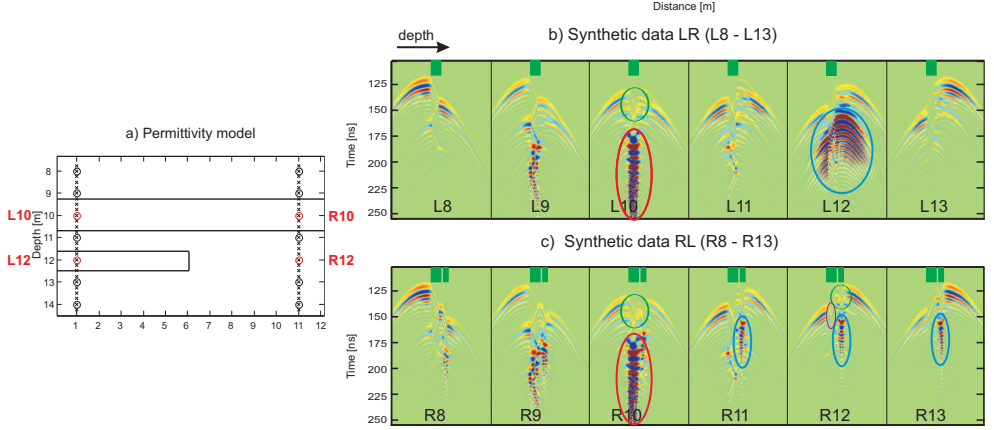
Figure 5.1: a) Permittivity model used for generating synthetic data. The two layers are indicating waveguides with a higher permittivity value as the surrounding medium. b) Synthetic data for transmitters L8 - L13, whereas L10 and L12 are located within the waveguides. c) Synthetic data for transmitter R8 - R13, whereas R10 is located within a waveguide layer. The green boxes are indicating the position of the waveguides. L10 and R10 data are showing clearly elongated wave trains with high amplitudes at later arrivals and a reduced velocity indicated by the red circles, whereas the events caused by the second discontinuous waveguide (reduced lateral extension) are marked by blue circles.

In addition, a delayed travel time can be observed caused by the reduced velocity (see blue circle). At 102 ns Figure 5.2b we see that the wave field starts to leave the waveguide and the energy, which was trapped at earlier times, is released and the bundled energy is then spreading in the homogeneous half space with higher amplitudes compared to the other wave fronts. This behavior continues also at 127 ns where the wave field is more spread out (see blue circle) and finally measured by the receivers on the right side. In contrast, the emitted wave of R12 travels more equally distributed in the domain until 64 ns (Fig. 5.2d). As soon as the wave enters the discontinuous waveguide (shown in Figs 5.2e and f), the energy is trapped within this zone and also causes an elongated wave train with a delayed travel time (blue circles), but with a smaller amplitude than for the continuous waveguide. When the waveguide would continue to the other borehole such as the waveguide at a depth of 10 m, this delayed travel time can be clearly observed, as shown in Figure 5.1 for L10 and R10. If we analyze the wave behavior in the continuous waveguide at 10 m depth, we observe that the wave field transmitted into the waveguide from below is refracted towards the vertical and refracted away from the vertical after being transmitted out of the waveguide. Note that the angle of incidence is below the
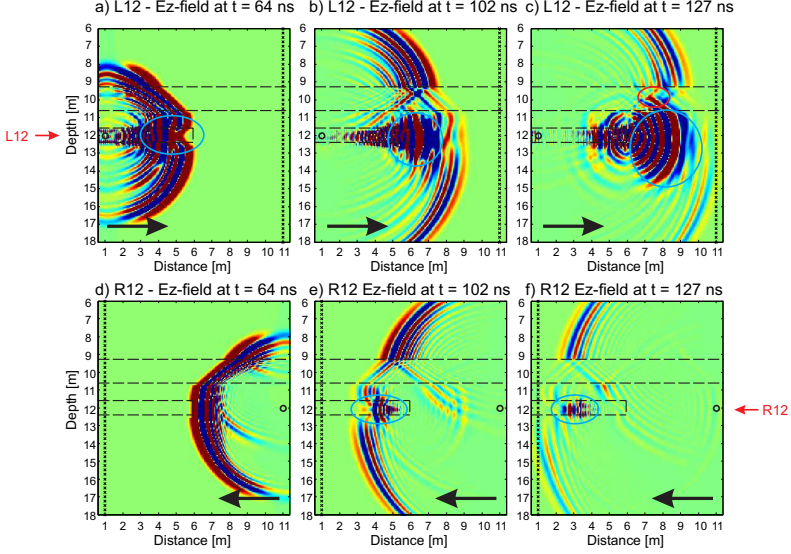
73

Figure 5.2: Forward modeled snapshots of the electrical field distribution for transmitter L12 and R12 of the synthetic model shown in Fig.5.1a, whereas the black dashed lines indicate the waveguide, at a) 64 ns, b) 107 ns and c) 127 ns. The transmitter and receiver positions are indicated by the black circles and crosses, respectively. The blue and red circles indicate events that are discussed in the text.

critical angle and both transmission and reflection can occur. Since the wave speed above and below the waveguide have the same fast wave speed, two interfering head waves from above and below the waveguide can be identified at 127 ns (Fig. 5.2c). We can also clearly see how the energy is minimized by this interference (indicated by the red circle) which causes a minimum in the measured trace energy as can be observed in Figure 5.1 indicated by the purple circle.

5.2 Waveguide detection using amplitude analysis

In Chapter 4, we introduced an amplitude analysis approach to identify and detect horizontally continuous waveguiding structures. This approach can be extended for the analysis of lateral discontinuous waveguides based on the modeling observations described in the previous section and can be divided into three steps. In the first step, the trace energy (summation of the squared amplitude) for each receiver position is calculated and transmitters are identified where receivers have one or two orders of magnitude higher

energy levels at certain depth intervals compared to receivers located outside of these ranges. These high energy levels indicate elongated late arrival wave trains due to the presence of a low-velocity waveguide and a distinct maxima peak in the trace energy can be picked. In the second step, the trace energy is calculated and analyzed for all the other transmitter positions. Generally, for transmitters outside of a waveguide region, intermediate amplitudes and energies are detected in the data for most of the receiver positions in the opposite borehole, whereas for the receivers straddling a waveguide, significantly diminished amplitudes and a minimum in trace energy can be observed in the depth region around the previous found maxima. The minima for each of the transmitter positions are picked when they have at least one order of magnitude smaller amplitudes compared to the picked maxima.

These minima and the reduced amplitudes in the data are caused by interferences of the head waves emitted by the electromagnetic wave from above and below the waveguide that are interfering in the waveguide layer and eliminate each other as shown in Figure 5.2c. With increasing distance of the transmitter to the waveguide the position where the head waves are interfering are directing to the waveguide boundaries. Therefore, in the third step, the obtained maxima and minima positions are plotted at the corresponding receiver depths, where the maxima are present within the waveguide layer and the minima positions are indicated the upper and lower boundaries of the waveguides.

When high amplitude elongated wave trains can be identified for transmitters in both boreholes at similar depths (similar to Fig. 5.1 for L10 and R10), this indicates the presence of a continuous waveguide present between the two boreholes. When high amplitude elongated wave trains on the opposite borehole spreaded late arrival high amplitudes can be identified for only one borehole, as shown in Figure 5.1 for R11 - R13 and L12, respectively, this indicates the presence of a discontinuous waveguide having a limited lateral extent (see Fig. 5.1a). With increasing lateral extent of a discontinuous waveguide between two wells, the spreading of the high amplitudes decreases until elongated wave trains can be observed in both boreholes as in the case of a continuous waveguide. In contrast, when the lateral extent is decreasing between the boreholes, the spreading of the high amplitudes will increase and lower amplitudes will be sensed by the receivers. Consequently, using this information and analyzing the intensity of the spreading of the high amplitudes allows for a qualitative estimation of how far the waveguide extends between the boreholes to be made. For a quantitative high resolution distribution estimation of the medium properties, the full-waveform inversion is still necessary.

5.2.1 Amplitude analysis for different synthetic models

In the following, we will analyze six synthetic models I - VI with different thicknesses, layering, dipping, and the extent of one or two low-velocity waveguides present between two boreholes (Fig. 5.3a). The maxima and minima positions in the trace energy profiles for each of the transmitter positions are shown in Figures 5.3b - e and the picked maxima and minima positions from the trace energy profiles were plotted against the receiver depth as shown in Figures 5.3f and g by red and green crosses.

For model I (first row of Fig. 5.3) the waveguide layer, indicated by the blue lines, has a thickness of 0.5 m and for each of the reciprocal setup, one transmitter L10 and R10 is located within this layer, marked by the thick black circle. For both of these transmitters a distinct maximum in the trace energy profile is observed at 10 m depth, having a magnitude three times higher than a transmitter located outside of this zone. For all the transmitter positions located outside the waveguide, a clear distinct minimum in the trace energy is visible for receivers present within the waveguide layer. Moreover, a plateau of minimum values is present which indicates the thickness of the waveguide. The trace energy profiles for planes LR and RL are identical due to the symmetric waveguide spanning between the boreholes. By plotting the picked maxima and minima positions from the trace energy profiles against receiver depth (Figs 5.3f and g), we see that the thickness of the waveguide is too thin for the receiver sampling of 0.25 cm to precisely define the boundaries of the waveguide using the amplitude analysis.

For synthetic model II (second row of Fig. 5.3)) the waveguide thickness is increased to 1 m (equal to the transmitter spacing). A similar behavior of the trace energy profiles to model I is observed, and the picked minima positions from the amplitude analysis represents the boundaries of the waveguide exactly due to the increased thickness of the layer.

When two transmitter positions are located in a waveguide with a thickness of 2 m as shown in the model III (third row of Fig. 5.3), and two waveguides are present between the boreholes, two maxima in the trace energy profiles can be observed for both layers. Similar to the other models, for each of the profiles, clear minima in a certain range spanning the thickness of the waveguide are visible. The picked minima positions precisely identify the boundaries of the waveguide, when transmitter positions with a larger distance from the waveguide are used. Also, for other models (not shown) we observed the trend that with increasing thickness of the layer, more transmitter positions with a higher distance to the waveguide are necessary to precisely estimate the waveguide boundaries.
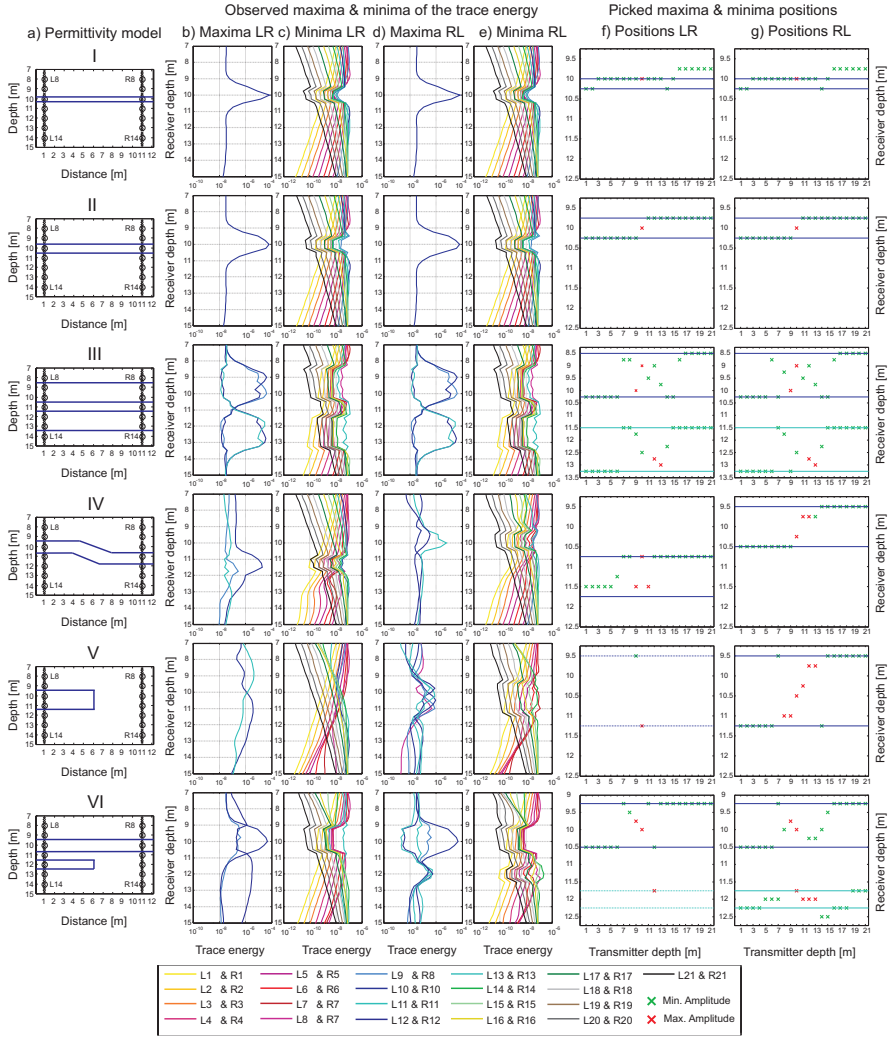
Figure 5.3: a) Synthetic permittivity models I - VI. b) - e) Maxima and minima of trace energy profiles for the reciprocal measurement setups LR and RL. Note, that the maxima and minima traces have a different x-axis range and each transmitter has a certain color affiliation. f) LR and g) RL picked positions of the maxima (red crosses) and minima (green crosses) of the trace energy for each transmitter along receiver depth. The blue lines indicate the waveguide boundaries close to the corresponding borehole in which the receivers are located.

77

In the case of a dipping waveguide, in model IV, the amplitude analysis is able to identify the waveguide and detect the boundaries at both sides of the waveguide. The picking of the maxima positions is more challenging and the trace energy is reduced compared to a non-dipping waveguide, due to that the dipping of the layer has an influence on the angle of the critical reflected waves in the waveguide. Energy which was critical before is now transmitted and not reflected anymore such that less energy is trapped. Furthermore, with the increasing angle of the dipping layer, less energy is trapped in the waveguide and more energy is released in the surrounding medium.

Model V is a discontinuous waveguide with a limited lateral extent where no clear maxima or minima can be identified in the profiles for the LR plane for either of the transmitters located within the waveguide, similar to the wave propagation observed in Figures 5.1 and 5.2. For the RL plane, we observe six maxima in the trace energy profiles (one magnitude higher than the minima profiles) for receivers straddling the waveguide depth. Using the information from the picked maxima and minima positions, the boundaries of the waveguide close to the borehole can again be identified. The minima plateaus of the plane RL indicate the thickness of the layer. In the last synthetic model VI, we combine a horizontal continues layer and a discontinuous waveguide (see also Figs 5.1 and 5.2). Similar to model II and V, where only one transmitter is located inside the waveguide, the boundaries of the waveguide layers can be obtained using the extended amplitude analysis approach.

In summary, when a waveguide is continuous between the boreholes similar wave fields with clear high amplitude elongated wave trains at the same depth of a reciprocal setup are present. Whereas, when at either side a possible discontinuous waveguide or a dipping waveguide is present, it is necessary to check if on the other side high amplitude spreading in the data occurs or if a second elongated wave train is present at a different depth, respectively.

5.2.2 Influence of permittivity and conductivity on waveguide behavior

Here, we test the influence of higher and lower permittivity and conductivity values of the waveguide. In theory, a low-velocity waveguide can either be caused by an increase of porosity in saturated media (high permittivity) or by an increase of clay content (high conductivity and high permittivity). It is not clear if the increased attenuation due to the higher conductivity of clay can compensate the high amplitudes that can be observed in the presence of a low-velocity waveguide. Therefore, we use a synthetic model with a waveguide of 2 m thickness (Fig. 5.4a), where two transmitters for each of the reciprocal

measurements are located inside the waveguide. First, we vary the relative permittivity value of the waveguide layer using $\varepsilon_{r1} = 26$ (similar to Figs 5.1 - 5.3), $\varepsilon_{r2} = 30$ and $\varepsilon_{r3} = 20$, with a homogeneous conductivity of $\sigma = 8.5$ mS/m. The critical angles are given by $\theta_{C1}(\varepsilon_r = 26) = 42.8°$, $\theta_{C2}(\varepsilon_r = 30) = 39.2°$ and $\theta_{C3}(\varepsilon_r = 20) = 50.8°$. As expected, the trace energy for the two transmitters L10 and L11 increases with increasing permittivity within the waveguide due to the decreased critical angle which traps more energy within the waveguide (Fig. 5.4b). Consequently, higher permittivity causes larger maximum trace energy and corresponding maxima are more distinct and can be better picked.
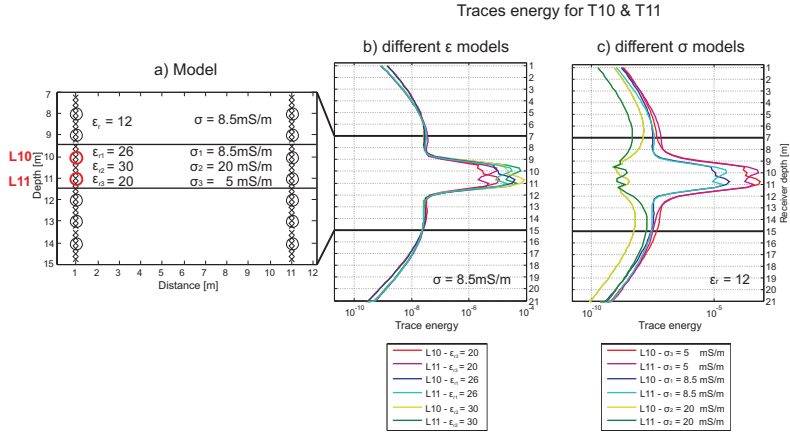
Figure 5.4: a) Permittivity and conductivity models used for generating synthetic data. b) Comparison of the T10 and T11 trace energy profiles (both located in the waveguide) when applying different permittivity values for the waveguide while the conductivity was homogeneous 8.5 mS/m. c) Comparison of the trace energy profiles for T10 and T11 when applying different conductivity values for the waveguide while the relative permittivity has a value of 26 within the waveguide.

Second, we defined three synthetic models using different conductivity values for the waveguide layer: $\sigma_1 = 8.5$ mS/m (homogeneous space), $\sigma_2 = 20$ mS/m (representative value for clay) and $\sigma_3 = 5$ mS/m, while the permittivity is constant in the layer with $\varepsilon_r = 26$ ($\theta_C = 42.8°$). It is clearly visible that in the case of a higher conductivity (Fig. 5.4c, green lines) no maximum in the trace energy for transmitters located in the waveguide can be observed due to the conductivity induced attenuation of the electromagnetic wave. In contrast, for a smaller conductivity (Fig. 5.4c, red lines) higher trace energy is detected. Additionally, in all cases distinct minimum positions and corresponding minimum plateaus in the trace energy are observed for the transmitter located outside the waveguide (not shown). This study clearly indicates that in the case of high trace energy forming a distinct

maximum (more than one order of magnitude higher) and in the presence of elongated wave trains, the waveguide is caused by a change in the porosity or soil water content. By contrast, when no elongated wave train and no distinct maxima in the trace energy profiles but still diminished minima positions and minima plateaus can be observed, the waveguide is probably caused by a change in clay content.

5.3 Experimental study: Boise Hydrogeophysical Research Site

We applied the extended amplitude analysis and full-waveform inversion to an experimental dataset acquired at the Boise Hydrogeophysical Research Site (BHRS) which is located 15 km from Boise, Idaho, USA.

5.3.1 Field site and geological background

The BHRS test site was designed to achieve a better understanding of the potential of geophysical methods and to obtain 3D distributions of geophysical, geological and hydrological parameters. During the last two decades, several studies were carried out using different methods to characterize the aquifer (Barrash *et al.*, 1999; Clement *et al.*, 1999; Barrash & Reboulet, 2004; Tronicke *et al.*, 2004; Clement & Barrash, 2006; Oldenborger, 2007; Bradford *et al.*, 2009; Mwenifumbo *et al.*, 2009; Bradford, 2010; Dafflon *et al.*, 2011a; Straface *et al.*, 2011). The test site is located close to the Boise River and installed boreholes are arranged within a diameter range of 20 m (Figs 5.5a and b). The aquifer is formed by an 18 m - 20 m thick layer of heterogeneous coarse cobble-sand, fluvial deposits, and an underlying red clay formation that forms the aquitard. (Barrash & Clemo, 2002) subdivided the aquifer into five hydrostratigraphic units primarily by using porosity differences: four cobble-dominated units and one sand unit (see Fig. 5.5c and Table 5.1). The crosshole GPR dataset was provided by the Department of Geosciences of the Boise State University for the SEG-AGU Hydrogeophysics workshop 2012 (more details can be found at www.seg.org/events/upcoming-seg-meetings/hydrogeo2012). The data were acquired in October 2011 using the Sensors and Software pulseEKKO Pro system with 100 MHz antenna in the boreholes C5 and B1, which are approximately 10 m apart and slightly tilted (indicated in Fig. 5.5a). We employed a semi-reciprocal crosshole GPR geometry (Fig. 5.5c), where there were 16 transmitter positions and 64 receiver positions in each borehole below the ground water table. The vertical spacing of the transmitter and receiver positions is 1 m and 0.25 m, respectively. In the following, we introduce the notation convention for the transmitter positions in boreholes C5 and B1, that the
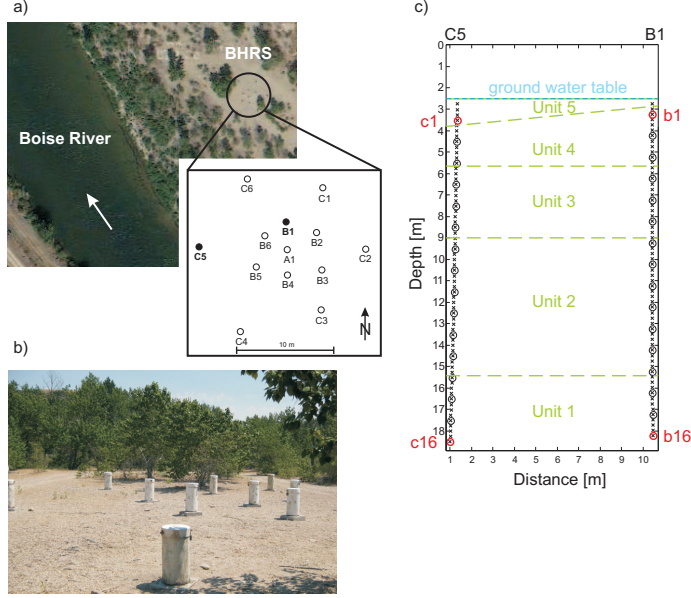
Figure 5.5: a) Overview of the BHRS showing the location of the installed boreholes close to the Boise River. The white arrow is indicating the flow direction of the river. The GPR measurements, which were used for the full-waveform inversion, were performed in the two black marked boreholes C5 and B1. b) Picture of the test site showing some of the boreholes. c) Schematic setup of the investigation area between C5 and B1 where the transmitter and receiver positions are shown with circles and crosses, respectively. The ground water table is at approximately 2.5 m depth. Marked in green are the different units obtained by Barrash & Clemo (2002), which can vary in depth over the entire test site.

positions are numbered from c1 - c16 and b1 - b16, respectively. The groundwater table was at approximately 2.5 m depth during the measurements and c1 and b1 are located at 3.5 m and 3.2 m depth, respectively.

5.3.2 Waveguide detection using extended amplitude analysis

High amplitude late arrival elongated wave trains are observed in the data of transmitters c1 - c3 and b1 - b3, which are present directly below the water table (Figs 5.6a and b). Wave-guiding structure I is identified directly below the water table for both sides of the measurements in the data of transmitters c1, b1 and b2, as indicated by the red circles. For these three transmitters, we observe clearly high amplitude late arrival elongated wave

81

Table 5.1: Mean porosity values and dominate compositions of the five hydrostratigraphic units of all wells located in the central part at the BHRS estimated from core and Neutron-Neutron porosity logs (Bradford *et al.*, 2009).

Unit	Approximate thickness [m]	Mean porosity [%]	Porosity variance [%]	Dominant composition
5	0-4	42.9	0.3	Coarse sand
4	1-5	23.3	0.2	Pebble/cobble dominated
3	3	17.2	0.06	Pebble/cobble dominated
2	6	24.3	0.2	Pebble/cobble dominated
1	2	18.2	0.06	Pebble/cobble dominated
Mean		25.2	0.4	

trains, which are more spread out for the c1 data. This asymmetry indicates that the waveguide is not continuous and does not extend laterally to borehole B1. Wave-guiding structure II is indicated by the blue circles between 5 m - 6 m depth, which have lower amplitudes and are more spread out for c2 and c3 compared to b2 and b3. Moreover, a distinct reduced velocity indicated by the green circles can be observed for the b2 and b3 transmitters. Again a clear asymmetry is present which indicates that wave-guiding structure II has also a reduced lateral extent and is not continuous in between the two boreholes. These observations are very similar to the observations for the synthetic studies V and VI (see Fig. 5.3), where a waveguide was present with a limited lateral extent.

The picked maxima and minima positions of the trace energy profiles in the depth range where the high-amplitude elongated wave trains were identified are shown in Figs 5.7a - c and 5.7d - f for the C5 B1 and B1 C5 planes, respectively. Two clear maxima can be observed for transmitter gathers c1 and c3 (red crosses in Fig. 5.7a). The minima positions indicated (green crosses in Fig. 5.7b) are less clear to distinguish around the picked maximum at about 3.5 m depth. The minima positions around the picked maximum at 5.3 m are not very pronounced, but allow an easy picking. Due to the location of both wave-guiding structures close to the water table, there are no transmitter positions above the layers to define the boundaries of the wave-guiding structures in more detail. Also, the picking of the maxima and minima is more challenging due to the less pronounced maxima and minima positions in the profiles. Using the picked maxima and minima positions along the receiver depth we identify the boundaries of the wave-guiding structures close to borehole B1 (black lines in Fig. 5.7c). For plane B1 - C5 also clear maxima can be identified (Fig. 5.7d). Moreover, very distinct minima positions in the
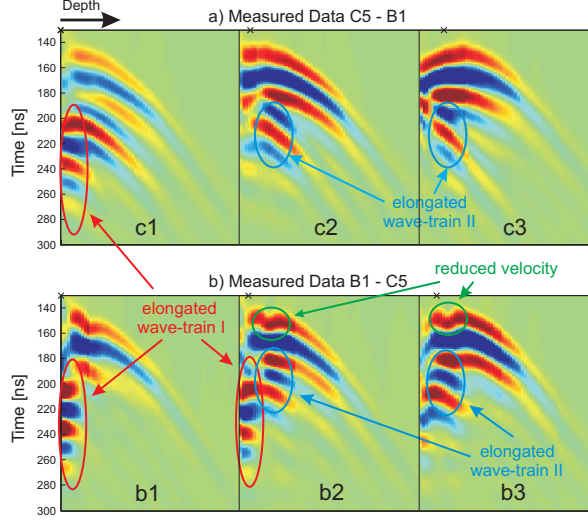
Figure 5.6: Measured data for transmitters a) c1 - c3 and b) b1 - b3, respectively. The position of the transmitter is indicated by the black crosses, whereas c1 and b1 are located close to the water table at 3.5 m and 3.2 m depth, respectively. The observed phenomena indicating wave-guiding structures are marked by red and blue circles. The reduced velocity in combination with the high amplitude elongated wave train II are indicated in green. For both images the same amplitude scale is used and the true amplitudes are shown, where high and low amplitudes are indicated by red and blue color, respectively.

trace energy profiles can be observed, especially between 5 - 6 m depth, which enables better identified boundaries of the waveguide (Fig. 5.7f). The clearer minima and the reduced velocities that can be observed when the transmitters are located in borehole B1 both indicate that the waveguide is present at borehole C5, whereas it is not present anymore at borehole B1. To determine the lateral extent of the two wave-guiding zones, we performed the full-waveform inversion of the data that provides high resolution images of the aquifer.

5.3.3 Full-waveform inversion results

The starting models for the full-waveform inversion are obtained by performing a ray-based travel-time and first-cycle amplitude inversion (Figs 5.8a and b). The permittivity model shows an intermediate permittivity layer which is embedded between lower permittivity layers. Due to the small variety of the conductivity values we chose a homogeneous starting model for the full-waveform inversion with 8.5 mS/m, which represents the mean
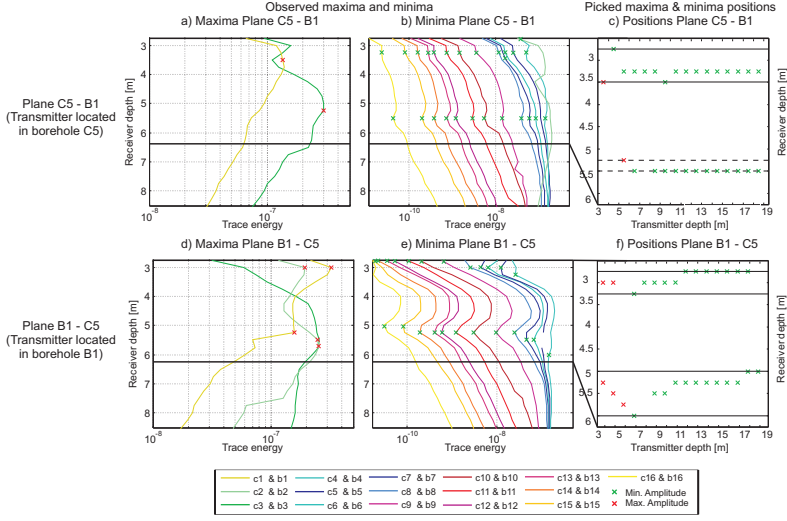
Figure 5.7: a) And d) maxima, b) and e) minima of trace energy profiles of the measured data, and c) and f) picked positions for the planes C5 - B1 and B1 - C5, respectively. The red and green crosses indicate the position of the maxima and minima of the energy, respectively. The black lines are indicating the estimated waveguide boundaries using the amplitude analysis close to the corresponding borehole B1 and C5, respectively.

value of the first-cycle amplitude inversion. The estimated effective source wavelet, shown in the corner of Figure 5.8b, was obtained by using the starting models and following the approach presented in Chapter 3. In the ε_r and σ full-waveform inversion results using the ray-based results as the start models (Figs 5.8c and d) the three main layers, which were obtained by the travel time inversion (see Figs 5.8a and b), are resolved with a higher resolution and the RMS error is reduced to 61.4 % (ray-based results are 100 %). Below 18 m depth in the tomogram (Fig. 5.8d), the underlying clay is indicated by higher values. Still a significant misfit is present between the measured data for the c1, c2, b1 and b2 transmitters close to the water table (Figs 5.9a and d) that contain the waveguide characteristics and the inverted data. This indicates that the starting model close to the water table obtained by the ray-based inversion is not reliable, which is probably due to the low ray-coverage close to the water table and the bottom of the inversion domain. When these unreliable results are used as the starting model for the full-waveform inversion, and the synthetic data calculated for the starting model have less overlap than half a wavelength, cycle skipping can occur and the full-waveform inversion cannot converge to the correct model (Meles *et al.*, 2011; Virieux & Operto, 2009).
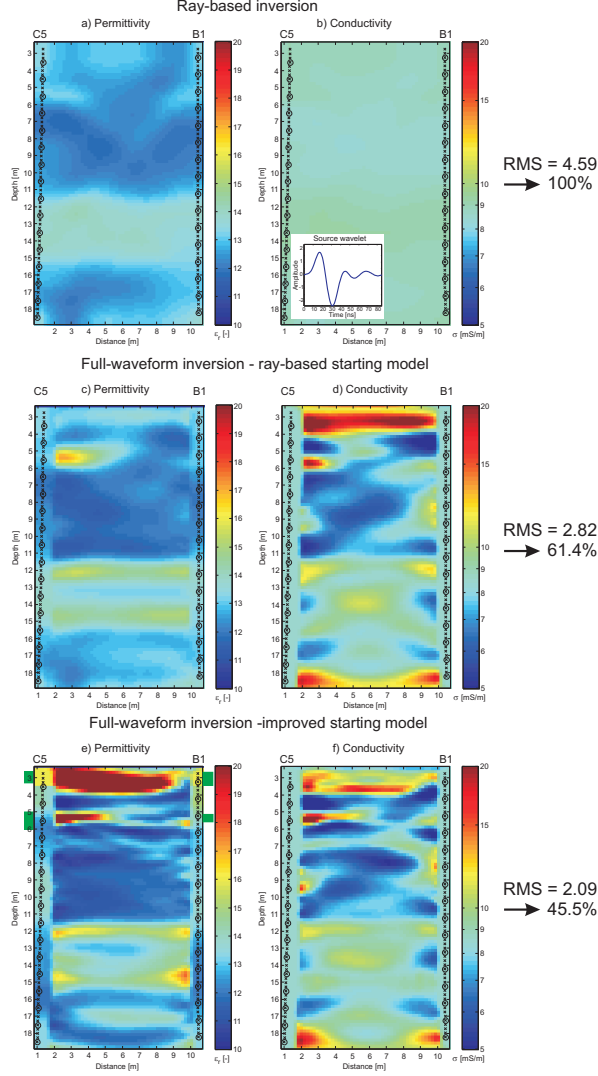
Figure 5.8: Ray-based a) permittivity and b) conductivity models obtained by the travel time and first-cycle amplitude inversion, respectively. Transmitter and receiver positions are marked with circles and crosses, respectively. Inset in b) shows the estimated effective source wavelet. c) Permittivity and d) conductivity results estimated by the full-waveform inversion using the ray-based starting models as shown in a) and b), respectively. In e) and f) the final permittivity and conductivity models are shown obtained by the full-waveform inversion using the improved starting models. The green boxes on the left and right side of e) indicate the boundaries of the wave-guiding structures obtained from the amplitude analysis.
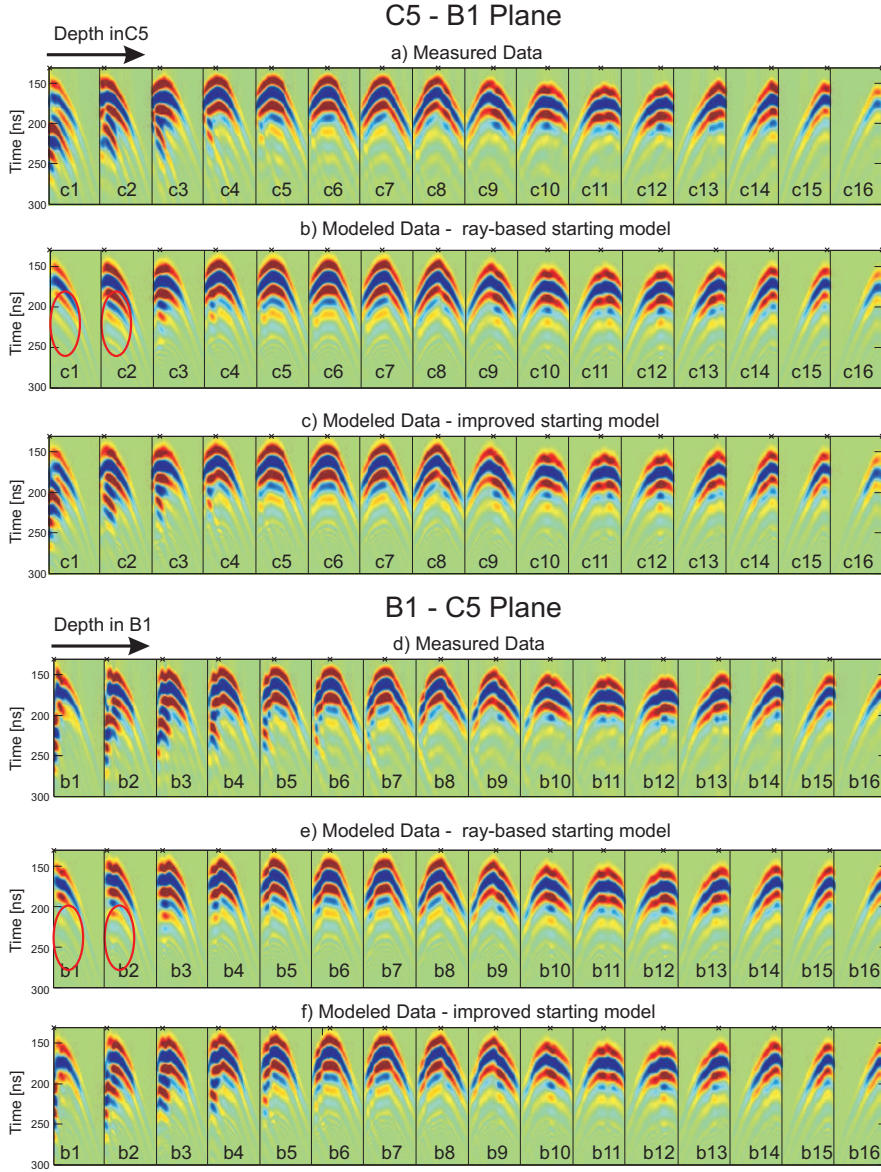
Figure 5.9: a) And d) measured data, and full-waveform modeled data using b) and e) the ray-based and c) and f) the improved starting model for the planes C5 - B1 (transmitters located in C5) and B1 - C5 (transmitters located in B1) with their true amplitudes, whereas positive and negative amplitudes are indicated by red and blue in the images, respectively. The black crosses illustrate the transmitter position.

Here, the information gained from the extended amplitude analysis, which indicates the presence of two discontinuous wave-guiding structures close to the water table, is incorporated in the starting model by assuming a homogeneous higher permittivity ($\varepsilon_r = 17$) layer between the water table and 4 m depth. In this way, the starting model yields synthetic data that has an overlap with the measured data within half the dominant wavelength such that a convergence is possible towards the global minimum.

The root-mean-squared (RMS) error between the measured and modeled data, using the updated ε_r starting model, is reduced to 45.5 % and a very good fit is visible between the modeled and measured data in shape, phase and amplitude shown in Figures 5.9a, d and c, f, respectively, for both acquisition planes including the high amplitude late arrivals caused by the two waveguides (see transmitter c1 - c3 and b1 - b3), which indicates the reliability of the obtained model.

The final ε_r and σ full-waveform inversion results (Figs 5.8e and f) show a high permittivity waveguide layer with a thickness of about 1 m present between the water table, and 4 m depth which extends from well C5 up to one meter before well B1 and then disappears. A high ε_r layer between 5 - 6 m depth is also present close to borehole C5 which extends for about three meters towards B1 and then disappears. The wave-guiding structures and boundaries obtained by the amplitude analysis (see Fig. 5.7 and green boxes in Fig. 5.8e) are confirmed by the full-waveform inversion result including the indications that the waveguides start at borehole C5, but do not extend until borehole B1. Whereas the amplitude analysis is not able to determine the lateral extent of the two waveguides, the full-waveform inversion exploits all information present in the measured data and images the waveguides with high resolution. The two wave-guiding layers are not identified by the ray-based approach (see Figs 5.8a and b) due to ignoring the late time high-amplitude arrivals.

To investigate the wave propagation within the waveguide, we perform a forward modeling for transmitters c1 and b1 using the final r and full-waveform inversion results, similar to that shown in Fig. 5.2. Within the snapshots of the vertical electrical wave field of c1 and b1 at time 76 ns (Figs 5.10a and d), we observe that most of the radiated energy is trapped between 2.5 - 4 m depth, whereas for c1 a clear velocity reduction below 4 m depth is visible indicating the waveguide boundary, which is less clear close to borehole B1. At a time of 102 ns (Figs 5.10b and e), the trapped wave field can be clearly observed in both cases. At time 127 ns the wave field emitted from c1 (see Fig. 5.10c) starts to spread out since it is not trapped in the waveguide anymore. Therefore, a reduced maximum in the trace energy can be observed (similar to the synthetic examples in Fig. 5.2). The wave field emitted from b1 (see Fig. 5.10f) is still trapped in the waveguide and formed an elongated wave train with less spreading in the data showing a clear maxima in

the trace energy. Similar behavior of the electrical field of the synthetic study (Fig. 5.2), whereas the boundaries of the synthetic study presented a sharp contrast and therefore, the trapping and spreading of the wave field can be better observed.
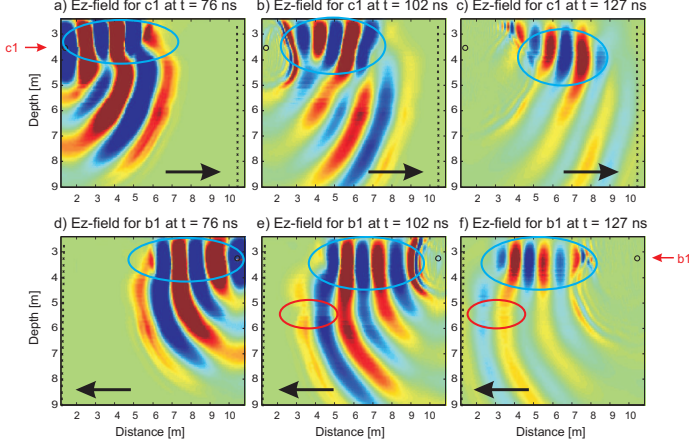

Figure 5.10: Forward modeled snapshots of the electrical field distribution for transmitter a) - c) c1 and d) - f) b1 for different time steps. The transmitter c1 and b1 position are indicated by the black circle. The blue and red circles indicate events caused by the two different waveguides layers.

5.3.4 Comparison of the full-waveform inversion results and logging data

To validate the waveform inversion results and the findings of the energy analysis, we compare the results to Neutron-Neutron porosity logs acquired in the wells C5 and B1 (see Fig. 5.11). Therefore, we converted the final waveform ε_r results into porosities Φ using the two-component CRIM equation for saturated aquifer. Solving for porosity, the CRIM equation gives

$$\Phi = \frac{\sqrt{\varepsilon} - \sqrt{\varepsilon_S}}{\sqrt{\varepsilon_W} - \sqrt{\varepsilon_S}} \tag{5.2}$$

where ε_W and ε_S are the permittivity of water and the sediment, respectively. Here, we used $\varepsilon_W = 80.36$ and $\varepsilon_S = 4.6$ similar to Barrash & Clemo (2002). Additional porosity logging data is available for borehole B6 (see Fig. 5.5), which is located close to the acquisition plane. For the full-waveform inversion porosity values of C5, B1 and B6, we use the mean of three cells next to the borehole (red graphs). The result from the

waveform inversion shows a good correspondence with all the logging data, especially in the upper part outlining the different thicknesses of the high porosity/permittivity zone.
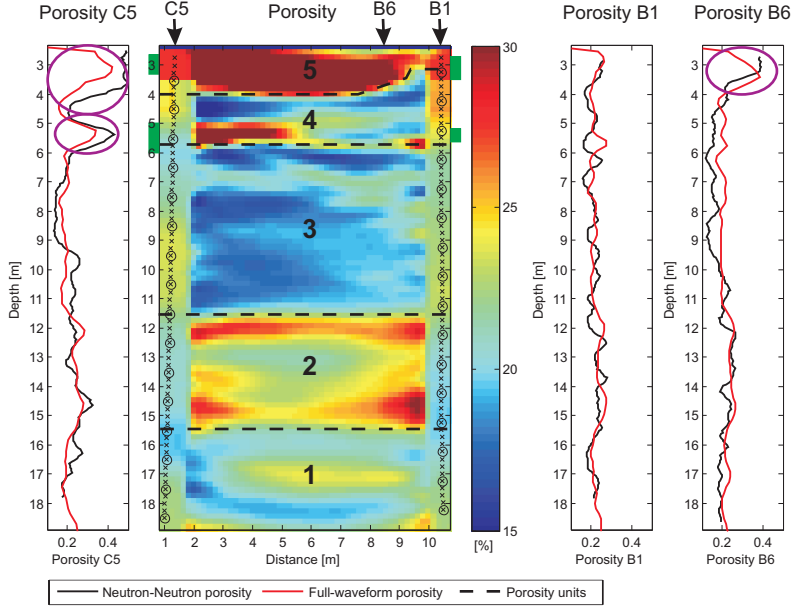

Figure 5.11: Converted full-waveform inversion porosity compared to Neutron-Neutron logging data (black graphs), acquired in boreholes C5, B6 and B1. The full-waveform inversion porosities close to the borehole locations are plotted as red graphs. The green boxes next to the image plot indicate the boundaries of the wave-guiding structures obtained from the amplitude analysis. The position of the boreholes corresponding to the image plot is marked by the black arrows. The numbers from 1 - 5 and the black dashed lines are indicating the different porosity units. The purple circles are indicating high porosity zones in the logging data.

The logging data follows the trend of the high porosity zones from the full-waveform inversion, indicating that the wave-guiding layer between 2.5 m - 4 m depth is more pronounced close to well C5, is still present in well B6, but almost absent in B1 (see purple circles). The second waveguide zone is only indicated in well C5, and absent in well B1 and B6. Consequently, this zone vanishes between well C5 and B6 (see dashed black lines in C5 and B6). These layers are caused by a change of low porosity ($\approx 20\%$), poorly sorted sand and gravel units to high porosity sand units ($\approx 40\%$). Both layers are also visible in the logging data of well C5 (purple circles). In the image plot of the full-waveform porosities the five possible different hydrostratigraphic units are indicated

by the black lines. The ray-based porosity shows only small variations in the porosity for the different units, whereas the full-waveform inversion resolved the porosity of each unit close to the values obtained by Neutron-Neutron data (see Table 5.2).

Table 5.2: Porosity estimates based on Neutron-Neutron logging data (mean value of all boreholes located in the center of the test site; see Tab. 5.1), ray-based and full-waveform inversion results for each of the hydrostratigraphic units indicated in Figure 5.11.

Unit	Approximate thickness [m]	Neutron-Neutron mean porosity [%]	Ray-based porosity [%]	Full-waveform porosity [%]
5	0 - 4	42.9	21.9	39.1
4	1 - 5	23.3	21.9	22.3
3	3	17.2	19.7	19.3
2	6	24.3	23.8	24.1
1	2	18.2	21.5	21.8
Mean		25.2	21.7	25.3

5.4   Conclusions

We have investigated the complicated wave phenomena occurring due to the presence of a low-velocity waveguide layer present between two boreholes. For transmitters located within a waveguide, at least one order of magnitude higher trace energy, a delayed travel time, and late arrival elongated wave trains are observed for receiver positions straddling along this zone. These elongated wave trains are formed due to the trapping of the waves within the waveguide caused by total reflection beyond the critical angle. For receiver positions within the waveguide, a distinct minimum in the trace energy is present when the transmitter are located outside the waveguide due to the interference of the head waves from above and below the waveguide. The picked minima positions identify the boundaries of the waveguide, especially for positions at larger distance from the waveguide. This amplitude analysis has been performed for different synthetic models showing that it is able to detect low-velocity waveguides with different thicknesses, lateral extents and orientations (dipping) and returns the waveguide boundaries close to the boreholes. If the thickness of the waveguide is smaller than the sampling rate of the transmitter or receiver, the estimation of the boundaries is more challenging. In the case that no transmitter position is located in the waveguide and consequently no maxima occurs, the minima position of the trace energy and the corresponding minima plateau can still be used to

identify waveguides. For a continuous horizontal or dipping waveguide present between two boreholes, similar wave fields with clear high amplitude elongated wave trains and minima positions at similar or different depths of the reciprocal setup can be identified.

The amplitude analysis is extended for the presence of a discontinuous waveguide that is connected to only one borehole. Here, minima positions and increased amplitudes, reduced velocity and elongated wave trains can only be detected for the receivers within this borehole, and still can be used to estimate the location and thickness of the waveguide. For receivers present in the other borehole, that is not connected to the borehole, significant late arrival high amplitude spreads are sensed in the data for the transmitter present at the waveguide depth, which is caused by the initial trapping of the waves within the waveguide followed by the release of the trapped wave energy when the waveguide is not present anymore. By analyzing the intensity and the spreading of the high amplitude energy, a qualitative estimation can be made how far the waveguide extends between the boreholes.

Investigating the influence of different permittivities and conductivities it has been shown that in the presence of elongated wave trains, the waveguide is most probably caused by a change in porosity rather than a change in clay content, since for high conductivities the peak maxima in the trace energy is missing. The presence of a high conductive low-velocity waveguide can still be characterized using the minimum amplitudes. Note that also for sparse sampling of the sources a thin waveguide will exhibit similar phenomena and show minima positions and no elongated wave trains.

The extended amplitude analysis was applied to an experimental dataset from the BHRS, where we were able to detect two discontinuous wave-guiding structures close to the water table. For both waveguides, significant spreading of late arrival high amplitudes could be observed, indicating for both waveguides a limited lateral extent similar as observed in the synthetic study. This information gained from the amplitude analysis was helpful to improve the starting model for the full-waveform inversion. The final full-waveform inversion of this data showed two high permittivity layers close to the water table whereas one layer was only present until the center of the domain (5 - 6 m depth) and the other almost for the entire distance of the boreholes (2.5 - 4 m depth). The obtained boundaries of the amplitude analysis were confirmed by the full-waveform inversion. Comparison with Neutron-Neutron logging data showed a good agreement with the converted full-waveform porosity. The lateral extent of the waveguide between 2.5 - 4 m depth was also confirmed in the Neutron-Neutron porosity logging data and indicated the origin of the waveguides as a change between sand and gravel in the aquifer. The mean porosity of the Neutron logging data and the full-waveform inversion for the different hydrostratigraphic units were in good correspondence. The amplitude analysis and

crosshole GPR full-waveform inversion enables a detailed characterization of waveguides, and can be applied to a wide range of geological, hydrological, glacial, and periglacial studies, and improve our ability to monitor and visualize important small scale processes in the subsurface.

Chapter 6

Conclusions and Outlook

In the following Chapter the main findings for advancements in the application of crosshole GPR full-waveform inversion for hydrogeological applications are presented. The outlook summarizes possible future research topics.

6.1 Conclusions

During this dissertation, we applied the extended crosshole GPR full-waveform inversion to two different saturated aquifers using an optimized acquisition setup to reduce computational cost and acquisition time and still remain a dense ray-coverage. Thereby, the final permittivity and conductivity results of the full-waveform inversion showed decimeter-scaled high resolution images in contrast to the low-resolution ray-based inversion results. The reliability of the results was indicated by the good fit between the measured and modeled data in phase and true amplitudes, and was evaluated using logging data acquired in the same boreholes. Further, we demonstrated the importance of a good starting model and effective source wavelet to reliably invert for the entire inversion domain. Additional constraints on the starting model are usually required for the region close to the water table due to the presence of reflected waves caused by the high contrast to the unsaturated domain above.

In the final full-waveform inversion results of one crosshole plane of the Thur River data, we were able to identify a higher permittivity zone, which acted as an electromagnetic low-velocity waveguide, between 5 m - 6 m depth. This zone was caused by a high porosity and affected characteristic electromagnetic wave behavior. For transmitters located within this zone, high amplitude and late arrival elongated wave trains were observed for receivers straddling in this zone. However, for the same receivers a distinct minimum in the trace energy spectrum was detected for transmitters located outside this

zone.

The 3D characterization of the gravel aquifer and the low-velocity zone was achieved by applying the 2D code to six crosshole planes located in a square configuration and stitching them together to construct pseudo-3D models. For all the planes sub-wavelength high resolution images for permittivity and conductivity were estimated by using the full-waveform inversion. At the borehole locations and the intersections of the planes similar structures for the permittivity were obtained (less good for conductivity), indicating that the 2D assumptions of the method are valid. In all six permittivity planes a high permittivity zone, which acts as a waveguide between 5 m - 6 m depth was resolved. To gain more information about this waveguide zone, we analyzed the measured data in more detail and developed a new amplitude analysis approach that was able to detect and identify wave-guiding structures and their boundaries already in the measured data without applying any inversion. Therefore, the positions of the maxima and minima of the trace energy spectra were picked and plotted against the receiver depth. Such information obtained by the amplitude analysis can be used to improve the starting models for the inversion. Permeability estimates indicate a zone of preferential flow between 5 m and 6 m depth, which corresponds well with the high permittivity/ high porosity zone obtained by the full-waveform inversion. The converted full-waveform porosities showed a good correlation with Neutron-Neutron logging data acquired in the center of the diagonals. The conductivity images identified the boundary of the underlying lacustrine sediments below 9.6 m depth which was also confirmed by Natural gamma logging data.

Finally, we extended the newly developed amplitude analysis approach and explored the potential to detect and identify discontinuous or dipping waveguides by applying the method to different synthetic models. By analyzing the wave propagation of the electrical field for a discontinuous waveguide, we observed a characteristic wave behavior, that is different compared to a continuous waveguide. Within this study, we found that the amplitude analysis method is able to detect waveguides and their boundaries for different thickness, extensions and dipping of the waveguide layer. However, the successful application of the method depends on the spatial sampling of the receivers. If a waveguide layer is thinner than the sampling rate, the boundaries of the layer are not accurately detected. Furthermore, in the presence of elongated high amplitude wave trains, the waveguide is most properly caused by porosity changes. In contrast, when no elongated wave train is detected, the waveguide is caused by changes in the high conductivity (e.g. high clay content).

We applied the amplitude analysis and the full-waveform inversion to experimental crosshole GPR data acquired at the BHRS and were able to detect two discontinuous waveguides between the wells that show similar wave characteristics as found in the syn-

thetic model. The full-waveform inversion results confirmed the presence of the discontinuous waveguides and revealed more details of the waveguide structures. Converted full-waveform porosities are compared with Neutron-Neutron logging data and confirmed the reliability of the full-waveform inversion results.

Summarizing, to invert data with the full-waveform inversion technique a proper sampling, a correct starting model, and a good effective source wavelet are necessary. Altogether, we demonstrated the potential of the crosshole GPR full-waveform inversion, that uses all phase and amplitude information contained in the measured data, to image complicated structures within sub-wavelength resolution for both permittivity and conductivity including high contrast layers to characterize saturated aquifers. Such small scale high contrast layers are important for an improved understanding of flow and transport processes. The new amplitude analysis approach enables a direct detection of wave-guiding structures and their boundaries in the measured crosshole GPR data without applying any inversion. Moreover, the full-waveform inversion and the amplitude analysis method can be applied and extended to a wide range of applications including geological, hydrological, glacial, and periglacial studies and thereby, improving our ability to detect and visualize important small scale structures in subsurface.

6.2 Outlook

The previous presented work on the full-waveform inversion of crosshole GPR data triggered the following ideas for further improvements and possible future applications for this technique. There are two main points on which further investigations could be based: theoretical algorithm developments and application of the full-waveform inversion.

6.2.1 Theoretical development

For the effective source wavelet estimation, a least squares approach was used which assumes a point source with a wavelet that is the same for the entire domain. The estimation of an effective source wavelet for different areas, where the medium parameters and corresponding coupling can be different, would be an improvement. Furthermore, instead of assuming a point source, finite length antennas could be implemented (Streich, 2007b) to consider the real dimensions of the used antennas. In Chapter 3, we demonstrated the sensitivity of the effective source wavelet estimation by using either the starting models and a single correction of the wavelet (Part B in Fig. 2.2), or, by applying a second correction after a certain number of iterations of the full-waveform inversion (Part C in Fig. 2.2). Up to now this second correction was done manually and no rule of thumb

could be found after which number of iterations this should be applied. Here, further investigations are necessary.

Another factor that probably influences the conductivity results is the 3D to 2D conversion of data. This transformation takes only the first arrival times and their amplitudes into account, while the influence on the late arrival high amplitude events caused by waveguides remain unclear. To avoid this additional transformation the existing code could be extended to 2.5D or 3D.

Further suggested theoretical development on the algorithm:

1. Normalizing the gradient for a better comparison of different models and datasets;

2. Estimating different step-length calculations and perturbation factors (Yang *et al.*, 2013);

3. Frequency hopping for experimental data (similar to Meles *et al.* (2011));

4. Combining the inversion of more than one plane or 3D time domain code with optimized acquisition setup;

5. Improving starting models (e.g. Monte Carlo search).

6.2.2 Experimental applications

The next step for the application of the full-waveform inversion is a combined inversion of the saturated and unsaturated domain. The algorithm is already implemented as outlined in Appendix B, but the data quality was insufficient and the spatial sampling was too sparse to obtain a good starting model and an effective source wavelet, and to reliably invert all the data. Therefore, its is suggested to measure a new dataset with a larger unsaturated zone which is acquired with a denser sampling rate for transmitter and receiver positions.

Another extension of the inversion code is the combined inversion of surface, saturated and unsaturated aquifer data; therefore, surface data and corresponding source wavelets need to be incorporated in the algorithm (the algorithm is already extended for this purpose). Again, a dataset that covers all these zones with a certain depth/ distance and denser sampling is needed. Additionally, high resolution time lapse measurements could help to gain more information about transport processes. Further applications of the crosshole GPR full-waveform inversion and amplitude analysis to new areas such as peat land and permafrost domains may be considered. Laboratory experiments or controlled studies with known medium parameters could also provide deeper understanding of the full-waveform inversion reliability.

Appendix A

Optimization of acquisition setup for crosshole GPR full-waveform inversion using checkerboard analysis [1]

Tomographic inversions of crosshole ground-penetrating radar provide images of electromagnetic properties of the shallow subsurface and are used in a wide range of applications. Whereas the resolutions of ray-based methods like first-arrival travel time and first-cycle amplitude tomography are limited to the scale of the first Fresnel zone, full-waveform inversions incorporate precise forward modeling using the full recorded signal for a solution of Maxwell Equations, which results in sub-wavelength resolutions. In practice, the method can be time-consuming in data acquisition and expensive in computational costs. To overcome these expenses, a semi-reciprocal acquisition setup with a reduced number of transmitters and an interchange of transmitter and receiver boreholes instead of a one-sided equidistant setup in either borehole yielded promising results. Here, this optimized, semi-reciprocal acquisition setup is compared to a dense, equidistant, one-sided acquisition setup measured at the field site Krauthausen, Germany. The full-waveform inversion results are evaluated using the checkerboard test as a capable resolution analysis tool to determine resolvabilities. We introduced also a new method of time-zero correction by a cross-correlation of a zero-offset profile with corresponding horizontal traces of each multi-offset gather. The obtained experimental results from Krauthausen combined with the checkerboard analysis indicate the main three permittivity layers that correspond with

different porosities. Also fine-layered structures within these main layers were reliably imaged. We conclude that the use of the semi-reciprocal setup is optimum for acquisition speed, inversion speed and obtained permittivity inversion results. Our results indicate that conductivity results are better for denser transmitter-receiver setups.

A.1   Investigated measurement setups

As a rule of thumb, the spatial resolution of ray-based inversions scales with the diameter of the first Fresnel-zone, whereas the full-waveform inversion provides a resolution in the order of sub wavelength (Dickens, 1994; Dessa & Pascal, 2003). Full-waveform inversions are more expensive in computational cost, which is highly influenced by the number of transmitters. Therefore, Klotzsche *et al.* (2010) used an optimized, semi-reciprocal acquisition setup with a reduced number of transmitters and a large number of receivers instead of a one-sided setup with equal transmitter and receiver spacings in either borehole as shown in Figure A.1, thus reducing the acquisition and computational effort but maintaining a high resolution of the subsurface. The resulting low ray-coverage close to the transmitter borehole was increased by an interchange of transmitter and receiver boreholes.

To investigate the reliability and resolution of tomographic images for different acquisition setups and inversion methods, a formal resolution analysis can be carried out (Menke, 1989; Maurer *et al.*, 2009). However, gradient-based methods do not explicitly compute the Jacobian matrix, which is needed to calculate permittivity and conductivity sensitivity functions (Meles *et al.*, 2012). Alternatively, one can use checkerboard tests that are commonly used in a wide range of seismic tomographic inversion applications to determine resolvabilities. Zelt & Barton (1998) inverted 3D refraction travel times recorded in the Faeroe Basin in a study area of 44 km x 26 km size and used detailed checkerboard tests on several depth slices of the 3D seismic refraction tomograms to assess the lateral resolution (Zelt, 1998). Several other studies (Day, 2001; Morgan *et al.*, 2002) adapted the procedure of Zelt (1998) and applied it to 3D seismic refraction data. Rao *et al.* (2006) performed the checkerboard test to verify a full-waveform tomography of experimental crosshole seismic data.

In this study, we apply the checkerboard analysis on full-waveform inversion results for a dense, equidistant, one-sided acquisition setup, an optimized, semi-reciprocal setup and a sparse, one-sided acquisition setup to investigate the obtained permittivity and conductivity resolution and the optimal acquisition setup. First, we give an overview of the full-waveform inversion algorithm. Then, we discuss the resolution analysis, which is carried out by a checkerboard test. Finally, we apply the full-waveform inversion and the
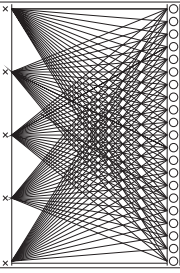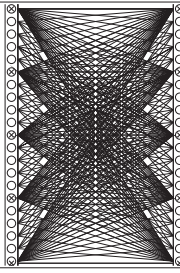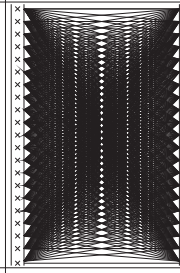
Setup	a) sparse	b) semi-reciprocal	c) dense
Scheme			
Trn.-spacing	0.5 m	0.5 m	0.1 m
Rec.-spacing	0.1 m	0.1 m	0.1 m

Figure A.1: Schematic acquisition setups with different spatial samplings of transmitters. Transmitters are indicated by crosses, receivers by circles. a) A sparse, one-sided setup with spatial samplings of 0.5 m and 0.1 m for transmitters and receivers, respectively (note the gaps in ray-coverage). b) Equals a) but additionally includes interchanged transmitters and receivers (semi-reciprocal) that improve the ray-coverage close to the transmitter borehole. c) A dense, one-sided, equidistant setup with spatial samplings of 0.1 m for transmitters and receivers, respectively. Note that mainly the number of transmitters determines the acquisition effort and computational costs.

checkerboard test to a data set recorded at the Krauthausen test site and evaluate the reliability and resolution for the different acquisition setups.

A.2   Full-waveform inversion

The full-waveform inversion algorithm after Ernst (2007) and Meles *et al.* (2010) is based on the approach of Tarantola (1984a,b, 1986) and uses a conjugate-gradient method. It involves precise forward modeling of the electromagnetic wave field through a 2D FDTD solution of Maxwells Equations. An essential requirement for the modeling is to find appropriate permittivity and conductivity starting models, $\varepsilon = \varepsilon_{ini}$ and $\sigma = \sigma_{ini}$, which are then iteratively updated in the direction of the corresponding gradient of a misfit function. The misfit or objective function is defined as the summation over the number of transmitters and receivers and the observation time of the residual wave field $\triangle \mathbf{E}^S$, which is obtained by a subtraction of the synthetic field $\triangle \mathbf{E}^S_{syn,z}$, from the observed wave field $\triangle \mathbf{E}^S_{obs,z}$. The gradient at each point in the model is calculated using a zero-lag cross-correlation of the synthetic wave field with a back propagation of the residual wave field

from all receivers towards the corresponding transmitters. Two additional FDTD forward models are needed to calculate how far the medium properties are updated towards the gradient direction. The inversion algorithm is MPI parallelized. Therefore, one slave CPU per transmitter is used to carry out the four forward modeling calculations involved in each iteration. Additionally, one master CPU is used for data organization and gathering of gradients and updated models.

Convergence of the inversion is reached if the change in the root mean square error of the residual wave field $\triangle \mathbf{E}^S$, referred to as trace RMS ($TRMS$), falls below 1%. We define the $TRMS$ for N_s transmitters, N_r receivers and the number of time samples N_e as

$$TRMS = \sqrt{\frac{\sum_{s=1,d=1,e=1}^{N_s,N_d,N_e}(\triangle E^{s,d,e})}{N_s \cdot N_d \cdot N_e}}. \tag{A.1}$$

A small $TRMS$ indicates a good fitting of the synthetic data and the observed measured data. Note that a small $TRMS$ does not necessarily imply a good reconstruction of the permittivity and conductivity distributions, since ray-coverage also plays an important role.

A.3   Resolution analysis

According to Zelt (1998) and Rao *et al.* (2006), the checkerboard test can be summarized as shown by the workflow in Figure A.2 using the convention for variables in Table A.1. In addition to the common checkerboard analysis for velocity tomograms, or permittivity tomograms for GPR, here we will also apply the checkerboard analysis on the obtained conductivity images, which depend both on the permittivity and the amplitude information of the traces. Firstly, the final result of the full-waveform inversion $\{\varepsilon, \sigma\}$ (Fig. A.2, step A) is superimposed by perturbation patterns $\{\triangle\varepsilon, \triangle\sigma\}$ (Fig. A.2, step B) to obtain a perturbed model $\{\varepsilon, \sigma\}_p$ (Fig. A.2, step C):

$$\{\varepsilon, \sigma\}_p = \{\varepsilon, \sigma\} + \{\triangle\varepsilon, \triangle\sigma\}, \tag{A.2}$$

where the perturbation patterns are defined as follows:

$$\{\triangle\varepsilon, \triangle\sigma\} = -C(x, z) \cdot m^p_{\{\varepsilon,\sigma\}} \cdot \{\varepsilon, \sigma\}_{mean}. \tag{A.3}$$

$\mathbf{C}$(x,z) is the checkerboard matrix consisting in rows and columns of alternating positive and negative patterns of ± 1 with a defined pattern size and $m^p_{\{\varepsilon,\sigma\}}$ is a parameter for the magnitude of perturbation. Thus, the perturbations are applied as a percentage of the background permittivity and conductivity distributions according to Zelt (1998).
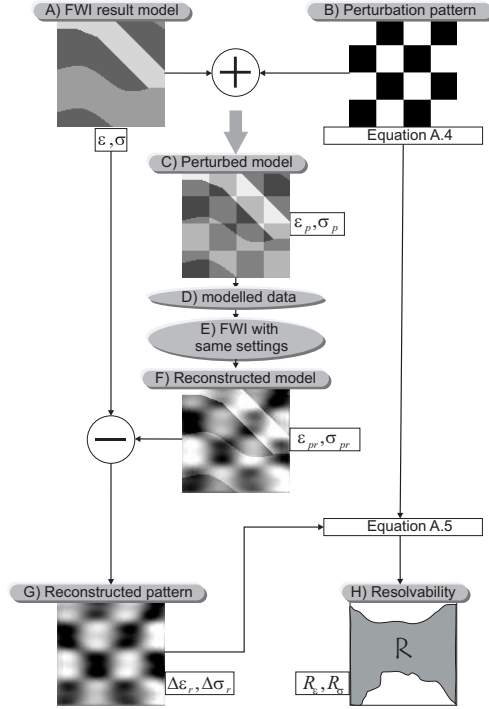
Figure A.2: Flow chart of checkerboard analysis. A) An inverted model is superimposed by B) a perturbation pattern resulting in C) a perturbed model, for which D) synthetic data are modeled, followed by E) full-waveform inversion to obtain F) a reconstruction of the perturbed model. After subtracting F) from the input model A), the reconstructed pattern G) is compared to the original pattern B) with a semblance approach to provide H) resolvability matrices.

From the superimposed, perturbed model, a synthetic data set is modeled using the same FDTD code (Fig. A.2, step D), which is then inverted using the same method, procedure, constraints and parametrization as used for the initial full-waveform inversion of the experimental data (Fig. A.2, step E). To reconstruct only the perturbations, the initial full-waveform inversion result (without the perturbation pattern) is used as a starting model for the perturbed data. A subtraction of the reconstructed perturbed model $\{\varepsilon_{pr}, \sigma_{pr}\}$ (Fig. A.2, step F) from the initial full-waveform result yields the reconstruction of the perturbation pattern $\{\triangle\varepsilon_r, \triangle\sigma_r\}$ (Fig. A.2, step G):

$$\{\triangle\varepsilon_r, \triangle\sigma_r\} = \{\varepsilon, \sigma\} - \{\varepsilon_{pr}, \sigma_{pr}\} \tag{A.4}$$

The resolvability compares the recovered and original perturbation patterns and provides

Table A.1: Variables and denotation convention for the methodology of the checkerboard test.

Variables for ε	Variables for σ	Describtion
ε	σ	Final model from inversion
$\mathbf{C}$(x,z)	$\mathbf{C}$(x,z)	Checkerboard matrix of alternating pattern of ± 1
m_ε^p	m_σ^p	Parameter of perturbation magnitude
ε_p	σ_p	Perturbed (checkerboard) model
$\triangle\varepsilon$	$\triangle\sigma$	Perturbation anomaly pattern
ε_{pr}	σ_{pr}	Reconstruction of perturbed model
$\triangle\varepsilon_r$	$\triangle\sigma_r$	Reconstruction of perturbation anomaly pattern

good information about the ability of a particular inversion to resolve the model. Zelt (1998) introduced the concept of a semblance between the exact and the recovered checkerboard anomalies over a square patch with M cells. This similarity approach indicates the ability of the data or inversion to resolve features and is defined in terms of resolvability $\mathbf{R}_{\{\varepsilon,\sigma\}}$ as

$$\mathbf{R}_{\{\varepsilon,\sigma\}} = \frac{\sum_{i=0}^{M}(\triangle\{\varepsilon,\sigma\}_{r,i} + \triangle\{\varepsilon,\sigma\}_i)^2}{2 \cdot \sum_{i=0}^{M}(\triangle\{\varepsilon,\sigma\}_{r,i}^2 + \triangle\{\varepsilon,\sigma\}_i^2)}, \tag{A.5}$$

where values of 1.0 correspond to perfect resolvability (Fig. A.22, step H). Both Zelt (1998) and Rao *et al.* (2006) indicated resolvabilities above a threshold of 0.7 as well-recovered checkerboard structures and fore well-resolved regions of the final inverted model. The size of the patch consisting in M cells, over which the semblance is calculated, should be, on the one hand, large enough to be relatively insensitive to noise and on the other hand, small enough to represent a local measure. As a compromise we chose the checkerboard pattern size for the size of the patch. The resolvability represents the ability to resolve features of the size of the checkerboard pattern. The checkerboard tests can be carried out for a series of checkerboard pattern sizes in the range of interest of resolution lengths to assess in detail the size of resolvable features. It is expected and has been shown by several authors (Zelt, 1998; Morgan *et al.*, 2002; Rao *et al.*, 2006) that the resolvability reflects the ray-coverage.

A.4   Experimental study

A.4.1   Test site

The Krauthausen test site, Germany, located 10 km south-west of the city of Düren, was setup by the Forschungszentrum Jülich in 1993 to perform experiments on water flow and solute transport processes (Tillmann A., 2005). The 200 m x 70 m, grass-covered test site lies in the Lower Rhine Embayment (Vereecken *et al.*, 2000), which is characterized by a multi-layer aquifer. Most of the studies at the Krauthausen test site were carried out in a near-surface aquifer from 2 m 11 m depth (Tillmann A., 2005). In total, 75 observation wells were installed with a pipe diameter of 50 mm. A conceptual cross-section of the uppermost aquifer derived from field studies from the borehole profiles presented from Englert (2003) is shown in Figure A.3. These geologic profiles were confirmed by Tillmann *et al.* (2008) using cone-penetration tests and measuring the natural gamma activity and electrical resistivity. According to the petro-physical log details of the uppermost aquifer (Vereecken *et al.*, 2000; Tillmann A., 2005), the uppermost aquifer can be divided into three main layers by means of samples of four drillings. The approximately 9 m thick aquifer is overlaid by flood plain deposits and the basis is formed by alternating thin clay and silt layers Englert (2003). Within the aquifer, upper and lower layers of medium gravel and a middle layer consisting of medium sand and fine gravel were found. Clay and silt contents of the aquifer vary between 0.5% - 7.5% and the mean total porosity is 26% $\pm$ 7% (Vereecken *et al.*, 2000). In this study, only the saturated zone below 2 m depth is considered.

A.4.2   Data acquisition

Two data sets were acquired in May 2011 in the northern part of the Krauthausen test site using two boreholes with a separation of 4 m. In the following, they will be referred to as borehole east and borehole west. A pulseEKKO system with 200 MHz antennas and a source voltage of 200 V was used. Two series of multi-offset gathers (MOG) are acquired, where the transmitter is fixed at a discrete series of locations in one borehole, while the receiver is in each case lowered down in a second borehole to record a MOG. A dense data set of a series of 94 MOGs with transmitters in borehole east and 0.1 m spatial sampling of receivers in borehole west, was recorded on the first day. On the second day, a sparse data set of a series of 19 MOGs was recorded with 0.5 m spaced transmitters located in borehole west and 0.1 m spaced receivers in borehole east. The two data sets could be combined to obtain a semi-reciprocal data set. After every 10 MOG measurements, a common midpoint (CMP) gather was recorded in air and at the end of each day a zero-
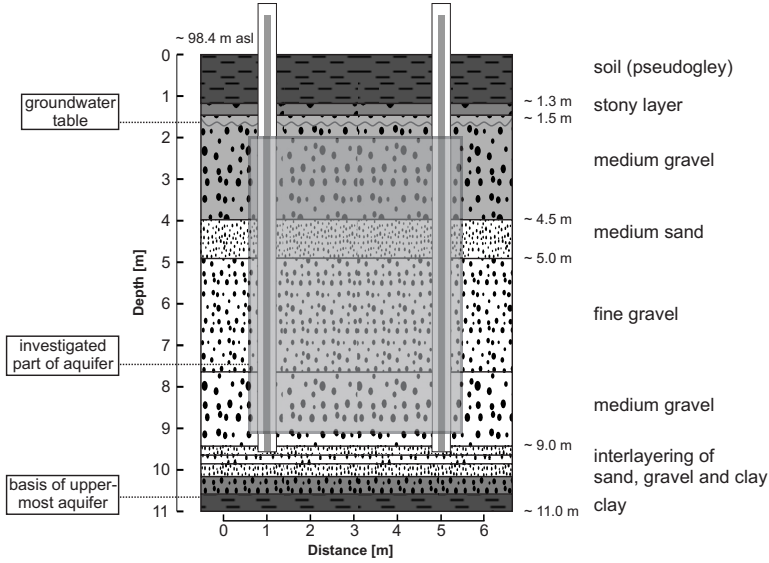
Figure A.3: Generalized stratigraphy of the investigated uppermost aquifer at the Krauthausen test site after Englert (2003). The surface is 98.4 m above sea level and the groundwater table varies seasonally from 2.5 m depth in summer to 1 m depth in winter. The dashed box indicates the investigated part of the aquifer from 2 m - 9 m. Here, three main layers are identified: an uppermost layer of medium gravel, a middle layer of medium sand and fine gravel and a lowermost layer of medium gravel, correlated with low, high and low porosities, respectively (Vereecken *et al.*, 2000).

offset profile (ZOP) was recorded by lowering down transmitter and receiver antennas in parallel with a spacing of 0.1 m in boreholes west and east, respectively. Note that we did not consider the unsaturated zone of the aquifer and use only transmitter and receivers below 2.7 m to prevent undesired effects due to water reflections and refractions close to the water table at 2.5 m depth (Klotzsche *et al.*, 2010).

A.4.3   Time-zero correction

An essential step in the preprocessing of GPR data is to determine an accurate time- zero position of the radar signal. In the majority of cases, time-shifts or jumps of the time zero are caused by thermal drift, electronic instability, cable length differences and variations in antenna coupling (Cassidy, 2009). The absolute time zero t_0^{abs} of the signal is defined

in air by

$$t_0^{abs} = t^{fb} - \left(\frac{x^s - x^r}{c_0} \right), \tag{A.6}$$

where x^s and x^r are the lateral positions of the transmitter and receiver boreholes, respectively and tfb the first break time.

A common method to determine time-zero shifts is to record a CMP measurement after several MOG measurements, determine the absolute time zero, followed by an interpolation to obtain an individual time zero for all MOGs in the data set. Here we propose an improved and time-saving time-zero correction method based on a ZOP-MOG cross-correlation method: 1) A ZOP measurement is time-zero corrected using a subsequently measured CMP in air. 2) Each measured MOG contains one trace where the wave has traveled the same path as one trace in the ZOP. Assuming that no time- shift occurs during the ZOP and CMP measurements and only time-shifts occur during the MOG measurements, these two traces can be cross-correlated, where the maximum correlation indicates the relative time-shift that occurred in the MOG gather that can be compensated accordingly. The cross-correlation of the z-component of the electric field between two corresponding traces i is given by

$$(E_{z,i}^{ZOP} * E_{z,i}^{MOG})(\tau) = \sum_{-\infty}^{\infty} E_{z,i}^{ZOP}(t) \cdot E_{z,i}^{MOG}(t + \tau) dt, \tag{A.7}$$

and provides information about the similarity, repeatability and also about the suitability of the trace to determine the time-zero shift. The time-lag τ of the maximum of the cross-correlation is the relative time-zero shift. The cross-correlation is normalized by the autocorrelation of the ZOP and MOG at zero-lag. Figure A.4 shows the maxima of the cross-correlations and the time-zero shifts resulting from the ZOP-MOG cross-correlation method and from the CMP method, where red circles mark the calculated CMP time zeros. As Figure A.4a shows, the maximum of the cross-correlation is above 0.98 for all traces in the saturated zone but there is a significant reduction with lower values in the unsaturated zone. This implies a good similarity and repeatability of shape and amplitude of the traces of the MOG and the corresponding ZOP traces in the saturated zone.

Figure A.4b is a plot of both the absolute time zero determined from CMPs in air (dashed line) and the relative time-zero shifts from cross-correlations with ZOPs (solid line), added to the absolute time zero of the reference to be comparable to the CMP method, for the dense acquisition setup. In principle, there is a high agreement of the time zeros. As expected from the weak cross-correlations, the time zero from ZOP deviates more strongly from the measured CMP time zero in the unsaturated zone. Note the large time jump after trace 88 related to a change of transmitter battery. In-between the CMP measurements, the correlation results seem to do a better job than the interpolation. To

ensure the correctness of the reference t_0^{abs} of the ZOP, it is recommended to perform several CMPs at the end of the survey and take the average of the obtained time zeros. We applied T0-correction with the time zero from the ZOP for all acquisition setups with a smoothing to neglect small outliers like traces 40, 43, 73 and 86 in the dense setup. We can conclude that the ZOP-MOG cross-correlation method is suitable to determine the relative time zero for the saturated zone. This methodology is better than the conventional interpolation between known absolute time zeros from CMPs, since for each MOG an individual time zero is obtained.
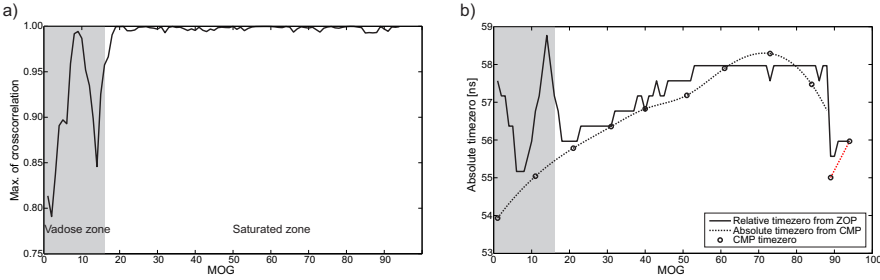
Figure A.4: Comparison of methods to determine the time-zero correction. a) Maximum of cross-correlations between ZOP traces and corresponding MOG traces. b) Absolute time zeros resulting from the cross-correlation with ZOP (blue) and from the CMP measurements (red) for each horizontal trace according to each MOG d) - f) Red circles indicate where the time zero is calibrated with the absolute time zero from the CMP. The relative time- zero shifts are converted into absolute values by adding them to the reference time zero corresponding to the ZOP. The gray background indicates the unsaturated zone. Note the large time jump after trace 88 related to a change of transmitter battery.

A.4.4 Starting model

The results of the ray-based inversion of first arrival travel times (Vidale, 1990) and first-cycle amplitudes (Maurer & Musil, 2004) are used as starting models for the full-waveform inversion. For the ray-based inversion, a wide range of different homogeneous start velocity models were tested and the smallest RMS after 30 iterations and the least diagonal artefacts were found for a constant velocity of 0.075 m/ns for the sparse acquisition setup, 0.069 m/ns for the semi-reciprocal setup and 0.065 m/ns for the dense setup. The inversion of the picked first arrival travel times and first-cycle amplitudes with these parameters and a subsequent conversion of velocity and attenuation into permittivity and conductivity led to the tomograms shown in Figure A.5 for the three acquisition setups.

Three layers are recovered: layer 1 in 23.5 m depth with a mean relative permittivity of $\varepsilon_{r;mean} = 15.0$ and a mean conductivity of $\sigma_{r;mean} = 27$ mS/m, layer 2 in 3.56.5 m depth with $\varepsilon_{r;mean} = 18.0$ and $\sigma_{r;mean} = 29$ mS/m and layer 3 in 6.59 m depth with $\varepsilon_{r;mean} = 15.0$ and $\sigma_{r;mean} = 27$ mS/m. Figures A.5c, f and i show the ray-coverage after travel time inversion, which is densest for the dense setup with the largest number of traces. According to the principle of semi-reciprocal measurements shown in Figure A.1b, the semi-reciprocal setup exhibits a dense ray-coverage close to both boreholes, whereas the sparse setup is not well covered with ray-paths close to the transmitter borehole. All three setups show a sparser ray-coverage in the upper and lower parts. This effect is more prominent for sparser acquisition setups. We used the permittivity distribution from the semi-reciprocal setup (Fig. A.5d) and for stability of the inversion a homogeneous conductivity model of 26 mS/m according to the mean conductivity of the distribution from Figure A.5e as starting models for the full-waveform inversion.

A.4.5   Full-waveform inversion results

Using the obtained ray-based inversions as permittivity and conductivity start models, the full-waveform inversion is performed following the approach of Meles *et al.* (2010). After applying a 3D to 2D conversion to correct 3D effects in the real data for the 2D FDTD modeling code, the source wavelets for each of the three addressed acquisition setups are estimated following the approach of Ernst *et al.* (2007b), which was extensively tested on measured data by Klotzsche *et al.* (2010). The shapes and amplitudes of the corrected wavelets are similar for all three setups.

For all setups, the convergence criterion of a change in TRMS smaller than 1% is reached after 16 iterations, where the TRMS at all setups decreases to 40% compared to the starting model. The TRMS of the sparse setup is $1.2916 \cdot 10^{-6}$ larger than the $TRMS$ of the semi-reciprocal ($1.1160 \cdot 10^{-6}$) setup but smaller than the dense ($1.3225 \cdot 10^{-6}$) setup, which is probably caused by the significantly increased number of traces that needs to be fitted. However, note that a small TRMS does not necessarily imply a good model resolution. Note that we observed a 4 % - 7% smaller TRMS by using the ZOP - MOG cross-correlation method instead of the CMP method to determine the time zero, which indicates that our novel time-zero correction improves the inversion results.

Figure A.6 shows the obtained permittivity and conductivity distributions. In addition to the three main layers of permittivity and conductivity indicated already by the ray-based inversion results, the permittivity middle layer shows finer sub-layers of alternating slightly higher and lower permittivities. In addition, significant differences are noticeable in the upper- and lowermost layer of the aquifer in 2 m - 3.5 m and 7 m - 9 m depths. Note

that accurate borehole deviation information was indispensable and artefacts occurred when uncorrected coordinates were used (see also Maurer & Green (1997)).

The conductivity results show more differences between the different acquisition setups. Again, like in the permittivity distribution, the middle layer is best resolved and most similar between the acquisition setups. In the upper part of this layer at about 4 m depth, a high-conductivity anomaly is present close to borehole east, which is most clear with the dense setup. With decreasing number of transmitters and receivers, the conductivity models appear to be smoother and fewer anomalies are resolved. The sparse setup does not resolve every layer that is distinguishable in the tomogram of the semi-reciprocal setup. In the upper region more conductivity structures and a stronger heterogeneity appear for the dense setup. In general, the sharpness of the conductivity layer interfaces differs between the acquisition setups, where the differences for the permittivity results are rather small, especially in the middle layer. For fewer transmitters the conductivity models are smoother and a finer layering is only resolved with the dense setup. In the following, we want to clarify which parts of the aquifer are most reliably resolved.
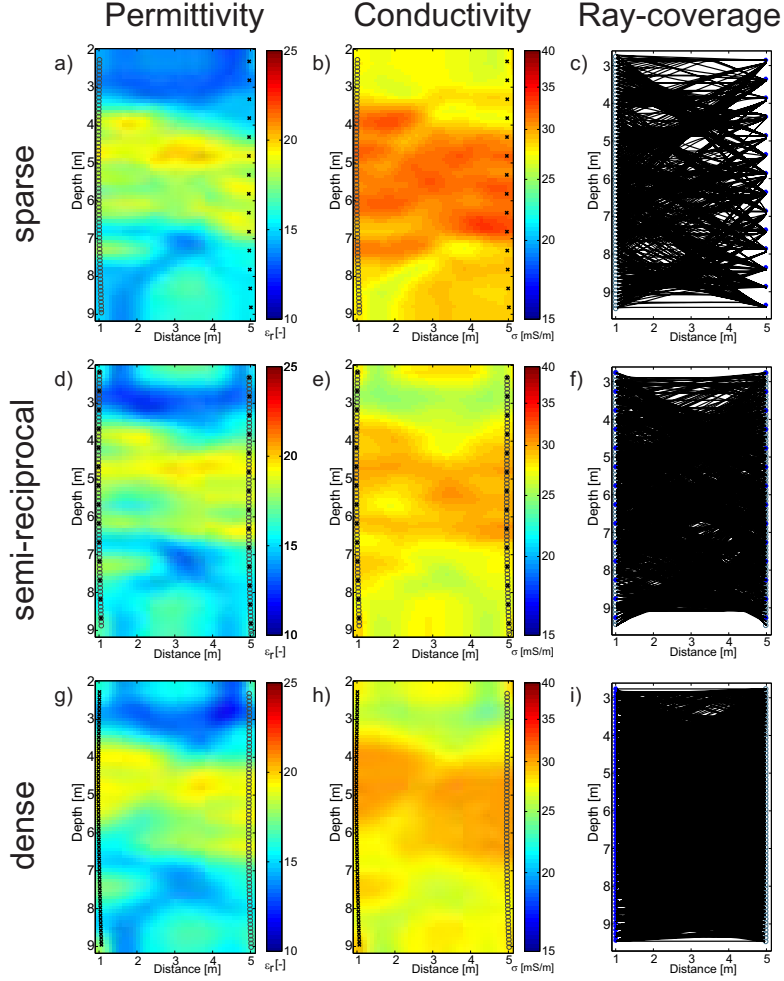
Figure A.5: Ray-based inversion results, where a), b) and c) show the permittivity distribution, conductivity distribution and ray-coverage of the sparse setup, respectively. d), e) and f) show the permittivity distribution, conductivity distribution and ray-coverage of the semi-reciprocal and g), h) and i) of the dense setup, respectively.
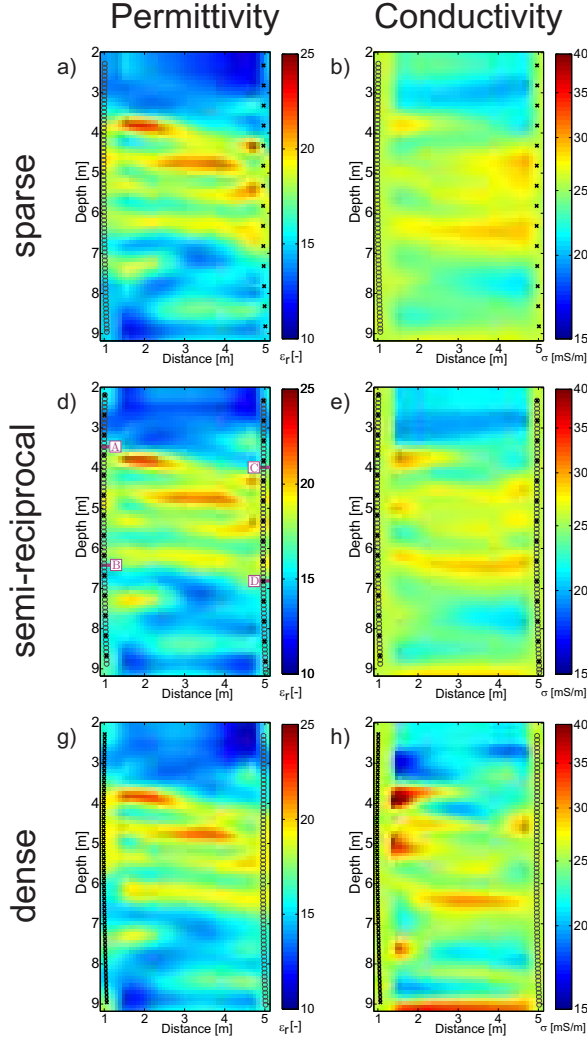
Figure A.6: Full-waveform inversion results, where a), b) and c) show the permittivity and d), e) and f) the conductivity distributions after 25 iterations for the sparse, semi-reciprocal and dense acquisition setups, showing an improved resolution compared to the ray-based results shown in Figure A.4.

A.4.6   Comparison of observed and modeled traces

Figure A.7 compares the observed traces with the modeled traces of transmitters 1 - 14 in borehole east after 16 iterations. In general, the modeled data show similar trends as the observed data and also the order of magnitude of the amplitudes is consistent. The shape of the traces is analogical for the modeled and observed data for all shown transmitters and all transmitters not shown. In general the phases of the modeled data fit the phases of the observed data well. Differences in the travel times can be directly related to heterogeneities in the permittivity model and conditionally also in the conductivity model since conductivity depends on both the velocity and the amplitudes of the signals.
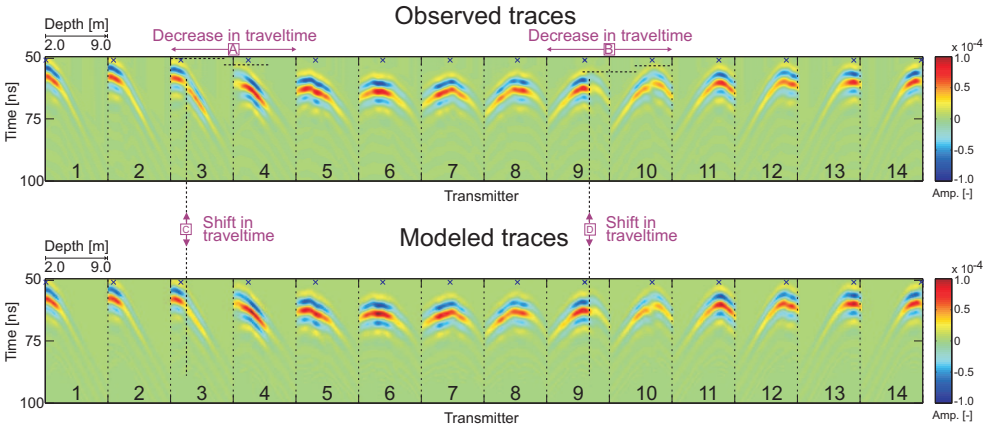
Figure A.7: Comparison of the observed traces and the modeled traces after 16 iterations for transmitters 1 - 14 and depths 2 m - 9 m (see Transmitter 1). Transmitters 1 - 14 are present at depths 2 m, 2.5 m, ... , 8.5 m, as indicated by the crosses. According to A and B in the inversion results in Figure A.5, the increase and decrease in overall MOG travel times between transmitters 3 - 4 and 9 - 10, indicated by the horizontal dashed lines and according to C and D in Figure A.5, the shift in travel time in MOGs 3 and 9, indicated by vertical dashed lines, correspond to the transitions between the three main layers shown in Figure A.2.

The transition from low permittivity and low conductivity above 4.5 m to higher values below 5.0 m is characterized by a decrease of velocity and thus an increase in permittivity. With respect to the decreased velocity we expect longer travel times at transmitter 4 compared to 3. This is indeed confirmed by the observed data (see A in Figs A.6 and A.7). Transmitter 3 shows a shift in travel time at receiver 18, which fits the increase in permittivity also very well (C in Figs A.6 and A.7). Transmitters 4 - 9 (borehole east) and

111

receivers 18 - 47 (borehole west) are located in the middle-high permittivity region. Slight fluctuations of the travel times of the data for these transmitters indicate the alternating higher and lower permittivity sub-layers. The transition from high permittivity and high conductivity to lower values is characterized by a clear decrease in travel time between transmitters 9 10 (B in Figs A.6 and A.7). A shift from longer to shorter travel times is, according to this, noticeable at transmitters 9 and 24 (D in Figs A.6 and A.7). The observed travel times but also the amplitudes of the traces are well fitted by the modeled data. In general, it is more difficult to fit the amplitudes compared to travel times and since the attenuation of amplitudes determines conductivity, the conductivity models are expected to be less accurate as permittivity models.

A.4.7   Resolution analysis using the checkerboard test

The differences in achieved resolution between the acquisition setups and between permittivity and conductivity are quantitatively investigated using the checkerboard test. One of the main challenges in the checkerboard test to achieve optimal quantitative and comparative values is to choose adequate pattern sizes and percentages of the perturbation of both the permittivity and conductivity distributions. With an average center frequency of 87.5 MHz and a mean permittivity of $\varepsilon_r = 16$, the dominant wavelength is about λ = 0.86 m. Additional synthetic studies (not shown) showed that a checkerboard pattern size of one wavelength encompasses the resolution range of interest.

In our study, the permittivity and conductivity parameters $m^p_{\{\varepsilon\sigma\}}$ are kept constant on optimized values and the tests are carried out for permittivity and conductivity separately to avoid falsified resolvabilities due to mutual interaction. Zelt & Barton (1998) and Rao et $al.$ (2006) found a perturbation magnitude of 5% for velocity suitable, which corresponds to a permittivity perturbation of $m^p_\varepsilon = 0.108$. Elaborate testing showed that this perturbation is well balanced. High-conductivity perturbations are needed to superimpose the model according to high-conductivity variability. However, it was found by extensive tests on synthetic data sets to be most effective to use a conductivity perturbation value of $m^p_\sigma = 0.6$.

The explained methodology is separately performed for permittivity and conductivity to obtain the reconstruction of the perturbation pattern for both, independently, as shown in Figure A.8. For both, permittivity and conductivity, the perturbation pattern is best reconstructed between 3.5 m - 6.5 m depth, clearly related to the high permittivity and high-conductivity layer. As also observed in synthetic studies, horizontal interfaces are sharper resolved than vertical interfaces. The permittivity perturbation pattern is better reconstructed for the dense and the semi-reciprocal setups than for the sparse setup. For

conductivity, the amplitude of the perturbation pattern increases for reducing numbers of transmitters.

The permittivity resolvability is better than the conductivity resolvability and demonstrates similar images for the dense and semi-reciprocal setups. In contrast to these two setups, the sparse setup shows worse resolvabilities, which is confirmed by a worse mean permittivity resolvability value, as listed in Table A.2. A similar situation is given for the conductivity, where the resolvabilities are stepwise better for denser setups. This is reflected by better mean resolvabilities, which seem to be interrelated with the number of involved transmitters. Note that in the sparse setup 14 transmitters, in the semi-reciprocal setup 28 transmitters and in the dense setup 68 transmitters are involved, which gives rise to differences in acquisition time and the number of required CPUs. Note that the mean permittivity resolvability is above the threshold of 0.7 for a well-resolved model, whereas the mean conductivity resolvability is slightly below this threshold.

Table A.2: Resolvability of permittivity and conductivity for the sparse, semi-reciprocal and dense acquisition setups. For a comparison, the approximate acquisition time and the number of CPUs required for the full-waveform inversion process is about 40 minutes.

Acquisition setup	Mean resolvability of ε	Mean resolvability of σ	Approximate acquisition time	Number of CPUs
sparse	0.72723	0.64833	2.5 hours	14
semi-reciprocal	0.74531	0.66462	4.5 hours	28
dense	0.74329	0.68394	9 hours	68

The resolvabilities are expected to be strongly related to the ray-coverage. Comparing the resolvabilities with the ray-coverage from the ray-based inversions shown in Figures A.5c, f and i the upper and lower regions of all resolvability images show lower values for R^2 and R^2, which is connected to the reduced ray-coverage in these regions. This is consistent with the inversion results in Figure A.6, where the middle part of the aquifer was well resolved and the upper and lower regions less resolved. The permittivity and conductivity resolvabilities for the sparse acquisition setup show low values close to borehole west, even if they are still above the threshold of 0.7 for permittivity and therefore, considered to be well-resolved. The discrepancy between the resolvabilities close to borehole east and borehole west are directly associated with the reduced ray-coverage due to a large transmitter spacing in borehole west. Figure A.5i displays the weak ray-coverage close to the borehole with the sparse transmitters. In contrast, the semi-reciprocal and dense setups provide higher resolvabilities due to a denser ray-coverage. Whereas with

the dense acquisition setup the dense ray-coverage is obtained by a dense transmitter configuration, a similarly dense ray-coverage is achieved with the semi-reciprocal setup by placing transmitters with a larger spacing in both boreholes. This results in high-permittivity resolvabilities above 0.8 and also high-conductivity resolvabilities above 0.7 close to both boreholes for these two acquisition setups.

Although the reconstruction of the conductivity patterns appears to be sharp, this is caused by the much larger conductivity perturbation magnitude. Figure A.9 indicates much better permittivity resolvability, which is consistent to synthetic studies and what we expected from the inversion results themselves. Note that the resolvability reflects how good the pattern was reconstructed compared to the original conductivity pattern. Due to different magnitudes of perturbation, the reconstructed permittivity pattern cannot be directly compared to the reconstructed conductivity pattern, whereas the resolvability can be directly compared.
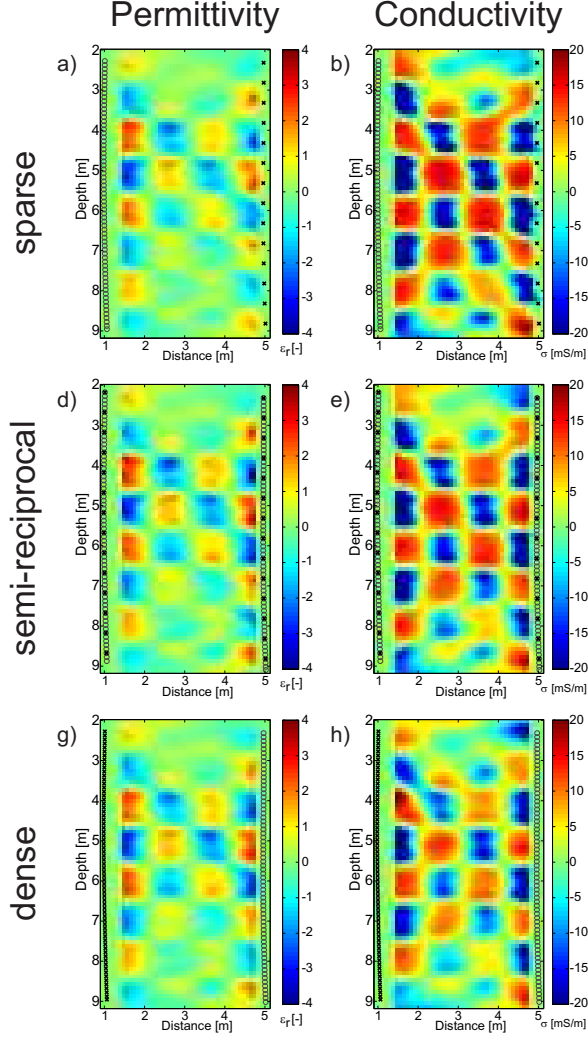
Figure A.8: Reconstruction of the permittivity and conductivity perturbation pattern for the sparse, semi-reciprocal and dense full-waveform inversion results shown in Figure A.5 using the checkerboard analysis shown in Figure A.2. A checkerboard pattern size of one wavelength and perturbation magnitudes of $m_\varepsilon^p = 0.108$ for permittivity and $m_\sigma^p = 0.6$ for conductivity are used.
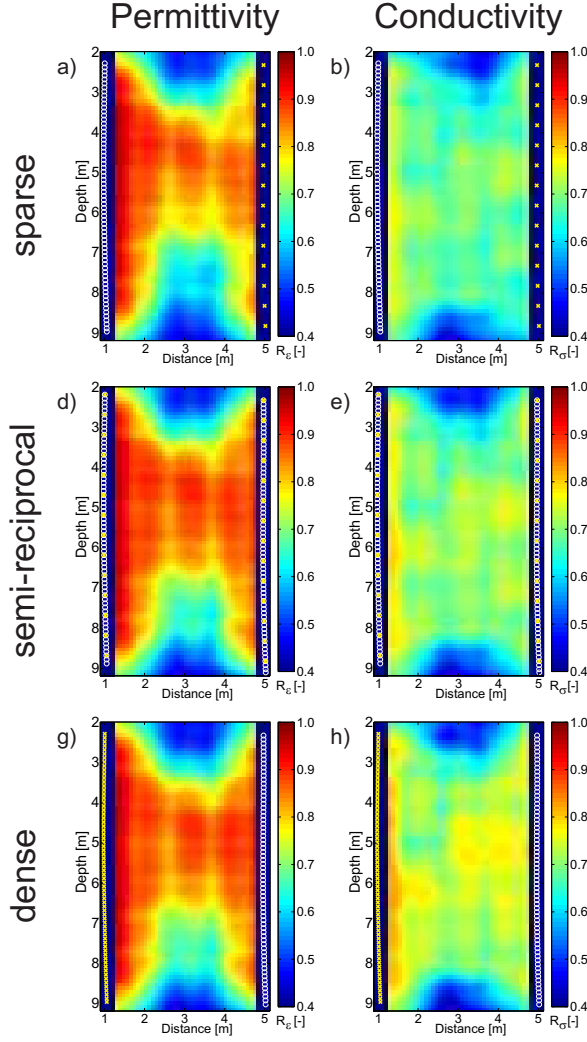
Figure A.9: Permittivity and conductivity resolvability for the sparse, semi-reciprocal and dense full-waveform inversion results shown in Figure A.5, obtained using the checkerboard analysis shown in Figure A.2.

A.4.8 Interpretation of permittivity and conductivity results

Based on the results of the reliability of certain regions in the models, Figure A.10 shows the interpreted permittivity model of the semi-reciprocal results with regard to the generalized stratigraphy introduced above. Changes in travel times in the observed data support the subdivision of the studied aquifer into three main layers. The shapes, phases and also amplitudes are well fitted by the modeled data, so we can assume that the permittivity and conductivity models are reliable. In 2 m - 3.5 m depth, a layer of low permittivity is distinguishable. The mean relative permittivity of $\varepsilon_{r,mean} = 14.1$ can be related to the medium gravel in the generalized soil texture. The high-permittivity layer in 3.5 m 6.5 m depth shows alternating horizontal sub-layers of slightly higher and lower permittivities. With regard to the resolution analysis the resolution of the middle layer is most reliable and we can have confidence in the detection of fine sub-layering. This can be explained by depositional sequences of the fluvial sediments with finer and coarser materials. In further studies this hypothesis needs to be confirmed by a comparison with other data from the uppermost aquifer at the Krauthausen test site. The higher permittivity with $\varepsilon_{r,mean} = 18.1$ in this middle layer is in accordance with the finer material of medium sand and fine gravel. At 6.5 m depth a transition to lower permittivity with mean values of $\varepsilon_{r,mean} = 15.1$ is present. This matches the change to coarser material of medium gravel in this depth.

The permittivity model ε_r is converted into porosity Φ using the petrophysical model from Linde *et al.* (2006):

$$\Phi = \left(\frac{\varepsilon_{r;water} - \varepsilon_{r;matrix}}{\varepsilon_r - \varepsilon_{r;matrix}} \right)^{-\frac{1}{m}}. \tag{A.8}$$

Due to a similar geology of a gravel aquifer, we use the same parametrization as Doetsch *et al.* (2010b): (1) the relative permittivity of water at 10 °C $\varepsilon_{r,water} = 84$; (2) the relative permittivity of the matrix $\varepsilon_{r,matrix} = 8$; and (3) the cementation factor of $m = 1.6$. Here, a fixed cementation factor instead of a likely range as in the study of Doetsch *et al.* (2010b) is used. The vertical variability and even the quantitative values of porosity match site-specific information from the literature very well without applying any further calibration (Vereecken *et al.*, 2000). More research is needed for the determination and calibration of the petrophysical model parametrization for this test site.

The conductivity inversion results show a high-conductivity layer at 9 m depth, which is most visible with the best resolved conductivity model of the dense acquisition setup and corresponds to the clayey base of the aquifer, even though the checkerboard test indicated low resolution in this region. Altogether, the layering derived from the inversion fits the generalized stratigraphy of the test site well, even though the depths of the layer interfaces are not exactly the same as in the generalized stratigraphy model. Note, that
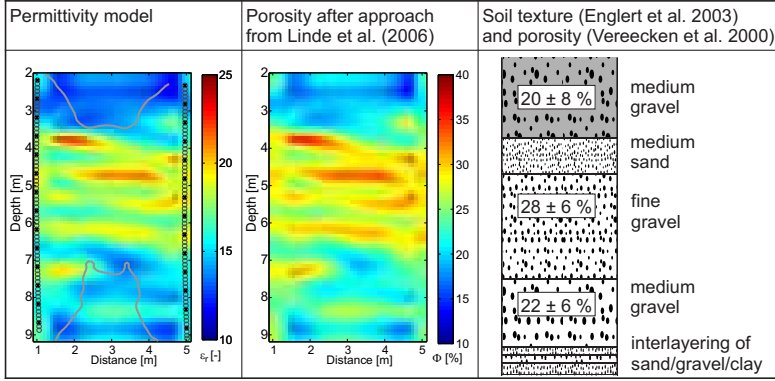
Figure A.10: Overall interpretation of semi-reciprocal permittivity inversion results. The gray line indicates the smoothed threshold of resolvability of 0.7, which separates less resolved regions in the upper and lower parts from well-resolved regions in the middle part. The middle layer, which resolves fine structures, is most reliable. Following the approach of Linde *et al.* (2006) and using the parameters of Doetsch *et al.* (2010b) the permittivity is converted into porosity. For a comparison the generalized soil texture after Englert (2003) and the porosity after Vereecken *et al.* (2000) of the Krauthausen test site are shown.

the uppermost and lowermost regions are less-resolved, indicated by the boundary of a resolvability threshold of 0.7 (indicated by gray lines).

A.5   Conclusions and outlook

Experimental data sets with sparse, semi-reciprocal and dense transmitter-receiver se-tups were acquired at the Krauthausen test site. The processing could be optimized by a novel method for time-zero correction, which improved the full-waveform inversion results. Here, a relative time-shift using a cross-correlation of horizontal ZOP traces with corre-sponding MOG traces was used. A comparison with the time zero obtained from CMP measurements confirmed that the cross-correlation method is reliable and more precise in the saturated zone. Ray-based inversions were used as start models for the full-waveform inversion. In order to assess the optimization and evaluate different acquisition setups, the checkerboard test was adapted as a resolution analysis tool and applied on full-waveform inversion results for the different acquisition setups. The final model results are superim-posed with a suitable checkerboard pattern, which are reconstructed using full-waveform inversion. A comparison of the reconstructed with the original pattern by a semblance

approach results in resolvability distributions of the full-waveform inversion results.

The full-waveform inversion results showed a similarly good resolved middle layer for all setups and anomalies in the upper- and lowermost layers in the ε and σ distributions and gradients. The conductivity model was generally smoother for the sparse setup whereas more layers were distinguishable with the dense setup. In further studies, the reliability of additional features resolved with the dense setup should be proven. The gradients of the semi-reciprocal and the dense setups were more homogeneous and the permittivity resolvabilities were similar and better compared to the sparse setup. For conductivity, the resolvability decreased with less transmitters and receivers and was also better for the semi-reciprocal and dense setups. It turned out, that the distribution of resolvabilities reflects the ray-coverage. The advantage of semi-reciprocal setups with sparser transmitter than receiver spatial samplings, on the one hand, was confirmed by similarly good resolvabilities like the dense setup and high resolvabilities close to both boreholes, in contrast, on the other hand, to lower values close to the transmitter borehole for the sparse setup. The checkerboard analysis provides a powerful tool to assess the obtained resolution.

Appendix B

High resolution imaging of the unsaturated and saturated zones of a gravel aquifer using full-waveform inversion [1]

Full-waveform inversion can significantly improve imaging results of crosshole GPR data compared to conventional ray-based inversion schemes. Recently, a 2D full-waveform finite difference time domain (FDTD) approach is used to invert crosshole GPR data measured in the saturated zone of a gravel aquifer. Due to water table refractions and reflections, the upper part of the aquifer was not reliably imaged. Here, we reconstruct the upper part of the aquifer by imaging both the saturated and unsaturated zones and extend the inversion domain by including data acquired in the unsaturated zone of the aquifer (2 m - 4 m depth). Estimating one effective wavelet, as was done for the saturated zone inversion alone, is insufficient because the effective wavelet strongly depends on the location of both the transmitter and receiver antennas. Therefore, four different source wavelets were estimated for the different combinations of antennas placement in the two zones, and the full-waveform inversion algorithm adapted accordingly. This resulted in improved images of the aquifer. In general, the observed and the modeled traces show a good correspondence in both shape and amplitude. For the transmitters in the unsaturated domain, the amplitude fit was not optimum and can probably be improved by adjusting the conductivity starting model.

---

[1]adapted from Klotzsche, A., van der Kruk, J., Vereecken, H., Meles, G. A, Doetsch, J., Maurer, H., Greenhalgh, S. A., Green, A. G. and Linde, N., 2011, 6th International workshop on advanced ground penetrating radar, 20-24.

B.1 Test site, measurement setup and geological background

Crosshole GPR data were acquired close to the Thur River in the Thur valley in Switzerland. A 7 m thick glaciofluvial gravel deposit is formed near the river, which is embedded between alluvial loam (silty sands) in the top three meters and lacustrine sediments (low permeable clays) below 10 m depth (see Fig. B.1). Close to the river, monitoring wells with a diameter of 11.4 cm were installed and GPR data were measured using the RA-MAC Ground Vision system of MalåGeosience with 250 MHZ antennas in six planes Doetsch *et al.* (2010b). Here, we investigate the data acquired along the south-west plane below and above the water table, which is at approximately 4.2 m depth. Between 2 m - 10 m depth two semi-reciprocal crosshole measurements were employed, each with 14 transmitters (spacing 0.5 m) and around 70 receivers (spacing 0.1 m).
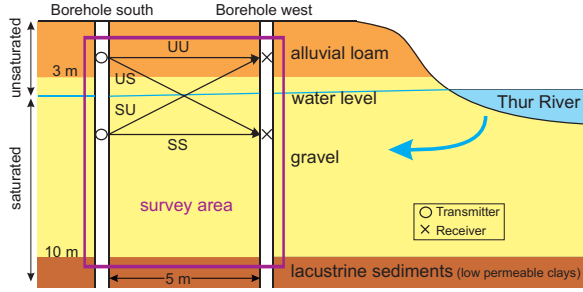
Figure B.1: Simplified geological representation of the measurement domain showing a three- layered structure from top to bottom: alluvial loam, gravel, and lacustrine sediments (extended from Klotzsche *et al.* (2010)). The water table is at approximately 4 m depth and transmitters and receivers are indicated by circles and crosses, respectively. Possible source-receiver combinations in the unsaturated (U) and saturated (S) zone are indicated by UU, SS, US, and SU.

B.2 Full-waveform inversion for the unsaturated and saturated zones

Since full-waveform inversion incorporates all arrivals we expect a better image reconstruction of the aquifer close to the water table when the unsaturated zone is included in the model and inversion domains. Specifically, the forward model should also include

refractions and reflections at the water table, which exist in the observed data. First, we analyze the behavior of the source wavelet in the different zones and then describe the full-waveform inversion for the combined saturated and unsaturated domain.

B.2.1 Source wavelet estimation for unsaturated and saturated zones

The typical procedure to estimate the unknown source wavelet consists of three steps Klotzsche *et al.* (2010). Firstly, a source wavelet is estimated by using only horizontally traveling rays where just the shape of the wavelet is considered. Secondly, the shape and the amplitude of the source wavelet are corrected by deconvolving the Green's function calculated from the starting model with the measured data. Thirdly, the source wavelet is updated after several iterations of the full-waveform inversion.

The use of one effective source wavelet Klotzsche *et al.* (2010) for the saturated and unsaturated zones did not lead to satisfactory results, because of different effects of the borehole fillings on the measurements in each zone. The effective wavelets are very different, depending on where each antenna is located Tronicke & Holliger (2004). Similar effects occur for the receiver antennas. Depending on the location of the antennas and the water level, four possible effective wavelets are obtained. These are illustrated in Figure B.1, where the following combinations are considered: transmitter and receiver are both located in the unsaturated medium (UU) or in the saturated medium (SS), or the transmitter is placed in the unsaturated medium and the receiver in the saturated medium (US), or vice versa (SU). Figures B.2 and B.3 show the separately obtained non-normalized and normalized effective wavelets and the corresponding amplitude spectra for the four different setups UU, SS, US and SU shown in blue, red, green and cyan, respectively (all three correction steps were applied). The wavelet with the highest frequency and amplitude is obtained when transmitter and receiver are both located in the unsaturated domain (blue lines in Figs B.2 and B.3), whereas the lowest frequency and amplitude wavelet occurs when both antennas are located in the saturated domain (red lines in Figs B.2 and B.3). When one antenna is located in the unsaturated zone and the other in the saturated zone, wavelets having intermediate central frequencies and amplitudes are obtained (green and cyan lines in Figs B.2 and B.3). Note, that the different amplitudes indicate that the source and receiver are non-reciprocal.
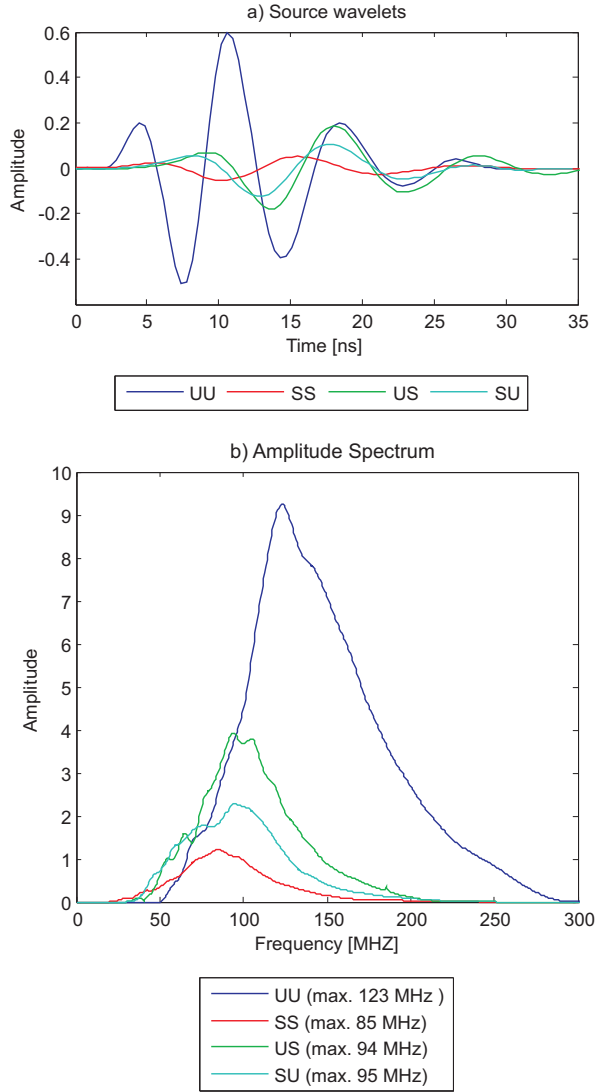
Figure B.2: a) estimated effective source wavelets and b) amplitude spectra for the four estimated source wavelets. UU, SS, US and SU are shown in blue, red, green and cyan, respectively.
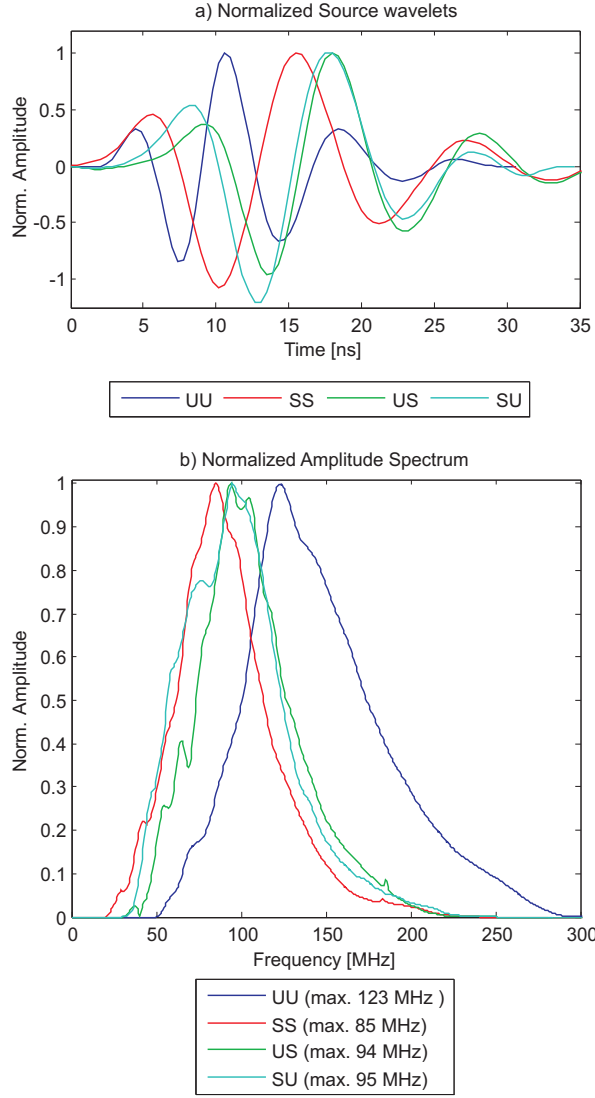
Figure B.3: a) normalized effective source wavelets and b) normalized amplitude spectra for the estimated source wavelets. . UU, SS, US and SU are shown in blue, red, green and cyan, respectively. Note, that the maximum frequency and amplitude is achieved for the UU wavelet and decrease towards SS. US and SU have a similar shape and center frequency.

B.2.2 Principle of the combined full-waveform inversion

The full-waveform inversion method is a gradient-based iterative optimization scheme Meles *et al.* (2010), which is adapted to using the different source wavelets for the simultaneous inversion of the unsaturated and saturated domains. In the first step, the residual wave field between the observed and the synthetic data is calculated. Before the synthetic data can be computed, it is necessary to assign and distribute the wavelets. For each transmitter two source wavelets need to be applied separately for receivers in the unsaturated and saturated domain. For both wavelets the synthetic data are calculated and assembled together, depending on the position of the water level. In the second step, the residual wave field is back-propagated to compute the gradient by means of a zero-lag cross-correlation of the synthetic and back-propagated residual wave fields. Next, the optimal step-lengths for the permittivity and conductivity are obtained and in the last step the permittivity and conductivity model are updated for each iteration with the corresponding gradient and step lengths for each iteration. Therefore, the same procedure is applied to compute the perturbed traces as for the computing of the synthetic field in step 1. The inversion loop is stopped, if the root-mean-square error between the observed and synthetic data is changing less than 0.5 % between two iterations.

B.2.3 Results of the combined full-waveform inversion

The full-waveform inversion was carried out for 28 transmitters and 140 receivers. It is important to define a good starting model because the amplitudes of the source wavelets are closely linked to the conductivity model, and both factors have a strong influence on the conductivity values obtained by the full-waveform inversion. Similar to the inversion carried out for the saturated domain alone Klotzsche *et al.* (2010), the travel time inversion results were used as the starting permittivity model for the saturated domain. Due to the low ray-coverage between 4.2 m - 6 m, a layer with relative permittivity of 17 was assumed. Different starting model tests showed that a layer of relative permittivity 17 fits the observed data best. Relative permittivity values for the unsaturated gravel and the loam are reported to lie between 3 - 6 and 5 - 20, respectively Daniels *et al.* (2005); Davis & Annan (1989). Forward modeling indicated a relative permittivity of 6 for the depth domain 0 m - 4.2 m. The capillary transition zone between unsaturated and saturated gravel is expected to be very thin and in the order of the cell size of 9 cm. For the conductivity, we used a homogeneous starting model of 9.5 mS\m. If clay is present in the aquifer, the conductivity values will increase with an increasing amount of clay. Therefore, for the alluvial loam and for the lacustrine sediments a higher conductivity after the inversion is expected than for the gravel layer Davis & Annan (1989).
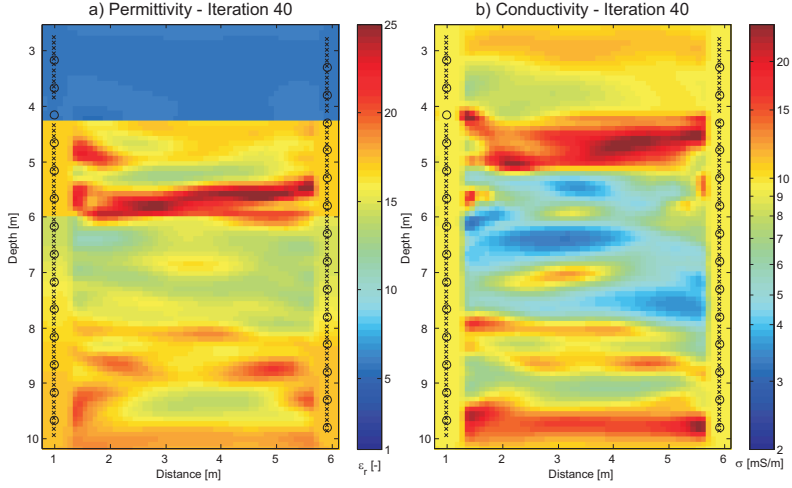
Figure B.4: a) Relative permittivity and b) conductivity tomograms after 40 iterations of the full-waveform inversion using four different wavelets. Transmitters and receiver are shown with circle and crosses, respectively. Note the logarithmic scale of the conductivity tomogram.

Figure B.4a and b show the relative permittivity and conductivity tomograms, respectively, after the 40th iteration of the full-waveform inversion scheme. Due to the presence of the water table at 4.2 m depth, and the correspondingly different starting model, the unsaturated zone between 2.5 m - 4.2 m depth shows a much lower permittivity compared to the saturated zone (see Fig. B.4a). For the zone in the depth range 6 m - 11 m, similar permittivity and conductivity results are obtained as when only the saturated zone is inverted Klotzsche *et al.* (2010). The underlying lacustrine sediments are clearly visible below 9.5 m depth, with conductivity values around 20 mS\m. For the zone between 4.2 m - 6 m, where alternating high and low permittivity and conductivity values were obtained when inverting only the saturated region Klotzsche *et al.* (2010), completely different results are now obtained. A high permittivity zone can be observed between 5.2 m - 6 m depth. The RMS is reduced by approximately 50 % compared to the travel time inversion.

Figure B.5 shows the normalized and un-normalized observed and modeled radargram source gathers for transmitters 1 - 14 for the final inverted model (transmitters and receivers are located in the west and south borehole, respectively). In Figures B.5a and b, the normalized radargrams of the modeled and observed data are depicted, and indicate that most of measured direct, reflected and refracted arrivals are well fitted by the modeled

data. In Figures B.5c and d, the un-normalized data are shown at true amplitude. Most amplitudes of the measured data are also well-fitted by the modeled data. Similar results are obtained for the transmitters 15 - 28 from the semi-reciprocal measurements (not shown). For antennas partly in unsaturated and saturated domain (transmitter 3 and 17), the fit is expected to be less good. Also for transmitters 1 - 2 and 15 - 16 the fit is less good, which is probably due to an insufficient start model for the conductivity in the unsaturated domain.
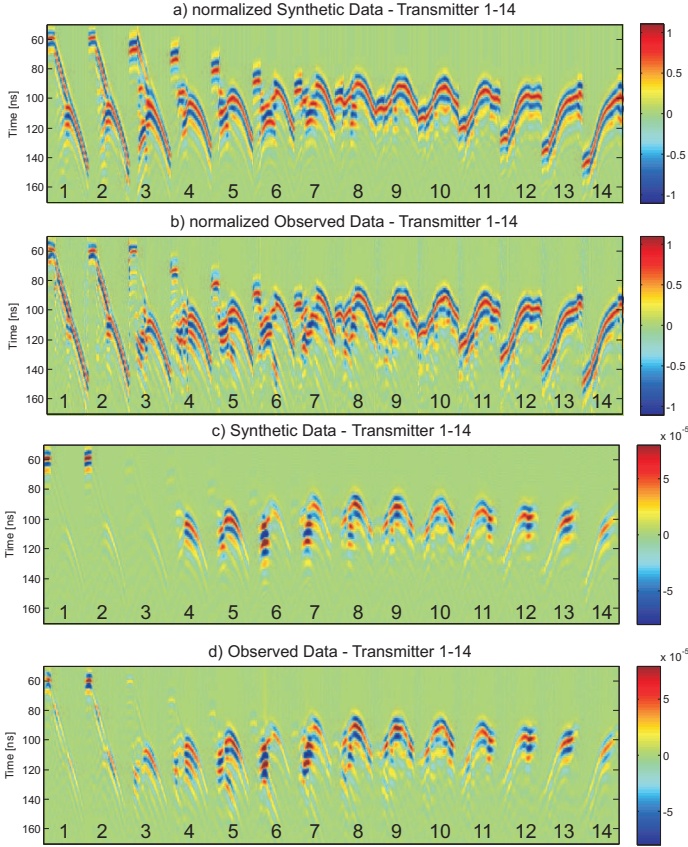
Figure B.5: a) and b) show the modeled and observed radargram source gather data normalized to the maximum amplitude, respectively. c) and d) show the true amplitude modeled and observed data. The numbers indicate the transmitter, 1-14. The modeled and experimental data show a very good fit in amplitude and shape. For transmitters 1-3, the amplitude fit is less good.

In the un-normalized measured and modeled radargrams, high amplitudes and elongated wave-trains can be observed for transmitters 6 and 7 for the receiver depth range between 5.2 m - 6 m depth, which indicates the presence of a waveguide van der Kruk *et al.* (2006) where the high permittivity zone is present (see Fig. B.4a). For the transmitters 20 - 21 from the semi-reciprocal measurements the same behavior is observed. Inversion of only the saturated domain showed residual gradients between 5 m - 6 m depth (see Chapter 3). Inverting jointly both the saturated and unsaturated domain, results in an almost vanishing gradient (not shown) for the permittivity and conductivity in the whole inversion domain, indicating that the model is describing the measurements well.

B.3   Conclusions and outlook

A full-waveform inversion algorithm for crosshole GPR data has been extended to incorporate both the saturated and unsaturated parts of a gravel aquifer in Switzerland. Due to the different borehole filling effects of the transmitter and receiver antennas in the saturated and unsaturated domains, it is necessary to estimate four different effective source wavelets to simultaneously invert for the permittivity and conductivity in the unsaturated and saturated regions of the aquifer. With the use of these four wavelets, high resolution images were obtained. Especially the aquifer characterization close to the water table is significantly improved using the unsaturated and saturated GPR data. In addition, a high permittivity layer could be delineated, which indicated the presence of a waveguide. The measurements for the source and receivers which were present over the depth range of the high permittivity layer in the saturated aquifer, along with the modeled data that show high amplitudes and elongated wave-trains, confirm the presence of a waveguide. The amplitudes for transmitters in the unsaturated domain were less well reconstructed by the model, which is probably due to a non-optimum conductivity starting model, and needs to be improved.

We obtained (1) very similar inversion results using different start models, (2) a good fit between the observed and modeled data travel times, waveforms, and amplitudes, and (3) an almost vanishing gradient. These observations indicate that the inverted model describes the measurements well and we assume that we found a good approximation of the global minimum for the saturated part of this dataset.

Appendix C

Improvements in crosshole GPR full-waveform inversion and application on data measured at the Boise Hydrogeophysics Research Site[1]

Since the first application of full-waveform inversion on experimental GPR data, the algorithm has been significantly improved. An overview is given of all developments by applying different versions of the full-waveform inversion to the experimental data set acquired at the Boise Hydrogeophysics Research Site in Idaho. Almost all improvements resulted in a reducing final misfit between the measured and synthetic data and a reducing gradient at the final iteration. One of the first full-waveform inversions of crosshole GPR data was based on a 2D scalar finite-difference time-domain solutions of Maxwell Equations (Ernst *et al.*, 2007a). This approach was applied to synthetic and to two experimental data sets (Ernst *et al.*, 2007b); one obtained in the Grimsel rock laboratory and one obtained at the Boise Hydrogeophysics Research Site (BHRS). Since these first applications of full-waveform inversion for crosshole GPR data, the full-waveform inversion has been improved by including the vector character of the electrical field and the simultaneous inversion of permittivity and conductivity (Meles *et al.*, 2010). Recently, this method was extended by allowing a more flexible source-receiver setup to minimize the computational costs and applied it to a data set measured on a gravel aquifer in

---

[1]adapted from Yang, X., Klotzsche, A., van der Kruk, J., Vereecken, H., Meles, G. A. and Maurer, H., 2011, 6th International workshop on advanced ground penetrating radar, 304-307.

Switzerland (Klotzsche *et al.*, 2010). In the following, an overview is given of all developments by showing all improvements (Meles *et al.*, 2010; Klotzsche *et al.*, 2010) of the full-waveform inversion to the experimental data set acquired at the BHRS (Ernst *et al.*, 2007b), which includes the use of all receiver data available, which is four times as many as originally used (Ernst *et al.*, 2007b).

C.1 Boise aquifer

The BHRS aquifer consists of a 20 m thick gravel- sand aquifer, which is embedded over a ≥ 3 m thick layer of red clay (see Fig. C.1). Within the aquifer five main units (four pebble and cobble dominated and a sand channel) and one subunit have been identified based on the Neutron-Neutron porosity logs and capacitive conductivity logs (Barrash & Clemo, 2002; Mwenifumbo *et al.*, 2009).
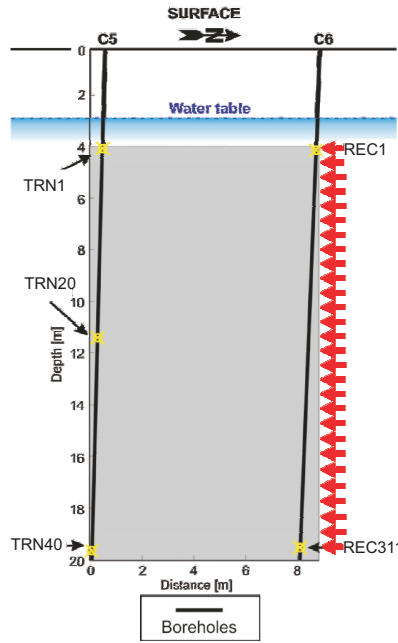
Figure C.1: Simplified acquisition setup of the experimental data set acquired at the Boise test side (adapted from Ernst *et al.* (2007b)). Transmitter and receiver locations are indicated by TRN and REC, respectively.

C.2 GPR survey layout

A high quality crosshole GPR dataset (Ernst *et al.*, 2007b; Tronicke *et al.*, 2004) was acquired in two vertical boreholes (C6 and C5) over a depth range of 20 m. The distance between the boreholes is approximately 8.5 m and the diameter of the boreholes casing is 0.1 m. The dominant antenna frequency of ~ 80 MHz yielded a dominant wavelength of ~ 1 m in the low velocity sediments. Although 311 receivers with a vertical spacing of 0.05 m were used to measure the data, initial inversion (Ernst *et al.*, 2007b) only used 77 receiver locations with a spatial sampling of 0.4 m. Here, we used all 311 receivers with a vertical spacing of 0.05 m, which is not requiring more calculation time (Klotzsche *et al.*, 2010). All inversions used 40 transmitters with a vertical spacing of 0.4 m. Note that, the depths are below measuring point in context.

C.3 Inversion results

C.3.1 Comparison of the inversion results

During the inversion, the root mean square (RMS) error between the measured and calculate data over all time samples is minimized (Meles *et al.*, 2010). The results of the cumulative improvements of full-waveform inversion are shown in Figure C.2. In the following, the number of traces used in the inversion is 77 unless mentioned otherwise. The ray-based inversion provides low resolution permittivity and conductivity images which are shown in Figures C.2a and f, respectively. A higher resolution of the subsurface is shown in Figures C.2b, g by applying the scalar full-waveform version (Ernst *et al.*, 2007a), using the stepped approach that inverts for the permittivity while keeping the conductivities fixed and vice versa. A prominent dipping feature in the results of permittivity and conductivity between 9 m and 12 m depth is visible. Table C.1 shows the obtained RMS value between the measured and inverted data which decreased significantly compared to the ray-based inversion. Note, that the ray-based inversion results are used as starting model for the full-waveform inversion.

The vectorial inversion (Figs C.2c, h) that considers the vectorial nature of the electric fields, returns similar imaging results and a slightly smaller RMS value was obtained (see Table C.1). Next, a simultaneous full-waveform inversion of the permittivity and conductivity values is used where the step-lengths and updates for these two parameters are calculated for each iteration. Although this process requires an additional forward model calculation, the simultaneous nature of the process results in a reduction of the total number of forward calculations needed (Figs C.2d, i). Here, the prominent dipping
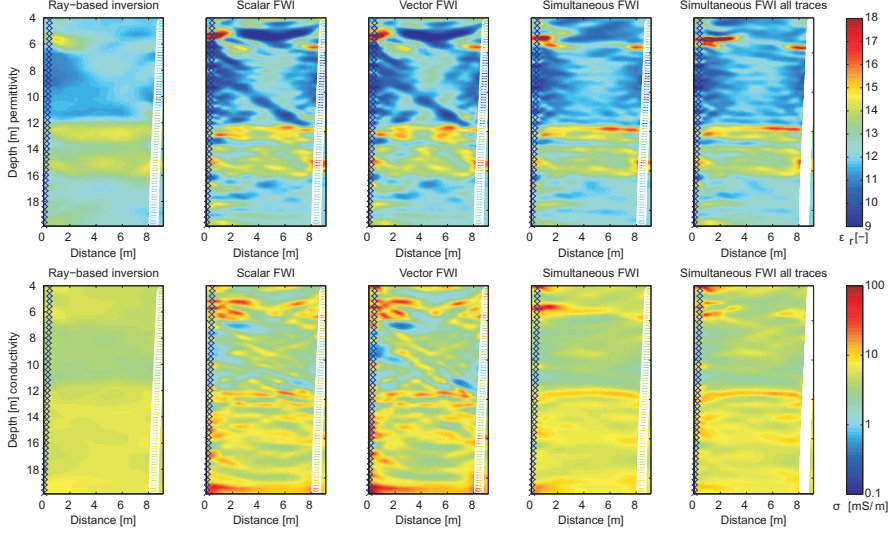
Figure C.2: Comparison of ray-based (equals the start model of the full-waveform inversion) and all full-waveform inversion results of the BHRS data. Transmitter and receivers are indicated by crosses and circles, respectively. Note, that for a - d and f - i 77 receivers are used, whereas for e and j all 311 receivers are used. Note the logarithmical scale of the conductivity images.

feature is nearly absent and the obtained RMS value is again reduced with more than 20 %, which indicates that the dipping feature is a numerical artefact. Running the simultaneous full-waveform inversion with 311 traces, the images show only small differences from the simultaneous full-waveform inversion results using 77 traces (Figs C.2 e, j). However, the obtained RMS value reduced distinctly.

C.3.2 Gradient comparison of the different full-waveform inversions

To investigate the reliability of the inversion results we show all remaining gradients in Figure C.3 using the same color scale. The mean gradient values are given in Table C.1. Note, that the permittivity gradients are much larger than the conductivity gradients due to an additional time derivative (see Eq. 22 in Meles *et al.* (2010)). Figures C.3a and f show the permittivity and conductivity gradients at the first iteration of the full-waveform inversion. Note, that here the ray-based inversion result is used as start model for the full-waveform inversion. The remaining gradients at the final inversion iteration number

30 of all full-waveform inversion methods are shown in Figures C.3b - e and C.3g - j. Remaining gradients for the scalar and vector version using a stepped approach shows still relatively large amplitudes between 9 and 12 m (Figs C.3 b, c, g, h). Note, that in this region also the artificial dipping feature was detected. This is an interval of high capacitive resistivity including the anomalous subunit recognized by Mwenifumbo *et al.* (2009). The remaining gradients for the vector version are slightly larger than the scalar version, which is probably caused by using the two components of the vector electromagnetic fields to calculate the gradients. Smaller and more homogeneous gradients are obtained by the simultaneous version of full-waveform inversion (Figs C.3d, i). For the permittivity gradient, the fluctuation on the porosity units boundary are nearly absent, but for the gradient of conductivity we can still observe some small amplitude fluctuations. When using 311 traces for the simultaneous full-waveform inversion the absolute mean value of the gradients are significantly reduced and relatively homogeneous gradient for both permittivity and conductivity are obtained (Figs C.3e, j). However, the permittivity and conductivity images show only small differences from the simultaneous full-waveform inversion results using 77 traces (see Fig. C.2). This indicates that an optimum acquisition setup exists where a limited number of traces are used. More research is needed to determine this optimum acquisition setup. Summarizing, we see that by improving the full-waveform inversion the absolute mean value of the gradient is decreasing significantly (see Table C.1) and that remaining gradients indicate regions where the images are less reliable.

Table C.1: Forward calculation time and RMS values for the different methods shown in Figure C.2 and absolute mean values of the gradients shown in Figure C.4.

Inversion method	Calculation time	Forward times	RMS	Mean gradient value for ε	Mean gradient value for σ
Ray-based	—	—	$3.4 \cdot 10^{-6}$	$3.4514 10^{9}$	7.7694
Scalar	69 min	180	$2.4 \cdot 10^{-6}$	$1.3578 10^{8}$	0.0826
Vector	69 min	180	$2.4 \cdot 10^{-6}$	$2.0771 10^{8}$	0.1927
Simultaneous	86 min	120	$1.9 \cdot 10^{-6}$	$4.9463 10^{7}$	0.0514
All traces simult.	86 min	120	$1.6 \cdot 10^{-6}$	$8.7286 10^{6}$	0.0174

C.3.3   Comparison of the observed and simulated radar traces

Figure C.4a shows notable misfits between the observed and simulated radar traces derived from the ray-based tomograms, particularly in the central regions of the receiver gather.
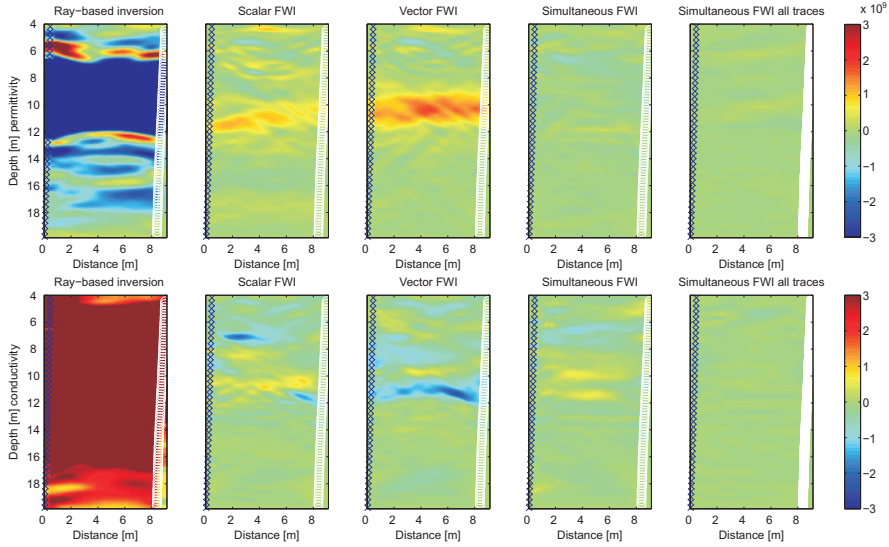
Figure C.3: Comparison of the gradients obtained of the final full-waveform inversion results. a) and b) show the gradients for the permittivity and conductivity, respectively, after one iteration of the full-waveform inversion to illustrated the misfit between the ray-bases inversion results and the observed data. Transmitter and receivers are indicated by crosses and circles, respectively.

Figure C.4b shows that the radar traces generated from the full-waveform tomogram (Figs C.2 e, j) fit quite well with the observed data. For small depths and small trace numbers, the correspondence for the second part of the wave train is poor.

The FWI results clearly show the boundaries of the main units at 12 and 16 m, which have a good correspondence with the findings of previous studies (Ernst *et al.*, 2007b; Barrash & Clemo, 2002; Mwenifumbo *et al.*, 2009; Tronicke *et al.*, 2004; Dafflon *et al.*, 2011b). The boundary around 6.5 m depth is less clear (likely the base of a sandy lens within Unit 4 that is continuous between wells C5 and C6, W. Barrash, pers. commun. 2011), but seems to correlate with the increased misfit observed in Figure C.4 for shallow depths. Using the improved full-waveform inversion (Meles *et al.*, 2011) that gradually and progressively expands the frequency content as the iterations proceed might improve these inversion results.
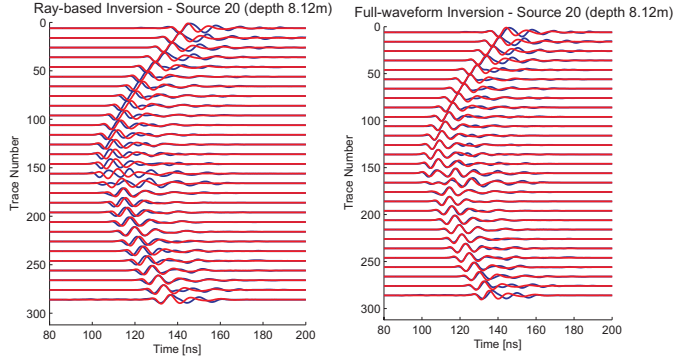
Figure C.4: Normalized receiver gathers for source 20 at depth of 8.5 m in Figure C.2. The blue and red lines show the measured and synthetic radar traces, respectively, for the ray tomograms shown in Figures C.2a and f and full-waveform tomograms in Figures C.2e and j).

C.4   Conclusions

The BHRS data have been inverted with several versions of the full-waveform inversion including a new version where all traces (311 instead of 77) are used. The results show that it is important to include the vector character and to use a simultaneous update for the permittivity and conductivity values. Almost every improvement of the full-waveform inversion resulted in a reduced misfit and smaller remaining gradients at the final iteration. Regions with relatively high remaining gradient amplitudes indicate less reliable inversion results. Using four times as many receivers resulted in similar inversion results as using the initial number of receivers. More research is needed to determine the optimum measurement setup (number of sources and receivers and their spatial sampling).

Acknowledgments & Danksagung

Without the help, contribution and constant encouragements of many special people from the Agroshere and elsewhere, whom I had the privilege to meet and work with, I would not yet be at the end of my dissertation. For this great support, I wish to thank everyone who contributed in one or another way to my success.

First and foremost, I would like to express my gratitude to my doctoral adviser and mentor Prof. Dr. Jan van der Kruk for his outstanding supervision and for introducing me to the field of hydrogeophysics. His belief in my abilities and my work, his open ears for my problems and his constant motivation, had always a positive influence to my dissertation. Thanks a lot for the great support. Des Weiteren danke ich Prof. Dr. Thomas Bohlen sehr für den Aufwand und die Zeit die er als Zweitgutachter in die Beurteilung meiner Arbeit investiert und Prof. Dr. Christoph Clauser, dass er den Vorsitze der Promotionskommission übernimmt.

During the last three years I had the pleasure to work with great scientists that contribute in one way or another to my publications. I am indebted to Niklas Linde, Joseph Doetsch, Giovanni Meles, Hansrüdi Maurer, Stewart Greenhalgh and Harry Vereecken for their helpful comments, great input, support, and suggestions. In the beginning of the third year of my PhD studies, I had the chance to visit Prof. Dr. John Bradford for three months at the Boise State University in Boise, Idaho, USA. This trip was a highlight in my education because of John's hospitality, and to get in touch with the American way of life with the support of his family.

To apply the full-waveform inversion a lot of computer powers are necessary, therefore I want to thank the JSC of the research center Jülich to get acsess to the JUMP and JUROPA cluster during the last years.

Zu großem Dank verpflichtet bin ich allen aktuellen (und einigen ehemaligen) Mitgliedern meiner Arbeitsgruppe - insbesondere Jutta Bikowski und unsere nie endenen Diskusionen über the Volle-wellenform-inversion, Jenneke Bakker, Max Oberröhrmann, Sebastian Rudolf, Xi Yang und Sebastian Busch.

Working in the Agrosphere gave me the opportunity to meet many great colleagues but also meanwhile good friends. Especially my lunch and coffee group - particular Daniela,

Kathrina, Katrin, Laura, Maria, Markus, Sadam, Sebastian G., Sonja and Wei - and office mates (especially Paul ☺) remained me everyday that there is more in life than work. Des Weiteren danke ich Natalie für inspirierende Bücherdiskussionen und vegetarische Sonntagabendessen. Diese Arbeit wäre bei weitem nicht abgabereif geworden ohne die kritischen Vorschläge und Anmerkungen aller derer, die ihre wertvolle Zeit geopfert haben, einzelne Teile eingehend zu lesen und zu kommentieren - vielen Dank an Bea, Katrin, Laura, Markus, Maria und Sonja.

Des Weitern hat mir mein privates Umfeld und meine Familie immer mit Rat und Tat zur Seite gestanden wofür ich ihnen sehr dankbar bin. Allem vorweg Bea deren langjährige Freundschaft mir immer wieder gezeigt hat das auch Germanisten und Geophysiker gar nicht so verschieden sind. Und schließlich gebührt vor allem meine Eltern großer Dank, die mich seit vielen Jahren bei allen meinen Vorhaben nach Kräften bestärkt und unterstützt haben, und mir immer Kraft gegeben haben immer weiter zumachen.

Bibliography

Annan, A. P. (2005): *Hydrogeophysics: GPR methodes for hydrogeophysical studies* (Springer Netherlands).

Archie, G. E. (1942): *The electrical resistivity log as an aid in determining some reservoir characteristics.* Transactions of the American Institute of Mining and Metallurgical Engineers 146, 54–61.

Arcone, S. A. (1995): *Numerical-studies of the radiation-patterns of resistively loaded dipoles.* Journal of Applied Geophysics 33(1-3), 39–52.

Arcone, S. A., P. R. Peapples, & L. B. Liu (2003): *Propagation of a ground-penetrating radar (GPR) pulse in a thin-surface waveguide.* Geophysics 68(6), 1922–1933.

Barrash, W. & T. Clemo (2002): *Hierarchical geostatistics and multifacies systems: Boise Hydrogeophysical Research Site, Boise, Idaho.* Water Resources Research 38(10).

Barrash, W., T. Clemo, & M. D. Knoll (1999): *Boise Hydrogeophysical Research Site (BHRS): Objectives, design, initial geostatistical results.* Proceedings of the Symposium on the Application of Geophysics to Engineering and Environmental Problems 389–398.

Barrash, W. & E. C. Reboulet (2004): *Significance of porosity for stratigraphy and textural composition in subsurface, coarse fluvial deposits: Boise Hydrogeophysical Research Site.* Geological Society of America Bulletin 116(9-10), 1059–1073.

Belina, F., J. Irving, J. Ernst, & K. Holliger (2012): *Evaluation of the reconstruction limits of a frequency-independent crosshole georadar waveform inversion scheme in the presence of dispersion.* Journal of Applied Geophysics 78, 9–19.

Belina, F. A., J. R. Ernst, & K. Holliger (2009): *Inversion of crosshole seismic data in heterogeneous environments: Comparison of waveform and ray-based approaches.* Journal of Applied Geophysics 68, 85–94.

Berenger, J.-P. (1994): *A perfectly matched layer for the absorption of electromagnetic waves.* Computational Physics 114, 185–200.

Bianchi, M., C. M. Zheng, C. Wilson, *et al.* (2011): *Spatial connectivity in a highly heterogeneous aquifer: From cores to preferential flow paths.* Water Resources Research 47.

Binley, A., G. Cassiani, R. Middleton, & P. Winship (2002a): *Vadose zone flow model parameterisation using cross-borehole radar and resistivity imaging.* Journal of Hydrology 267, 147–159.

Binley, A., P. Winship, R. Middleton, M. Pokar, & J. West (2001): *High-resolution characterization of vadose zone dynamics using cross-borehole radar.* Water Resources Research 37(11), 2639–2652.

Binley, A., P. Winshipa, L. J. Westb, M. Pokarb, & R. Middletona (2002b): *Seasonal variation of moisture content in unsaturated sandstone inferred from borehole radar and resistivity profiles.* Journal of Hydrology 267, 160–172.

Bleistein, N. (1986): *2-1/2 dimensional inplane wave-propagation.* Geophysical Prospecting 34, 686–703.

Blindow, N. (1997): *Handbuch zur Erkundung des Untergrundes von Deponien und Altlasten Band 3: Bodenradar* (Springer Verlag Berlin, Heidelberg).

Bohlen, T. (2002): *Parallel 3-d viscoelastic finite difference seismic modelling.* Computers and Geosciences 28, 887–899.

Bradford, J. H. (2010): *Advances in near surface seismology and ground-penetrating radar*, chap. 19. Integrated Hydrostratigraphic Interpretation of 3D Seismic-Reflection and Multifold Pseudo-3D GPR Data, 313–326 (Society of Exploration Geophysicists).

Bradford, J. H., W. P. Clement, & W. Barrash (2009): *Estimating porosity with ground-penetrating radar reflection tomography: A controlled 3-D experiment at the Boise Hydrogeophysical Research Site.* Water Resources Research 45.

Brauchler, R., R. Hu, P. Dietrich, & M. Sauter (2011): *A field assessment of high-resolution aquifer characterization based on hydraulic travel time and hydraulic attenuation tomography.* Water Resources Research 47.

Busch, S., J. van der Kruk, J. Bikowski, & H. Vereecken (2012): *Quantitative conductivity and permittivity estimation using full-waveform inversion of on-ground gpr data.* Geophysics 77(6), H79–H91.

Buursink, M. L., T. C. Johnson, P. S. Routh, & M. D. Knoll (2008): *Crosshole radar velocity tomography with finite-frequency fresnel volume sensitivities.* Geophysical Journal International 172, 1–17.

Cassidy, N. (2009): *Ground Penetrating Radar Data Processing, Modelling and Analysis. In: Ground Penetrating Radar Data Processing, Modelling and Analysis* (Elsevier Science).

Cerveny, V. (2001): *Seismic Ray Theory* (Cambridge University Press).

Cirpka, O. A., M. N. Fienen, M. Hofer, *et al.* (2007): *Analyzing bank filtration by deconvoluting time series of electric conductivity.* Ground Water 45(3), 318–328.

Clement, W. P. & W. Barrash (2006): *Crosshole radar tomography in a fluvial aquifer near Boise, Idaho.* Journal of Environmental and Engineering Geophysics 11(3), 171–184.

Clement, W. P., M. D. Knoll, L. M. Liberty, *et al.* (1999): *Geophysical surveys across the Boise Hydrogeophysical Research Site to determine geophysical parameters of a shallow, alluvial aquifer.* Proceedings of the Symposium on the Application of Geophysics to Engineering and Environmental Problems 399–408.

Collin, R. E. (1991): *Field theory of guided waves* (IEEE Press).

Coscia, I., S. A. Greenhalgh, N. Linde, *et al.* (2011): *3D crosshole ert for aquifer characterization and monitoring of infiltrating river water.* Geophysics 76(2), G49–G59.

Coscia, I., N. Linde, S. Greenhalgh, T. Vogt, & A. Green (2012): *Estimating traveltimes and groundwater flow patterns using 3D time-lapse crosshole ERT imaging of electrical resistivity fluctuations induced by infiltrating river water.* Geophysics 77(4), E239–E250.

Dafflon, B., W. Barrash, M. Cardiff, & T. C. Johnson (2011a): *Hydrological parameter estimations from a conservative tracer test with variable-density effects at the Boise Hydrogeophysical Research Site.* Water Resources Research 47.

Dafflon, B., J. Irving, & W. Barrash (2011b): *Inversion of multiple intersecting high-resolution crosshole GPR profiles for hydrological characterization at the Boise Hydrogeophysical Research Site.* Journal of Applied Geophysics 73(4), 305–314.

Daniels, J. J., B. Allred, A. Binley, D. Labrecque, & D. Alumbaugh (2005): *Hydrogeophysics: Hydrogeophysical case studies in the vadose zone* (Springer Netherlands).

Davis, J. & A. Annan (1989): *Ground-penetrating radar for high-resolution mapping of soil and rock stratigraphy.* Geophysical Prospecting 37, 531–551.

Day, P. C. S. M. C., A. J. (2001): *Three-dimensional crustal structure and magma chamber geometry at the intermediate-spreading, back-arc Valu Fa ridge, Lau Basin - results of a wide-angle seismic tomographic inversion.* Geophysical Journal International 146, 31–52.

Day-Lewis, F. D., J. W. Lane, J. M. Harris, & S. M. Gorelick (2003): *Time-lapse imaging of saline-tracer transport in fractured rock using difference-attenuation radar tomography.* Water Resources Research 39.

Day-Lewis, F. D., K. Singha, & A. M. Binley (2005): *Applying petrophysical models to radar travel time and electrical resistivity tomograms: Resolution-dependent limitations.* Journal of Geophysical Research-Solid Earth 110.

Dessa, J. X. & G. Pascal (2003): *Combined traveltime and frequency-domain seismic waveform inversion: a case study on multi-offset ultrasonic data.* Geophysical Journal International 154, 117–133.

Dickens, T. A. (1994): *Diffraction tomography for crosswell imaging of nearly layered media.* Geophysics 59, 694–706.

Diem, S., T. Vogt, & E. Hoehn (2010): *Spatial characterization of hydraulic conductivity in alluvial gravel-and-sand aquifers: a comparison of methods.* Grundwasser 15(4), 241–251.

Doetsch, J., N. Linde, I. Coscia, S. A. Greenhalgh, & A. G. Green (2010b): *Zonation for 3D aquifer characterization based on joint inversions of multimethod crosshole geophysical data.* Geophysics 75(6), G53–G64.

Doetsch, J. A., I. Coscia, S. Greenhalgh, *et al.* (2010a): *The borehole-fluid effect in electrical resistivity imaging.* Geophysics 75(4), F107–F114.

Dogan, M., R. L. Van Dam, G. C. Bohling, J. J. Butler, & D. W. Hyndman (2011): *Hydrostratigraphic analysis of the MADE site with full-resolution GPR and direct-push hydraulic profiling.* Geophysical Research Letters 38.

Ellefsen, K. J. (1999): *Effects of layered sediments on the guided wave in crosswell radar data.* Geophysics 64, 1698–1707.

Englert, A. (2003): *Measurement, Estimation and Modelling of Groundwater Flow Velocity at Krauthausen Test Site.* Ph.D. thesis, RWTH Aachen University.

Ernst, J. (2007): *2-D finite-difference time-domain full-waveform inversion of crosshole georadar data.* Ph.D. thesis, Swiss Federal Institute of Technology Zurich.

Ernst, J. R., K. Holliger, H. Maurer, & A. G. Green (2006): *Realistic FDTD modelling of borehole georadar antenna radiation: methodology and application.* Near Surface Geophysics 4, 19–30.

Ernst, J. R., H. Maurer, A. G. Green, & K. Holliger (2007a): *Full-waveform inversion of crosshole radar data based on 2-D finite-difference time-domain solutions of Maxwells equations.* IEEE Transactions on Geoscience and Remote Sensing 45, 2807–2828.

Ernst, J. R., H. Maurer, A. G. Green, & K. Holliger (2007b): *Application of a new 2D time-domain full-waveform inversion scheme to crosshole radar data.* Geophysics 72, J53–J64.

Ewing, J. W. S., M. & F. Press (1957): *Elastic waves in layered media* (McGraw-Hill Book Co.).

Fichtner, A. & J. Trampert (2011): *Resolution analysis in full waveform inversion.* Geophysical Journal International 187, 1604–1624.

Füchtbauer, H. (1988): *Sedimente und Sedimentgesteine: Sandsteine* (Schweizerbart Stuttgart.), 4th ed.

Garambois, S., P. Senechal, & H. Perroud (2002): *On the use of combined geophysical methods to assess water content and water conductivity of near-surface formations.* Journal of Hydrology 259(1-4), 32–48.

Greenhalgh, S. A., B. Zhou, D. R. Pant, & A. Green (2007): *Numerical study of seismic scattering and waveguide excitation in faulted coal seams.* Geophysical Prospecting 55(2), 185–198.

al Hagrey, S. A. & J. Michaelson (1999): *Resistivity and percolation study of preferential flow in vadose zone at Bokhorst, Germany.* Geophysics 64, 746–753.

al Hagrey, S. A. a. & C. Müller (2000): *GPR study of pore water content and salinity in sand.* Geophysical Prospecting 48(1), 63–85.

Holliger, K., M. Musil, & H. Maurer (2001): *Ray-based amplitude tomography for crosshole georadar data: A numerical assessment.* Applied Geophysics 47, 285298.

Hubbard, S. S., J. S. Chen, J. Peterson, *et al.* (2001): *Hydrogeological characterization of the South Oyster Bacterial Transport Site using geophysical data.* Water Resources Research 37(10), 2431–2456.

Hubbard, S. S., J. E. Peterson, Jr, *et al.* (1997): *Estimation of permeable pathways and water content using tomographic radar data.* The Leading Edge 16(11), 1623–1630.

Hubbard, S. S. & Y. Rubin (2000): *Hydrogeological parameter estimation using geophysical data: a review of selected techniques.* Journal of Contaminant Hydrology 45(1-2), 3–34.

Kemna, A., J. Vanderborght, B. Kulessa, & H. Vereecken (2002): *Imaging and characterisation of subsurface solute transport using electrical resistivity tomography (ERT) and equivalent transport models.* Journal of Hydrology 267(3-4), 125–146.

Kettridge, N., X. Comas, A. Baird, *et al.* (2008): *Ecohydrologically important subsurface structures in peatlands revealed by ground-penetrating radar and complex conductivity surveys.* Journal of Geophysical Research 113, G04 030.

Klotzsche, A., J. van der Kruk, G. A. Meles, *et al.* (2010): *Full-waveform inversion of cross-hole ground-penetrating radar data to characterize a gravel aquifer close to the Thur River, Switzerland.* Near Surface Geophysics 8(6), 635–649.

Klotzsche, A., J. v. d. Kruk, G. Meles, & H. Vereecken (2012): *Crosshole GPR full-waveform inversion of waveguides acting as preferential flow paths within aquifer systems.* Geophysics 77(4), H57–H62.

van der Kruk, J. (2001): *Three diensional imaging of multi-comonent ground penetrating radar data.* Ph.D. thesis, Technische Universiteit Delft.

van der Kruk, J., R. W. Jacob, & H. Vereecken (2006): *Properties of precipitation-induced multilayer surface waveguides derived from inversion of dispersive TE and TM GPR data.* Geophysics 75(4), WA263–WA273.

van der Kruk, J., C. M. Steelman, A. L. Endres, & H. Vereecken (2009a): *Dispersion inversion of electromagnetic pulse propagation within freezing and thawing soil waveguides.* Geophysical Research Letters 36.

van der Kruk, J., H. Vereecken, & R. W. Jacob (2009b): *Identifying dispersive GPR signals and inverting for surface wave-guide properties.* The Leading Edge 28(10), 1234–1239.

van der Kruk, J., C. P. A. Wapenaar, J. T. Fokkema, & P. M. van der Berg (2003): *Improved three dimensional image reconstruction technique for mulit-component ground penetrating radar data.* Subsurface Sensing Technologies and Applications 4, 61–99.

Kuroda, S., M. Takeuchi, & H. J. Kim (2007): *Full-waveform inversion algorithm for interpreting crosshole radar data: a theoretical approach.* Geosciences Journal 11(3), 211–217.

Lanz, E., H. Maurer, & A. G. Green (1998): *Refraction tomography over a buried waste disposal site.* Geophysics 63, 1414–1433.

Linde, N., A. Binley, A. Tryggvason, L. B. Pedersen, & A. Revil (2006): *Improved hydrogeophysical characterization using joint inversion of cross-hole electrical resistance and ground-penetrating radar traveltime data.* Water Resources Research 42(12).

Linde, N., A. Tryggvason, J. E. Peterson, & S. S. Hubbard (2008): *Joint inversion of crosshole radar and seismic traveltimes acquired at the South Oyster Bacterial Transport site.* Geophysics 73(4), G29–G37.

Liner, C. (2004): *Elements of 3D Seismology* (Pennwell Corp).

Lines, L. R., K. R. Kelly, & J. Queen (1992): *Channel waves in cross-borehole data.* Geophysics 57, 334–342.

Lochbühler, T., J. Doetsch, R. Brauchler, & N. Linde (2013): *Structure-coupled joint inversion of geophysical and hydrological data.* GEOPHYSICS 78(3), ID1–ID14.

Looms, M. C., K. H. Jensen, A. Binley, & L. Nielsen (2008): *Monitoring unsaturated flow and transport using cross-borehole geophysical methods.* Vadose Zone Journal 7, 227–237.

Maurer, H. & A. G. Green (1997): *Potential coordinate mislocations in crosshole tomography: Results from the Grimsel test site, Switzerland.* Geophysics 62, 1696–1709.

Maurer, H., S. Greenhalgh, & S. Latzel (2009): *Frequency and spatial sampling strategies for crosshole seismic waveform spectral inversion experiments.* Geophysics 74, Wcc79–Wcc89.

Maurer, H. & M. Musil (2004): *Effects and removal of systematic errors in crosshole georadar attenuation tomography.* Journal of applied Geophysics 55, 261–270.

Meles, G., S. Greenhalgh, J. van der Kruk, A. Green, & H. Maurer (2011): *Taming the non-linearity problem in GPR full-waveform inversion for high contrast media*. Journal of Applied Geophysics 73(2), 174–186.

Meles, G., J. Van der Kruk, S. A. Greenhalgh, *et al.* (2010): *A new vector waveform inversion algorithm for simultaneous updating of conductivity and permittivity parameters from combination crosshole/borehole-to-surface GPR data*. IEEE Transactions on Geoscience and Remote Sensing 48(9), 3391–3407.

Meles, G. A., S. A. Greenhalgh, A. G. Green, H. Maurer, & J. Van der Kruk (2012): *GPR full-waveform sensitivity and resolution analysis using an FDTD adjoint method*. IEEE Transactions on Geoscience and Remote Sensing 50(5), 1881–1896.

Menke, W. (1989): *Geophysical Data Analysis: Discrete Inverse Theory* (Academic Press Inc. New York).

Mora, P. (1987): *Nonlinear two-dimensional elastic inversion of multioffset seismic data*. Geophysics 52, 1211–1228.

Morgan, J. V., G. L. Christeson, & C. A. Zelt (2002): *Testing the resolution of a 3D velocity tomogram across the Chicxulub crater*. Tectonophysics 355, 215–226.

Musil, M., H. Maurer, K. Hollinger, & A. G. Green (2006): *Internal structure of an alpine rock glacier based on crosshole georadar traveltimes and amplitudes*. Geophysical Prospecting 54, 273–285.

Musil, M., H. R. Maurer, & A. G. Green (2003): *Discrete tomography and joint inversion for loosely connected or unconnected physical properties: application to crosshole seismic and georadar data sets*. Geophysical Journal International 2, 389–402.

Mwenifumbo, C. J., W. Barrash, & M. D. Knoll (2009): *Capacitive conductivity logging and electrical stratigraphy in a high-resistivity aquifer, Boise Hydrogeophysical Research Site*. Geophysics 74(3), E125–E133.

Oberröhrmann, M., A. Klotzsche, J. van der Kruk, & H. Vereecken (2013): *Optimization of acquisition setup for cross-hole GPR fullwaveform inversion using checkerboard analysis*. Near Surface Geophysics 11.

Oldenborger, K. M. D. R. P. S. L. D. J., G. A. (2007): *Time-lapse ERT monitoring of an injection/withdrawal experiment in a shallow unconfined aquilfer*. Geophysics 72, F177–F187.

Paige, C. & M. A. Saunders (1982): *LSQR: Analgorithm for sparse linear equations and sparse least squares.* ACMTrans. Math. Softw. 8, 43–71.

Pratt, R. G. (1999): *Seismic waveform inversion in the frequency domain, part 1: Theory and verification in a physical scale model.* Geophysics 64(3), 888–901.

Pratt, R. G. & R. M. Shipp (1999): *Seismic waveform inversion in the frequency domain, part 2: Fault delineation in sediments using crosshole data.* Geophysics 64(3), 902–914.

Pride, S. (1994): *Govering equations for the coupled electromagnetics and acoustics of porous-media.* Physical Rev. 50, 678696.

Rabbel, W. (1996): *Groundwater Geophysics: Seismic Methodes* (Springer Berlin Heidelberg).

Rao, Y., Y. H. Wang, & J. V. Morgan (2006): *Crosshole seismic waveform tomography - ii. strategy for real data application.* Geophysical Journal International 166, 1237–1248.

Ronayne, M. J. & S. M. Gorelick (2006): *Effective permeability of porous media containing branching channel networks.* Physical Review E 73.

Rubin, Y., G. Mavko, & J. Harris (1992): *Mapping permeability in heterogeneous aquifers using hydrologic and seismic data.* Water Resources Research 28(7), 1809–1816.

Scheibe, T. & S. Yabusaki (1998): *Scaling of flow and transport behavior in heterogeneous groundwater systems.* Advances in Water Resources 22(3), 223–238.

Schneider, W. A. J., K. A. Ranzinger, A. H. Balch, & C. Kruse (1992): *A dynamic programming approach to first arrival traveltime computation in media with arbitrarily distributed velocities.* Geophysics 57, 39–50.

Shin, C. & Y. H. Cha (2008): *Waveform inversion in the Laplace domain.* Geophysical Journal International 173, 922–931.

Slater, L. D., D. Ntarlagiannis, F. D. Day-Lewis, *et al.* (2010): *Use of electrical imaging and distributed temperature sensing methods to characterize surface water-groundwater exchange regulating uranium transport at the Hanford 300 area, Washington.* Water Resources Research 46.

Straface, S., F. Chidichimo, E. Rizzo, *et al.* (2011): *Joint inversion of steady-state hydrologic and self-potential data for 3D hydraulic conductivity distribution at the Boise Hydrogeophysical Research Site.* Journal of Hydrology 407(1-4), 115–128.

Streich, R. & J. van der Kruk (2007): *Characterizing a gpr antenna system by near-field electric field measurements.* Geophysics 72(5), A51–A55. 213RA Times Cited:6 Cited References Count:11.

Streich, v. d. K. J., R. (2007a): *Accurate imaging of multicomponent GPR data based on exact radiation patterns.* IEEE Transactions on Geoscience and Remote Sensing 45, 93–103.

Streich, v. d. K. J., R. (2007b): *Characterization a GPR-antenna system by near-field electrical field measurements.* Geophysics 72, A51–A55.

Strobach, E., B. D. Harris, J. C. Dupuis, A. W. Kepic, & M. W. Martin (2012): *Cross well radar and vertical radar profiling methods for time lapse monitoring of rainfall infiltration.* In: *ASEG Extended Abstracts*, 1–4.

Tarantola, A. (1984a): *Inversion of seismic-reflection data in the acoustic approximation.* Geophysics 49, 1259–1266.

Tarantola, A. (1984b): *Linearized invesion of seismic reflection data.* Geophysical Prospecting 32(6), 998–1015.

Tarantola, A. (1986): *A strategy for non-linear elastic inversion of seismic-reflection data.* Geophysics 51(10), 1893–1903.

Tarantola, A. (2005): *Inverse Problem Theory and Methodes for Model Parameter Estimation* (Society for Industrial Mathematics).

Tchang, T. (2012): *Intégration de données géophysiques pour obtenir un modèle en trois dimensions d'un aquifère au voisinage de la rivière Thur, Suisse.* Master's thesis.

Tillmann, A., A. Englert, Z. Nyari, *et al.* (2008): *Characterization of subsoil heterogeneity, estimation of grain size distribution and hydraulic conductivity at the Krauthausen test site using Cone Penetration Test.* Journal of Contaminant Hydrology 95, 57–75.

Tillmann A., F. I. E. A. V. J. S. J. e. a., Nyari Z. (2005): *Cone penetration tests (CPT) on the Krauthausen Test Site, part i: Data aquisition and preliminary interpretation of the surveys 2003 and 2004.* Forschungszentrum Jülich GmbH. .

Topp, G. C., J. L. Davis, & A. P. Annan (1980): *Electromagnetic determination of soil-water content - measurements in coaxial transmission-lines.* Water Resources Research 16(3), 574–582.

Tronicke, J., N. Blindow, R. Gross, & M. A. Lange (1999): *Joint application of surface electrical resistivity- and GPR-measurements for groundwater exploration on the island of Spiekeroog - northern Germany.* Journal of Hydrology 223(1-2), 44–53.

Tronicke, J., P. Dietrich, U. Wahlig, & E. Appel (2002): *Integrating surface georadar and crosshole radar tomography: A validation experiment in braided stream deposits.* Geophysics 67, 1516–1523.

Tronicke, J. & K. Holliger (2004): *Effects of gas- and water-filled boreholes on the amplitudes of crosshole georadar data as inferred from experimental evidence.* Geophysics 69(5), 1255–1260.

Tronicke, J., K. Holliger, W. Barrash, & M. D. Knoll (2004): *Multivariate analysis of cross-hole georadar velocity and attenuation tomograms for aquifer zonation.* Water Resources Research 40.

Turesson, A. (2006): *Water content and porosity estimated from ground-penetrating radar and resistivity.* Journal of Applied Geophysics 58(2), 99–111.

Vereecken, H., U. Doring, H. Hardelauf, *et al.* (2000): *Analysis of solute transport in a heterogeneous aquifer: the Krauthausen field experiment.* Journal of Contaminant Hydrology 45, 329–358.

Vidale, J. E. (1990): *Finite-difference calculation of traveltimes in three dimensions.* Geophysics 55(5), 521–526.

Virieux, J. & S. Operto (2009): *An overview of full-waveform inversion in exploration geophysics.* Geophysics 74(6), WCC1–WCC26.

Wang, Y. H. & Y. Rao (2006): *Crosshole seismic waveform tomography - II. resolution analysis.* Geophysical Journal International 166, 1224–1236.

Watanabe, T. K., T. Nihei, S. Nakagawa, & L. R. Myer (2004): *Viscoacoustic waveform inversion of transmission data for velocity and attenuation.* Journal of the Acoustical Society ofAmerica 115, 3059–3067.

Waxman, L. J. M., M. H. Smits (1968): *Electrical conductivities in oil-bearing shaly sands.* Society of Petroleum Engineers Journal 8, 107–122.

Williamson, P. R. (1991): *A guide to the limits of resolution imposed by scattering in ray tomography.* Geophysics 56, 202–207.

Winship, P., A. Binley, & D. Gomez (2006): *Flow and transport in the unsaturated Sherwood sandstone: characterization using cross-borehole geophysical methods.* Geological Society, London, Special Publications 263, 219–231.

Worthington, P. F. (1993): *The uses and abuses of the Archie Equations .1. the formation factor porosity relationship.* Journal of Applied Geophysics 30, 215–228.

Wu, R. S. & M. N. Toksoz (1987): *Diffraction tomography and multisource holography applied to seismic imaging.* Geophysics 52, 11–25.

Yang, X., A. Klotzsche, G. A. Meles, V. H., & van der Kruk J. (2013): *Improvements in crosshole gpr full-waveform inversion and application on data measured at the boise hydrogeophysics research site.* Journal of Applied Geophysics doi:http://dx.doi.org/10.1016/j.jappgeo.2013.08.007.

Zelt, C. A. (1998): *Lateral velocity resolution from three-dimensional seismic refraction data.* Geophysical Journal International 135, 1101–1112.

Zelt, C. A. & P. J. Barton (1998): *Three-dimensional seismic refraction tomography: A comparison of two methods applied to data from the Faeroe Basin.* Journal of Geophysical Research-Solid Earth 103, 7187–7210.

Zelt, C. A. & R. M. Ellis (1988): *Practical and efficient ray tracing in two-dimensional media for rapid traveltime and amplitude forward modeling.* Canadian Journal of Exploration Geophysics 24(1), 16–31.

Zhang, J. C. C. C. T. A. P. R. G., F. J. (2012): *Cross-well seismic waveform tomography for monitoring CO2 injection: a case study from the Ketzin Site, Germany.* Geophysical Journal International 189, 629–646.

Zheng, C. M., M. Bianchi, & S. M. Gorelick (2011): *Lessons learned from 25 years of research at the MADE Site.* Ground Water 49(5), 649–662.

Zheng, C. M. & S. M. Gorelick (2003): *Analysis of solute transport in flow fields influenced by preferential flowpaths at the decimeter scale.* Ground Water 41(2), 142–155.

Zhou, B. & S. A. Greenhalgh (1998a): *Crosshole acoustic velocity imaging with the full-waveform spectral data: 2.5-D numerical simulations.* Exploration Geophysics 29, 680–684.

Zhou, B. & S. A. Greenhalgh (1998b): *A damping methode for 2.5-D Green's function for arbitrary acoustic media.* Geophysics 144, 111–120.

Zhou, B. & S. A. Greenhalgh (2003): *Crosshole seismic inversion with normalized full-waveform amplitude data.* Geophysics 68, 1320–1330.

List of Figures

List of Tables

Anja Klotzsche

curriculum vitae

Linnicher Str. 9
D-52428 Jülich
☎ +49 2461 61-1796
📱 +49 173 4592795
✉ a.klotzsche@fz-juelich.de

Personal details

Date of birth	August 7th, 1985
Place of birth	Schlema (Germany)
Nationality	German

Education

10/2009–02/2013	**Doctoral studies**, *Forschungszentrum Jülich and RWTH Aachen (Germany).*
Doctoral thesis	Full-waveform inversion of crosshole GPR data for hydrogeological applications.
Supervisor	Prof. Dr. Jan van der Kruk, *IBG 3 - Agrosphere, Forschungszentrum Jülich and RWTH Aachen*
09/2007–08/2009	**Master in Applied Geophysics**, *Joint Master Program of the Universities: TU Delft (Netherlands), ETH Zurich (Switzerland) and RWTH Aachen (Germany).*
Master thesis	Full-waveform inversion of cross-hole ground penetrating radar data to characterize a gravel aquifer close to the river Thur, Switzerland.
Supervisor	Prof. Dr. Jan van der Kruk, *IBG 3 - Agrosphere, Forschungszentrum Jülich and RWTH Aachen*
10/2004–08/2007	**Bachelor in Geophysics**, *TUBA Freiberg (Germany).*
Bachelor thesis	Gravimetrische Messungen im Kloster Osek (Gravimetric analysis in the convent Osek).
Supervisor	Prof. Dr. Klaus Spitzer, *TUBA Freiberg*
09/1996–07/2004	**Abitur**, *Johann-Gottfried-Herder-Gymnasium, Schneeberg (Germany).*

Work experience

Boise State University, Idaho, USA

011/2011–02/2012 Three-months stay at the Boise State University in the research group Center for Geophysical Investigation of the Shallow Subsurface.
During the work with Prof. Dr. John Bradford the full-waveform inversion was applied to a dataset measured at the Boise Hydrogeophysical Research Site and the inversion algorithm was extended to include surface to borehole data.

ETH Zurich, Switzerland

06/2008 Student assistant for a seismic survey in the Niederweningen Project for Heinrich Horstmeyer

TUBA Freiberg, Germany

2005–2006 Student assistant for Prof. Ratschbacher in the area stone preparation in the faculty of Geosciences

Publications

2013 **Klotzsche, A.**, J. van der Kruk, N. Linde, J. Doetsch, and H. Vereecken, *3-D characterization of high-permeability zones in a gravel aquifer using 2-D crosshole GPR full-waveform inversion and waveguide detection.* Geophysical Journal International, doi: 10.1093/gji/ggt275.

2013 Yang, X., **A. Klotzsche**, G. A. Meles, H. Vereecken, and J. van der Kruk, *Improvements in crosshole GPR full-waveform inversion and application on data measured at the Boise Hydrogeophysics Research Site.* J. of Applied Geophysics, http://dx.doi.org/10.1016/j.jappgeo.2013.08.007.

2013 Oberöhrmann, M., **A. Klotzsche**, H. Vereecken, and J. van der Kruk, *Optimization of acquisition setup for cross-hole GPR full-waveform inversion using checkerboard analysis.* Near Surface Geophysics 11, 197-209, 2013, doi: 10.3997/1873-0604.2012045.

2012 **Klotzsche, A.**, J. van der Kruk, A. G. Meles, and H. Vereecken, *Characterizing a low-velocity waveguide using crosshole GPR full-waveform inversion.* Geophysics 77, H57-H62, 2012, doi: 10.1190/geo2011-0458.1.

2012 van der Kruk, J., **A. Klotzsche**, S. Busch, and H. Vereecken, *Neueste Ergebnisse der Dispersionsinversion und Vollen-Wellenfeldinversion von Georadar Daten.* Georadar Rundtischgespräch, DGG 8, 631-646, 2012.

2010 **Klotzsche, A.**, J. van der Kruk, A. G. Meles, J. Doetsch, H. Maurer, and N. Linde, *Full-waveform inversion of crosshole ground penetrating radar data to characterize a gravel aquifer close to the river Thur, Switzerland.* Near Surface Geophysics 8, 631-646, 2010, doi: 10.3997/1873-0604.2010054.

in preparation **Klotzsche, A.**, J. Bradford, H. Vereecken and J. van der Kruk, *Detection and identification of waveguides with limited lateral extension using crosshole GPR full-waveform inversion and the amplitude analysis approach: synthetic and experimental study.*

Awards

07/2012 Award within Homework session Tomography Bake-off at the SEG-AGU Hydrogeophysics Workshop 2012, Boise State University, Idaho, USA: *Crosshole GPR full-waveform inversion to characterize the aquifer of the Boise Hydrogeophysical Research Site*, poster presentation

06/2012 Award for best young researcher at the 14 International Conference on Ground Penetrating Radar, Shanghai, China: *Characterizing a low-velocity waveguide using crosshole GPR full-waveform inversion*, extended abstract and oral presentation

06/2010 Award for best young researcher at the XIII International Conference on Ground Penetrating Radar, Lecce, Italy: *Full-waveform inversion of crosshole ground penetrating radar data to characterize a gravel aquifer close to the Thur River, Switzerland*, extended abstract and oral presentation

Conferences and Workshops

06/2013 7th International Workshop on Advanced Ground Penetrating Radar, Nantes, France: *3D Characterization of an aquifer using Full-waveform inversion and amplitude analysis* , oral presentation

04/2013 European Geosciences Union (EGU) General Assembly 2013, Vienna, Austria: *Crosshole GPR full-waveform inversion and amplitude analysis of waveguides for 3D characterization of a gravel aquifer*, oral presentation

03/2013 Deutsche Geophysikalische Gesellschaft (DGG), Leipzig, Germany: *Waveguide characterization using crosshole GPR full-waveform inversion and novel amplitude analysis approach*, oral presentation

02/2013 Full-waveform inversion workshop, Karlsruhe, Germany: *Full-waveform inversion of crosshole ground penetrating radar data for hydrogeological applications*, oral presentation

07/2012 SEG-AGU Hydrogeophysics Workshop 2012, Boise State University, Idaho, USA: *Crosshole GPR full-waveform inversion to characterize the aquifer of the Boise Hydrogeophysical Research Site*, oral and poster presentation

06/2012 14th International Conference on Ground Penetrating Radar, Shanghai, China: *Characterizing a low-velocity waveguide using crosshole GPR full-waveform inversion*, oral presentation

03/2012 Deutsche Geophysikalische Gesellschaft (DGG), Hamburg, Germany: *Imaging of a low-velocity waveguide within a gravel aquifer using crosshole GPR full-waveform inversion*, oral presentation

12/2011 American Geoscience Union (AGU) Fall Meeting 2011, San Francisco, USA: *Imaging high contrast layers within a gravel aquifer using full-waveform crosshole GPR inversion*, oral presentation

06/2011 4th International Workshop on Advanced Ground Penetrating Radar, Aachen, Germany: *High resolution imaging of the unsaturated and saturated zones of a gravel aquifer using Full-waveform inversion*, oral presentation

04/2011 European Geosciences Union (EGU) General Assembly 2011, Vienna, Austria: *High resolution imaging of the saturated and unsaturated zone of a gravel aquifer using full-waveform borehole GPR inversion*, oral presentation

03/2011	Deutsche Geophysikalische Gesellschaft (DGG), Cologne, Germany: *Full-waveform inversion of the unsaturated and saturated zone of a gravel aquifer*, oral presentation
06/2010	XIII International Conference on Ground Penetrating Radar, Lecce, Italy: *Full-waveform inversion of crosshole ground penetrating radar data to characterize a gravel aquifer close to the Thur River, Switzerland*, oral presentation

Trainings

11/2010	HLRS Parallel Programming Workshop - MPI, OpenMP, PETSc for beginners, Jülich Supercomputing Centre
06/2010	Scientific writing course, Institute for Bio- and Geoscience 3
02/2009	VI-HPS Tuning Workshop, Jülich Supercomputing Centre

Languages

German	Mother tongue
English	Fluent (written and spoken)
Dutch	Basic
Latein	Latinum

Computer skills

Prog. languages	C, C++ (intermediate)
Libraries	OpenMP (basic), MPI (basic)
Computer algebra	Matlab (advanced)
Operating systems	Windows (advanced), Linux (basic)
Geopysical Tools	ProMax, Petrell, ModFlow, 3D Groundwater Explorer, Dc2InvRes (all basics)

Interests

Literature	Fiction, Fantasy, Crime
Sports	Swimming, Cycling, Hiking

Anja Klotzsche   Jülich, 10/21/2013

Band / Volume 180
**Entwicklung und Herstellung von metallgestützten Festelektrolyt-
Brennstoffzellen mit Hilfe des Hohlkathoden-Gasflusssputterns**
M. Haydn (2013), XVI, 174 pp
ISBN: 978-3-89336-886-0

Band / Volume 181
**Characterization and stability investigation of water dispersible colloids
(WDCs) in natural soils**
C. Jiang (2013), X, 102 pp
ISBN: 978-3-89336-887-7

Band / Volume 182
**Monazite-type Ceramics for Conditioning of Minor Actinides:
Structural Characterization and Properties**
C. Babelot (2013), x, 127 pp
ISBN: 978-3-89336-889-1

Band / Volume 183
**High-rate growth of hydrogenated amorphous and microcrystalline silicon
for thin-film silicon solar cells using dynamic very-high frequency plasma-
enhanced chemical vapor deposition**
T. Zimmermann (2013), x, 126 pp
ISBN: 978-3-89336-892-1

Band / Volume 184
IEK-3 Report 2013. Durable Electrochemical Process Engineering
(2013), ca. 180 pp
ISBN: 978-3-89336-893-8

Band / Volume 185
**Light Trapping with Plasmonic Back Contacts
in Thin-Film Silicon Solar Cells**
U. W. Paetzold (2013), X, 175 pp
ISBN: 978-3-89336-895-2

Band / Volume 186
**Plant-plant interactions, biodiversity & assembly
in grasslands and their relevance to restoration**
V. M. Temperton (2013), ca 420 pp
ISBN: 978-3-89336-896-9

Band / Volume 187
**Ab initio investigation of ground-states and ionic motion
in particular in zirconia-based solid-oxide electrolytes**
J. A. Hirschfeld (2013), v, 144 pp
ISBN: 978-3-89336-897-6

JÜLICH
FORSCHUNGSZENTRUM